이학박사학위논문

Mobility enhancement in wide bandgap semiconductor $BaSnO_3$

넓은 밴드갭 반도체인 $BaSnO_3$의
이동성 향상에 관한 연구

2018년 2월

서울대학교 대학원
물리천문학부
신 주 연

Mobility enhancement in wide bandgap semiconductor $BaSnO_3$

지도교수 차 국 린

이 논문을 이학박사학위논문으로 제출함

2018년 2월

서울대학교 대학원

물리천문학부

신 주 연

신주연의 박사학위논문을 인준함

2018년 2월

위 원 장 노 태 원 (인)

부위원장 차 국 린 (인)

위 원 김 대 식 (인)

위 원 박 윤 (인)

위 원 최 우 석 (인)

Abstract

Mobility enhancement in wide bandgap semiconductor $BaSnO_3$

Juyeon Shin

Department of Physics and Astronomy

The Graduate School

Seoul National University

Wide bandgap semiconductors have received much attention for their potential applications in high-temperature and high-power electronics. Apart from typical wide bandgap semiconductors, e.g. SiC and GaN, there has been a growing interest in perovskite oxide $BaSnO_3$, which is studied especially for transparent conducting oxides and transparent oxide semiconductors in transparent electronics, to date. In usual active devices in display, the transport property, e.g. mobility, is less important compared to its transparency because the reaction of human eye is slow compared to the speed of digital processing. On the other hand, $BaSnO_3$ has a high mobility, which records the highest value among wide bandgap semiconductors in the degenerate doped regime, so that the study for enhancement of its mobility combined into devices is surely needed toward its application in high-temperature and high frequency area, not only constrained in transparent electronics.

Another particular advantages using $BaSnO_3$-based electronics is the development of all epitaxial heterostructures, that is, incorporating of perovskite oxides with large

polarization, ferroelectricity, ferromagnetism and multiferroicity. This enables application toward non-volatile switching memory and spintronics, which give the opportunity for extending the amount and type of information in electronics.

This dissertation focuses on the study of mobility enhancement of $BaSnO_3$ in three aspects such as the excellent transport on MgO substrate, bandgap engineering by Hf doping for the possibility of modulation doped heterostructure, and modulation doped-polar interface by $LaInO_3$/undoped $BaSnO_3$/La-doped $BaSnO_3$ heterostructures. All the epitaxial films are grown by using the pulsed laser deposition technique. And the crystallinity of films is investigated by X-ray diffraction analysis; single phase growth, well defined orientation. The transmission electron spectroscopy has been employed to study the microstructural property of crystalline $BaSnO_3$ films such as misfit dislocations and threading dislocations. The transport property of films, e. g. resistivity, mobility, carrier concentration, was measured by Van der Pauw method and all the devices has a three terminal-field effect transistor structures with metal-insulator-semiconductor interfaces.

Because the research of $BaSnO_3$ is limited on films on perovskite oxide substrates such as $SrTiO_3$, $SmScO_3$, $PrScO_3$, $LaAlO_3$, and $BaSnO_3$, which suffer from a small size, a small bandgap and oxygen instability, the effort to grow $BaSnO_3$ films with excellent transport property on non-perovskite MgO substrate is very important toward wafer scale processing with oxygen stability. This opens commercially the area of $BaSnO_3$-based electronics, too. In spite of non-perovskite oxide substrate, the maximum electron mobility of La-doped $BaSnO_3$ films is 97.2 cm^2/Vs, which is quite comparable value deposited on $BaSnO_3$ single crystal substrate. And the field effect transistor with HfO_2 dielectrics reveals successful carrier modulation of La-doped $BaSnO_3$ channel with mobility of 43.9 cm^2/Vs and on-off ratio of 3.0×10^7, which is slightly better compared to devices on $SrTiO_3$ substrate.

Another possibility to enhance mobility of devices based on $BaSnO_3$ channel is modulation doping like GaAs system. The carrier modulation of $BaSnO_3$ by field

effect is limited in metal-insulator-semiconductor structure, to date. So intentional La doping or unintentional oxygen vacancies, source of electron carriers, may degrade the device performance. On the other hand, heterostructures with interfaces of doped large bandgap material and channel can increase mobility by reducing ionized impurity scattering. To employ this modulation doping in $BaSnO_3$-based heterostructures, bandgap engineering is a necessary step. So, Hf substation for Sn in $BaSnO_3$ is investigated, which significantly modifies the band structure, crystal structure, and the bandgap. Also La doping in $BaSn_{1-x}Hf_xO_3$ is investigated, displaying significant potentials for modulation doping in $BaSnO_3/BaSn_{1-x}Hf_xO_3$ heterostructures.

Lastly, enhancement of mobility of $BaSnO_3$ in polar interface has been studied. The optimal condition of semiconductor devices is switching with low-on-state resistance. To manipulate highly conductive current, high sheet carrier concentration and high mobility is needed in field-induced confined well. Polarization doping helps to accumulate high density of mobile charges, which is impossible in usual solid-gate-dielectrics. Recently, conducting interface between $LaInO_3$/La-doped $BaSnO_3$ was reported with high sheet carrier density in the order of 10^{13} cm^{-2}. Moreover, if the mobility of channel in this polar interface is enhanced, the two dimensional electron gas science in $BaSnO_3$-based electronics will be more powerful. Because the slight La doping on $BaSnO_3$ channel is needed to accumulate high carrier density, modulation doping technique is applied in smaller bandgap $BaSnO_3$ compared to $LaInO_3$ by inserting undoped $BaSnO_3$ spacer layer between La-doped $BaSnO_3$ and $LaInO_3$. The enhanced mobility of this modulation doped-polar interface may lead further advance of $LaInO_3/BaSnO_3$ polar interface in high mobility and high power electronics applications.

Keywords: high mobility, $BaSnO_3$, perovskite oxide, pulsed laser deposition, wide bandgap semiconductor, modulation doping, polar interface, bandgap engineering

Student number: 2012-20367

Contents

List of figures

List of Tables

Chapter 1

Introduction

This dissertation mainly illustrates the endeavors to employ high mobility heterostructure devices based on $BaSnO_3$ (BSO) like similar platforms studied in conventional semiconductors such as Si, GaAs, GaN, etc with structures of metal-insulator-semiconductor, modulation-doped heterointerface, and modulation- doped polar interface. The earlier outstanding paper for BSO was its use in transparent conductive oxide (TCO) for transparent electronics [1,2]. Because BSO is a stable oxide, which is largely different from usual oxide materials, suffering from the stability of interface through repeated thermal cycles and uncontrollability of electron carriers by unintentional oxygen vacancies [3,4], its incorporation into display electronics is natural, as expected to replace the area of In_2O_3:Sn [5]. Meanwhile, the high mobility [1] of La-doped BSO (BLSO) enables to play as a highly conductive metal electrode, following published papers, in which the band bending of BSO was successfully modulated through field effect transistors [6-9], drive the potential of BSO-based electronics toward high temperature, high power, and high frequency electronics mainly treated in wide bandgap semiconductors (WBGs) [10-12].

The most special feature, enabling BSO-based electronics to jump over usual WBGs application, is its class of materials, namely, perovskite oxides with the chemical formula of ABO_3. The edge-sharing octahedral oxygen network in perovskite oxide can support a wide varierty of cations on the A and B sites, displaying a rich functional properties such as magnetism [13], piezoelectricity [14], ferroelectricity [15], multiferroicity [16], and superconductivity [17]. All epitaxial heterostructures that incorporate a high mobility channel of BSO and any other functional perovskite oxide have a potential to open a new generation of semiconductor electronics.

Until now, many subsequent studies to improve the mobility of BSO, have focused on the material properties on perovskite oxide substrate for epitaxial growth; various dopant, suitable substrate selection, and deposition method, etc [18-27]. And the heterostructure devices based on BSO channel has been constrained in the field effect transistors of metal-insulator-semiconductor structure [6-9], which is like conventional MOS structure.

Throughout this dissertation, the effort to enhance mobility of BSO is described in five chapters. The first is this introductory chapter, describing the outstanding advantages of BSO materials and previous reports for the transport of BSO in film and devices. The second chapter illustrates the film growth by pulsed laser deposition technique, which is very important to attain high mobility of BSO. The third chapter is about the effort to grow high mobility BSO films on non-perovskite MgO substrate. The study to improve the mobility of BLSO on MgO substrate is investigated and the successful modulation of BLSO channel by HfO_2 gate dielectrics is demonstrated. The fourth chapter is about bandgap engineering of BSO by Hf substitution for extending toward modulation-doped heterstructures. And the fifth chapter describes the most complicated interface in previously mentioned structures in this part, modulation and polarization doped heterointerface, for high sheet carrier density and high mobility in BSO-based electronics. Lastly, the sixth chapter, which is not main focus topic but many experiment efforts were done in my early Ph. D. term, illustrates a try of Ru substitution on $SrSnO_3$ (SSO) and BSO system to make p-type semiconductors.

1.1 Advantages of $BaSnO_3$ materials

BSO is known to form an ideal cubic perovskite structure, in which Sn^{4+} ion is located in the center of the octahedron by six O^{2-} ions and Ba^{2+} ion is at the corner of cubic unit cell as illustrated in Figure. 1.1 (a). And the lattice parameter is 4.116 Å, having lattice mismatch of 5.4 % compared to the mostly used substrate, $SrTiO_3$ (3.9 Å) as Figure. 1.1 (b) [1,2].

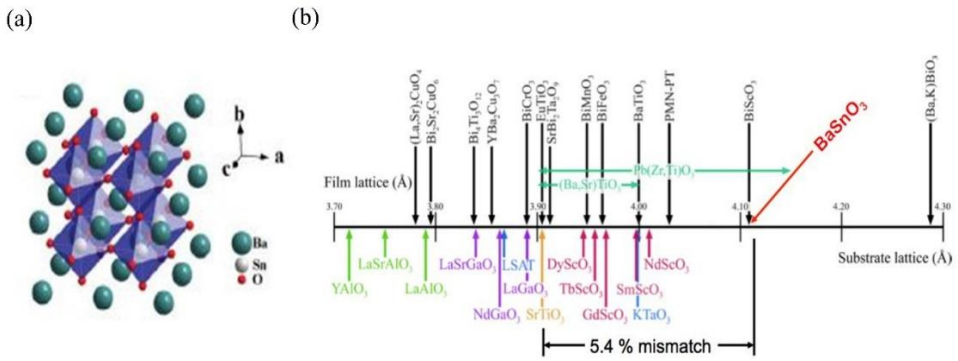

Figure 1.1 : The lattice structure of BSO. (a) The perovskite structure is drawn in the case of BSO, as indicating each atom, separately. (b) The lattice parameters for various perovskite oxides (single crystal)

1.1.1 Wide bandgap

The band structure of BSO shown in Figure. 1.2 (a), is obtained by first-principles density functional calculations with local density approximation (LDA) [2]. According to the folded Brillouin zone of the 3X3X3 supercell, the valence band maximum is located at R and M points while the conduction band minimum at Γ point, indicating BSO as an indirect bandgap materials. And the bandgap value about 1 eV from band structure indicates that BSO is an insulator without any doping.

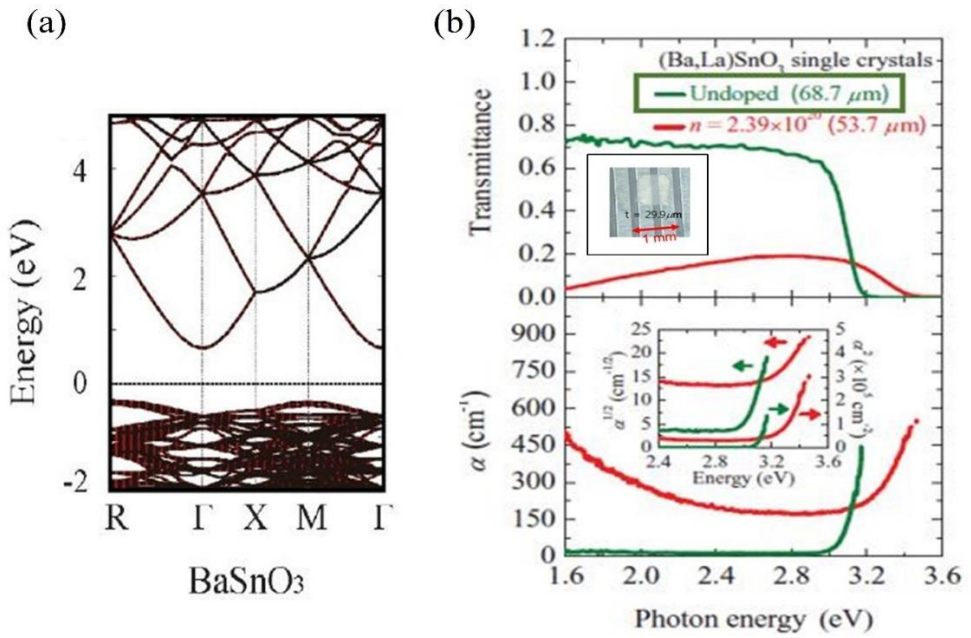

Figure 1.2: (a) The band structure of BSO from DFT calculations based on LDA approximation (3X3X3 supercell) (b) Transmittance and absorption coefficient (α) as varying photon energy for BSO single crystal (green) and BLSO single crystals (red)

While it is well known that the bandgap calculated by the band calculation based on the LDA approximation often underestimates the actual gap [28], the transmission and optical absorption spectra for BSO single crystal (green line) with thickness of 68.7 μm from Figure 1.2 (b) [2], shows its transmittance about 0.71 in the visible region (1.8-3.1 eV), convincing BSO as a WBGs. The inset describes the optical transparency of grown single crystal of BSO with size about 1 mm. The indirect and direct band gaps determined from experimental result by $\alpha^{0.5}$ and α^2 $vs. hv$ fitting, are 2.95 and 3.10 eV, respectively.

Among various applications using the advantages of wide bandgap of BSO, fully solidified perovskite solar cell is recently investigated using BLSO as an electron-transporting layer (ETL) [29]. A solar cell is an electrical device, converting the energy of light into electricity, appealing as a renewable energy generation and storage devices for new generation. As illustrated in Figure 1.3 (b), the created

electron-hole pair by sunlight moves to each end metal contact to generate current through external load. Because usual metal electrodes are opaque, reducing power conversion efficiency (PCE) in solar cell, TCOs such as In_2O_3:Sn [5], SnO_2 [30], ZnO [31] are appropriate, having both transparency and conductivity. Usual solar cells use Si pn-junction to make electron-hole pair, but perovskite materials based on lead halide ($CH_3NH_3PbX_3$; X is I and Br) as dyes have shown remarkable increase of PCE, appealing as an important candidate for photovoltaic devices [32,33]. In Figure 1.3 (c), the superior performance of perovskite solar cell fabricated with BLSO as an ETL is presented in photocurrent density-voltage (*J-V*) characteristics and compared with mesoporous TiO_2, which is a typical ETL for highly efficient perovskite solar cell. The PCE is 21.2 % for using BLSO as a TCO and 19.7 % for TiO_2, which is attributed by higher conduction band minimum, higher electron density, and reduced carrier recombination. And experiment for photostability under light illumination describes a greater resistance against photodegradation than TiO_2 in Figure 1.3 (d), making closer to a commercialization of perovskite solar cell.

Apart from the transparent electronics using its wide bandgap of BSO, another potential area will be high temperature and power electronics [10-12]. WBGs can perform in a high temperature without losing their electrical property due to its wide bandgap, so it can function at ambient temperature without external cooling, beneficial for the automotive, aerospace, and energy production industries. Moreover, its high breakdown voltage makes higher doping levels achievable and higher saturation drift velocity makes possible to operate at higher switching frequency. In turn, the lower conduction loss and lower switching loss can enable breaking the limit of silicon-based power electronics, e.g. radio-frequency application and energy production like photovoltaic inverter technology. Already WBGs such as SiC and GaN are commercially available, so BSO can go beyond TCO, if much effort to achieve higher efficiency for high temperature and power device requirement are done.

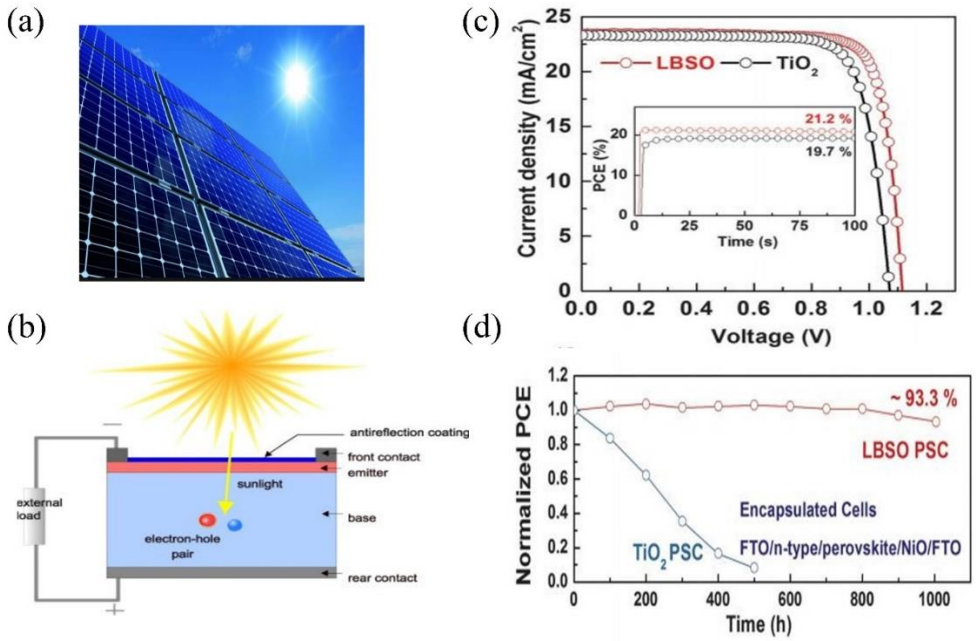

Figure 1.3: Application for solar cell (a) Solar panels. (b) Cross section of solar cell (c) J-V curves and PCEs at a maximum power point for the best performing BLSO and TiO2 based perovskite solar cell. (Au/PTAA (hole-transport layer/$MAPbI_3$/BLSO/SnO_2:F and Au/PTAA/$MAPbI_3$/TiO_2/SnO_2:F) (d) Long term photostability test under AM 1.5G illumination with a metal-halide lamp, including UV radiation for BLSO and TiO_2-based perovskite solar cell. (SnO_2:F/BLSO/$MAPbI_3$/NiO/SnO_2:F and SnO_2:F/TiO2/$MAPbI_3$/NiO/ SnO_2:F)

1.1.2 Thermal stability

Thermal stability, which is the stability of material under repeated thermal cycles in the environment of device fabrication or operation, is a very important property for reliability in application or foothold in material science. Especially, many oxide materials suffer from oxygen stability because oxygen vacancies are easily formed, making difficult to reliability in device application and even to uncontrollability of carrier density.

At the earlier papers reporting the thermal stability of BSO, Ostrick *et al*. [34] measured the carrier density of BSO ceramics at several high temperatures under O_2-

poor environment. According to the experimental results, the variation of the carrier density of BSO was less than 10^{14} cm^{-3} at 700 °C. The stability is also confirmed by the conductivity variation of BLSO films at 530 °C under Ar, O_2, air atmosphere in Figure 1.4 [1]. Annealing in Ar gas resulted in resistance change of only about 8 % in 5 hours and a tiny increase of 1.7 % in air for 100 nm-thick film. Although annealing at high temperature in O_2 -poor environment makes the oxygen to diffuse out of the film, the slight change of resistance directly reflects the unusual stability of oxygen atoms in BSO. For comparison, ZnO films have shown about one order of resistance change in air under similar annealing temperature and time condition [35].

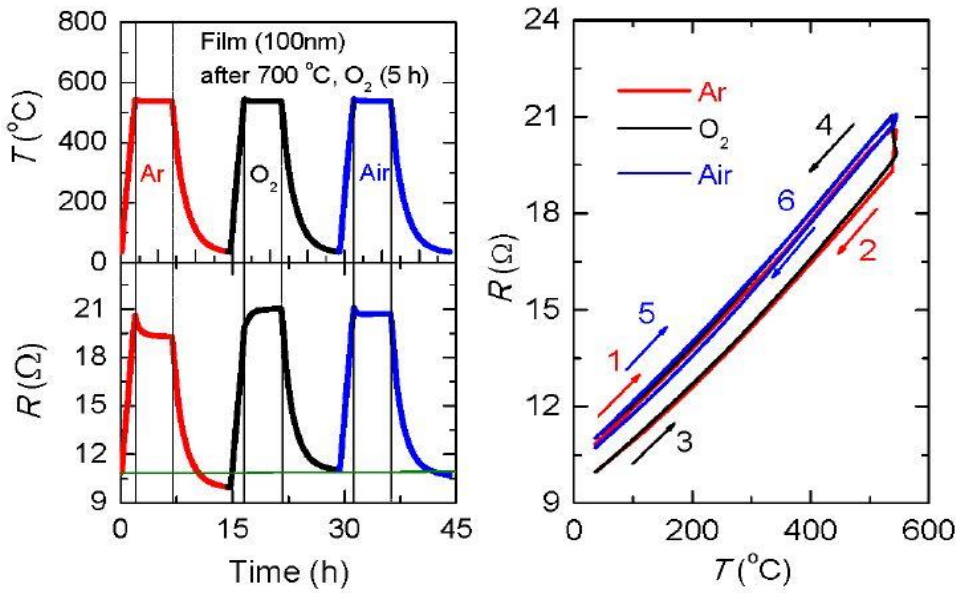

Figure 1.4: Annealing experiment for 100 nm- thick- 4 % La- doped BSO films. The left upper panel is temperature and gas atmosphere condition and the lower panel is the resultant resistance. The right plot is the corresponding resistance vs. temperature from left panel.

The oxygen diffusion constant, a measure of oxygen stability, for various complex oxides, is shown in Figure 1.5. The value for BSO is 10^{-15} cm^2s^{-1} [1], which is lower

value about ten order than $SrTiO_3$, well- known perovskite oxides. Since lower oxygen diffusion constant means that it takes much time for oxygen to get out of film, the clearly lower value for BSO indicates its unusual stability, e.g, the value of perovskite oxides are on the order of 10^{-8} for titinates [36], 10^{-11} for cuprates [37], and 10^{-13} cm^2s^{-1} for manganites [38] at similar temperature region. On the other hand, the dielectric properties also support this thermal stability of BSO; stability of oxygen stoichiometry [39].

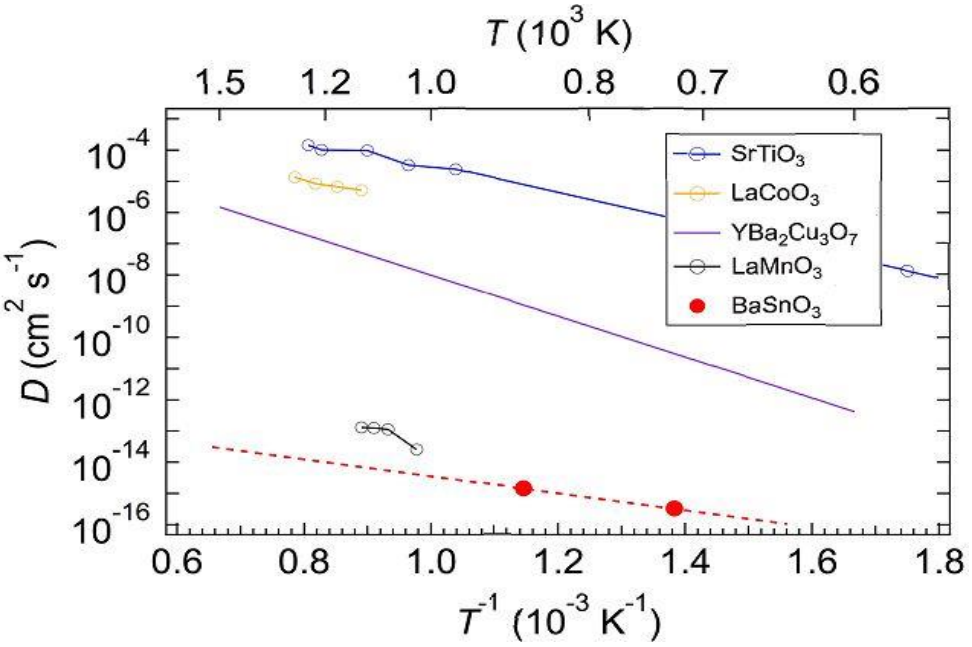

Figure 1.5: Oxygen diffusion constant (D) for various oxides

1.1.3 High mobility

Figure 1.6 illustrates room temperature mobility (μ) vs. carrier density plots for typical semiconductors, e.g, GaAs [40], GaN [41], Si [42], ZnO [43], $SrTiO_3$ [44,45] and BLSO [1]. It is noteworthy that the μ of BLSO single crystal is about 320 $cm^2V^{-1}s^{-1}$, higher than GaN, well-known WBGs, at carrier density above 10^{19} cm^{-3}. Moreover, this is the highest value among WBGs in the degenerate doped regime, e.g, ~100 for GaN [46], ~160 for In_2O_3 [47], ~50 for SnO_2 [48] and ~100 $cm^2V^{-1}s^{-1}$ for

ZnO [49]. Meanwhile, the non-degenerate regime for BLSO single crystal is absent

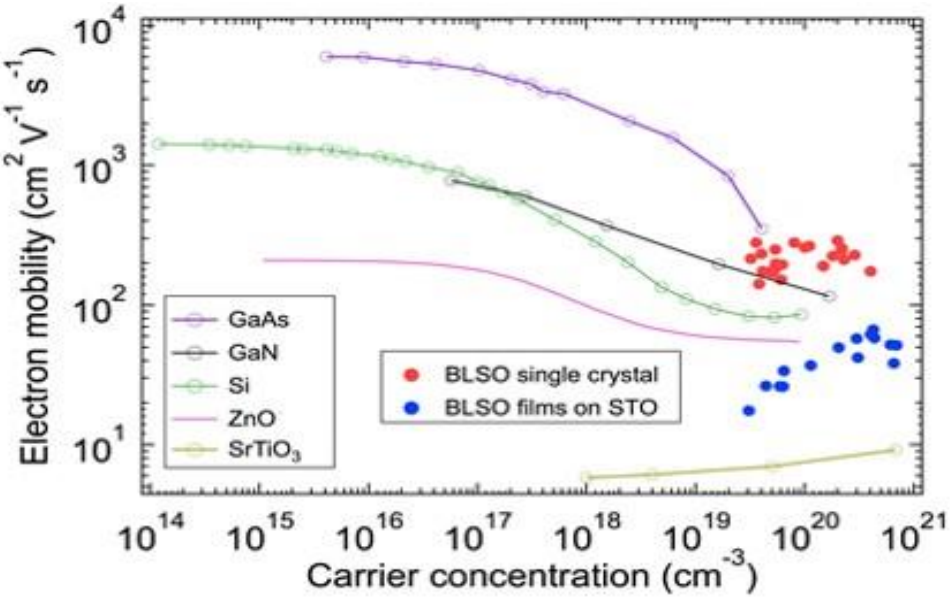

Figure 1.6: Mobility against carrier concentration for BLSO and other semiconductors.

since it is hard to control intrinsic defects related to oxygen vacancies during synthesis of single crystal at high temperature, yet. And smaller values for BLSO films than single crystals are believed by high density of dislocations acting as a charge traps [1].

Although much effort is needed to control the non-degenerate region, sensitive to defects, the transport property in degenerate regime is crucial since high on-state current requires both high μ and high carrier density. But for perfect controllable switching, requirement for semiconductor industry, the transport region in case of BSO should be wider. Until now, it seems that the boundary between off- and on-state is clearly related to defect states, much higher density (~10^{19} cm^{-3}) than conventional semiconductors, in thin film transistor based on BSO channel, so making hard to regulate the band bending physics in BSO. The defect control is most important key to its application as semiconductor.

The μ can be written by;

$$\mu = \frac{e\tau}{m^*} \tag{1.1}$$

where, τ and m^* is scattering time and effective mass of conduction band, respectively [50]. The first reason for high μ in BLSO is a small effective mass about 0.42 m_0 [18], due to highly dispersive band mainly composed of Sn 5s orbital. While transition metal oxides usually have flat conduction band composed of d orbital, BSO has a dispersive band by s orbital character and even smaller value of 0.06 is recently

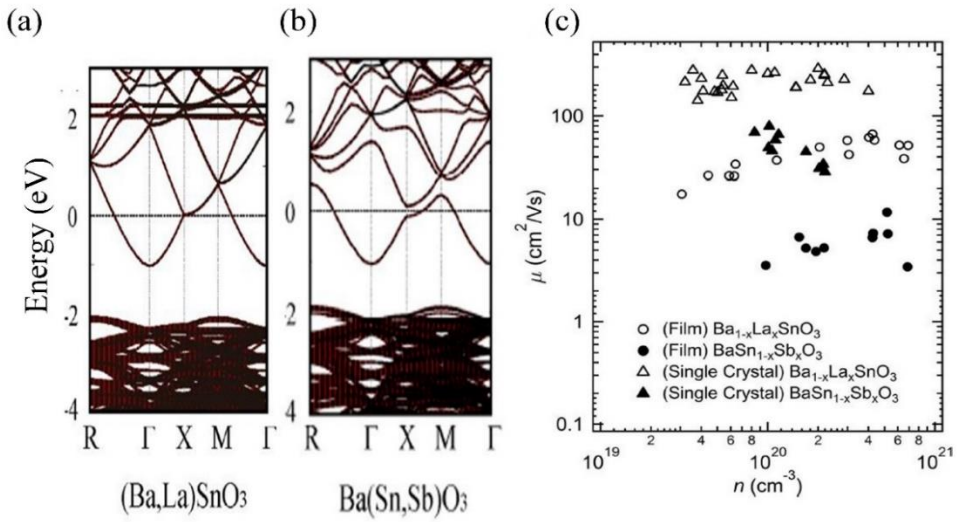

Figure 1.7: A site (by La^{3+}) and B site (by Sb^{5+}) doping for BSO. (a~b) The band structure of 3.6 % La-doped BSO and 3.7 % Sb-doped BSO are obtained by first-principles calculations with $(3 \times 3 \times 3)$ unit cells. (c) Comparison between transport properties of BLSO and BSSO by plotting of mobility vs. carrier concentration for single crystal and film.

reported [51]. However the value is not particularly small to explain its high μ since μ is 0.067 for GaAs [52], 0.22 for GaN [53], 0.259 for Si [54], 0.23 for ZnO [55] and 0.3 m_0 for In_2O_3 [56]. So the scattering time is believed to be a major reason.

The most probable reason for high μ is La dopant on A site, somewhat like modulation doping in atomic scale. Because Sn 5s states and Sn-O antibonding character states mainly constitute bands near Fermi level in Figure 1.7 (a), La^{3+} ion

substation on Ba site maybe rarely interrupt the electron channels, only acting as an electron donor. This argument seems valid when comparing Sb-doped BSO in Figure 1.7 (c). Sb^{5+} ion substitution on Sn site affects lower mobility compared to BLSO for each single crystal and epitaxial film, and change of band dispersion near Fermi level in Figure 1.7 (b). This phenomena is only possible for perovskite oxide with two cation dopant site, because most semiconductors have strong covalent bonding with one or two species of atom comprising main transport-relevant band.

Also the ideal Sn-O-Sn bond angle of 180° contributes to low scattering rate for cubic BSO, since orthorhombic SSO shows a lower μ [57,58] possibly due to distorted bonding angle about 160° [59]. And reduced dopant scattering due to rather a high dielectric constant about 20 [60] and possibly small phonon scattering can attribute to low scattering rate.

1.1.4 All epitaxial heterostructures with multiple functionalities

The perovskite oxides are known to have a rich variety of functionalities such as superconductivity, magnetism, ferroelectricity, multiferroicity, large polarization, and piezoelectricity, e.g, $BaTiO_3$, $Pb(Zr,Ti)O_3$, $BaFeO_3$, $YMnO_3$, etc [13-17]. Many electronic device architectures require multiple functionalities enabling to extend the amount and types of processing data, e.g, nonvolatile ferroelectric random access memory (FeRAM) [61], spintronics [62], and micro-electromechanical system (MEMS) [63]. FeRAM has a similar structure as dynamic random access memory (DRAM), but uses a ferroelectric layer instead of a linear dielectric layer, so consume less power, not requiring refresh process of every cell. Moreover, it has a lower power usage, faster write performance, and a much greater read/write endurance (10^{10}~10^{14} cycles) compared to flash memory. Following the discovery of the giant magnetoresistance, electron spin have been employed as a new degree of freedom for electronics, extending toward spintronics. Switching a ferromagnetic state is possible

by various means such as using current induced magnetic field, spin transfer torque based on high spin polarized current density, spin-orbit interaction, and even just

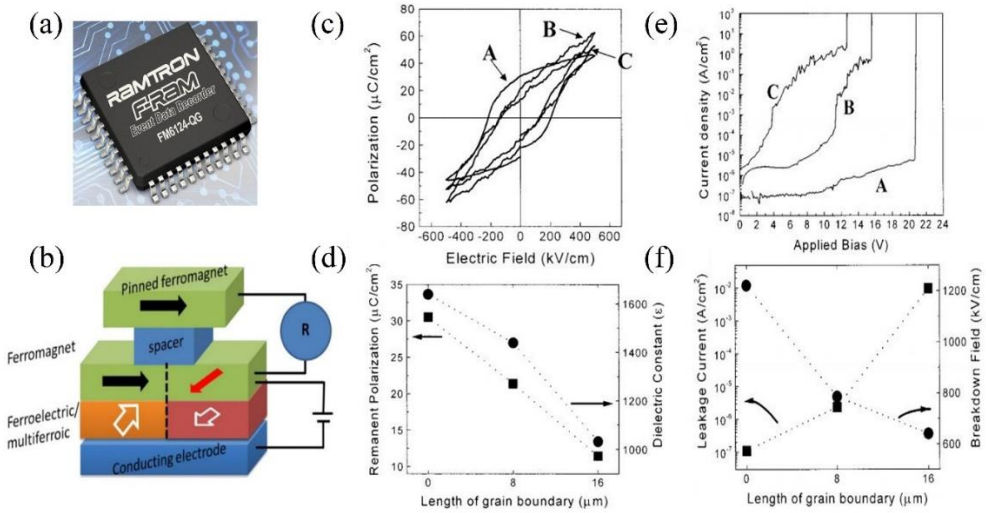

Figure 1.8: (a) An example of FeRAM chip. (b) Multiferroic heterostructures for spintronics (multiferroic magnetoelectric memristor concept). (c) Ferroelectric hysteresis loop for samples within grains (A), on the line grain-boundary (B), and at the grain-boundary intersection (C). (d) Variation of the remanent polarization and dielectric constant with the length of grain boundaries. (e) Leakage current density vs. applied bias for A, B, and C. (f) Variation of the breakdown field and leakage current density at 5 V with the length of grain boundaries

simple a voltage bias is adequate especially for multiferroic materials. In addition, a new fundamental two-terminal elements, memory resistor (memristor) [64] being achieved with different physics, continuously tunable resistors, which observed in many transition metal oxides, ferroelectric heterostructures, and spin valve heterostructures, helps to be smaller and more easily addressable than conventional three-terminal transistor with minimal energy dissipation. Also the highest-performing piezoelectric MEMS with $Pb(Zr,Ti)O_3$ have been fabricated, jumping over the drawback of Si. [65]

To integrate this functionalities into devices, epitaxial growth is most important because achieving a working device requires the control of material properties such as ferroelectric/ferromagnetic coercive field, ferroelectric polarization, domain

structure, interface trap concentration, etc. As shown in Figure 1.8 (c~f) [66], serious degradation can be observed in terms of polarization, leakage current, breakdown field, and fatigue characteristics when grain boundaries are included in $Pb(Zr,Ti)O_3$. To manipulate the functional perovskite oxide in Si-based electronics, there are limitations in the choice of materials and proper buffer oxides due to a difficulty on epitaxial growth. However, if BSO-based electronics with a high mobility channel is incorporated, all epitaxial heterostructure devices with multiple functionalities will be realized.

1.1.5 Optoelectronics (to be continued)

Additionally, oxygen stability of BSO leads to very stable pn-junctions after repeated high-bias and high-temperature thermal cycling as Figure 1.9 [67]. Although the study for optoelectronics function for BSO is needed, it can be expected that pn-junction based on BSO system may emit light in the near future due to small difference of bandgap energy (~0.15 eV) between indirect and direct [2].

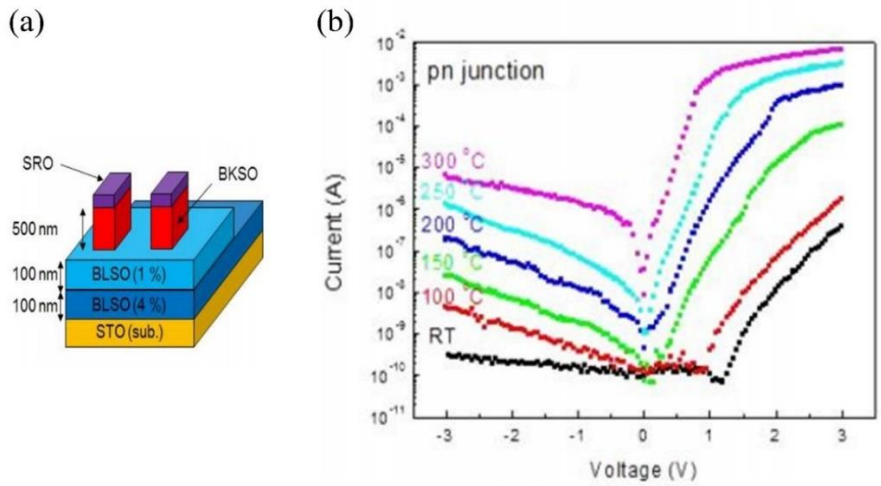

Figure 1.9: pn-junction using K-doped BSO as a p-type semiconductor and La-low doped BSO as a n-type semiconductor (a) Schematics of the BKSO/BLSO pn junction (b) Logarithmic I-V plot at various temperatures for 11 % K-doped BSO/BLSO pn-junction

1.2 Previous study on $BaSnO_3$

Numerous dopants in BSO system, such as $Ba_{1-x}Sr_xSnO_3$ [18] and $BaSn_{1-x}M_xO_3$ (M: Cr, Co, Mn, Te, Si, etc) [19-23], have been studied, but the transport property of BLSO and $BaSnO_{3-x}$ is mainly introduced in this chapter because the high μ have been presented by La doping, ever since published in Applied Physics Express by H. J. Kim *et al*. [1]

1.2.1 The transport property of films

Figure 1.10 (a) [1] illustrates the different scattering mechanism for limiting the transport of BLSO single crystal and film. In BLSO single crystal, phonon and ionized dopant scattering can affect in transport. As a result, $\mu \propto n^{-1}$ tendency implies that μ dominantly depends on the number of scattering centers, with a small screening length (Debye length) due to degenerately doped regime. While ionized impurity scattering is dominant in single crystal, the high room temperature μ = 320 $cm^2V^{-1}s^{-1}$ is found at carrier density (n) of 8.0×10^{19} cm^{-3} and 620 $cm^2V^{-1}s^{-1}$ at 2 K.

On the other hand, in case of thin films, μ decreases in a low doping range smaller than $n = 4.0 \times 10^{20}$ cm^{-3} with a tendency of $\mu \propto n^{0.5}$, particularly lower value than single crystal, and then follows the single crystal trend at higher n, e.g., $n = 6.8 \times 10^{20}$ cm^{-3}. As illustrated in Figure 1.10 (b), there exists a large density of threading dislocations (TDs) about $10^{10} \sim 10^{11}$ cm^{-2} [68], so that every few tens of nanometers one or two full TD cores reach the surface of the film. Even though the film is epitaxially grown on $SrTiO_3$ substrate, the large lattice mismatch about 5.4 % between film (4.116 Å) and substrate (3.9 Å) makes TDs, acting as strong a charge traps and scattering centers with reducing n and μ simultaneously. But highly doped region, the scattering by ionized dopants seems to dominating. The tendency of $\mu \propto n^{0.5}$, is well known in the transport in GaN thin films [69-72], governed mainly by

dislocations.

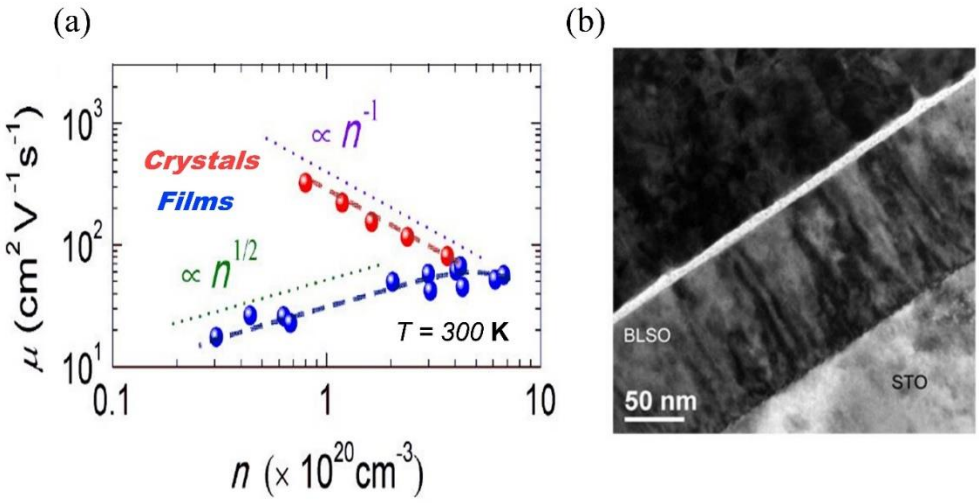

Figure 1.10: (a) μ as a function of n at 300 K for BLSO thin films and single crystals. (b) A cross-sectional transmission microscope image of a BLSO film on $SrTiO_3$ substrate.

To improve μ in the thin films, various studies were investigated using diverse substrate [24-27], growth condition [68], buffer technique [6], and deposition method [25] exhibiting μ ranging from 10~150 $cm^2V^{-1}s^{-1}$. First of all, lattice-mismatched substrate will be worthwhile to reduce the density of TDs, and various substrate, e.g, $SrTiO_3$, $SmScO_3$, $PrScO_3$, $LaAlO_3$, and $BaSnO_3$, etc. were selected. Second, varying growth temperature yielded different TD densities, that is, BLSO on $SrTiO_3$ substrate calculated from AFM etching surface images reveals TD density of 8.9×10^{10} and 4.9×10^{10} cm^{-2} at growth temperature of 600 °C and 750 °C, respectively [68]. In turn, simultaneous increase of μ and n are observed as increasing growth temperature in Figure 1.11 (a). Third, buffer technique using undoped BSO layer directly on lattice-mismatched substrate is investigated, which is widely used in GaN thin films with a few μm GaN template on sapphire or Si substrate [69]. The buffer layer reduces the density of TDs in the above film layer, and enhancement of μ is expected in Figure 1.11 (b), shown in black circles for BLSO (100 nm)/BSO (100 nm)

and red circles for BLSO (100 nm) on $SrTiO_3$ substrate. Lastly, while most of films are epitaxially grown by pulsed laser deposition (PLD), oxide molecular beam epitaxy (MBE) can improve stoichiometry of films with almost matched-rate in each atom in $Ba_xLa_{1-x}SnO_3$ films, since atomic layer deposition is possible. Although μ is limited by TDs in thin films, the recent highest value 150 $cm^2V^{-1}s^{-1}$ at $n = \sim 7 \times 10^{19}$ cm^{-3} reported by oxide MBE group [25] implies there are possibly cation off-stoichiometry in thin films by PLD.

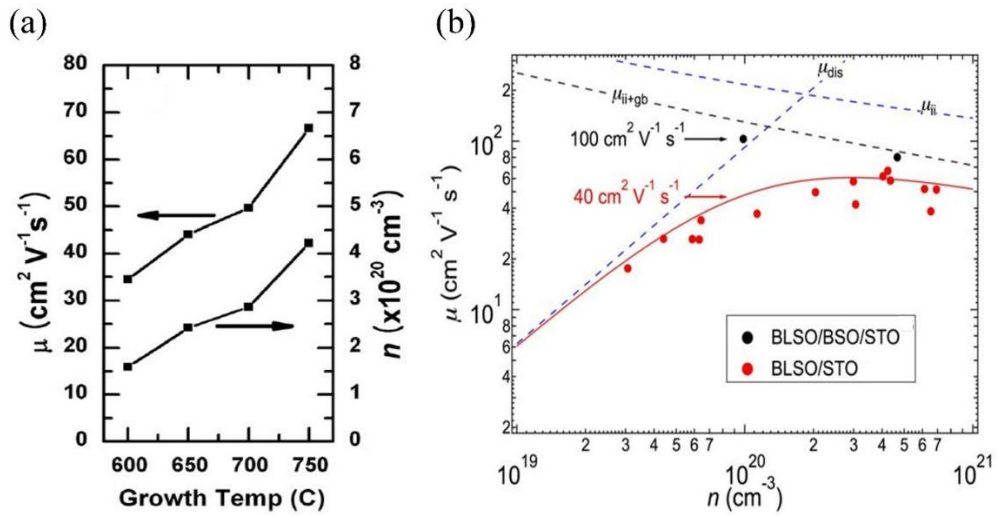

Figure 1.11: (a) μ and n of BLSO on $SrTiO_3$ substrate at various temperatures. (b) Buffer effect on μ in BLSO films on $SrTiO_3$ substrate.

1.2.2 The transport property of devices

Until now, the carrier modulation of BSO channel by field effect have been investigated with a structure of metal-insulator-semiconductor [6-9]. The first paper, demonstrating successful field effect transistor (FET) based on BLSO channel by C. Park *et al*. [6], employs a device structure with Al_2O_3 as a gate dielectrics, and In_2O_3:Sn as electrodes as shown in Figure 1.12 (a). Channel length and width of 140 and 60 μm, respectively, are designed by deposition using stencil masks. At room temperature, the field effect mobility (μ_{FE})of 17.8 $cm^2V^{-1}s^{-1}$ and I_{on}/I_{off} ratio higher

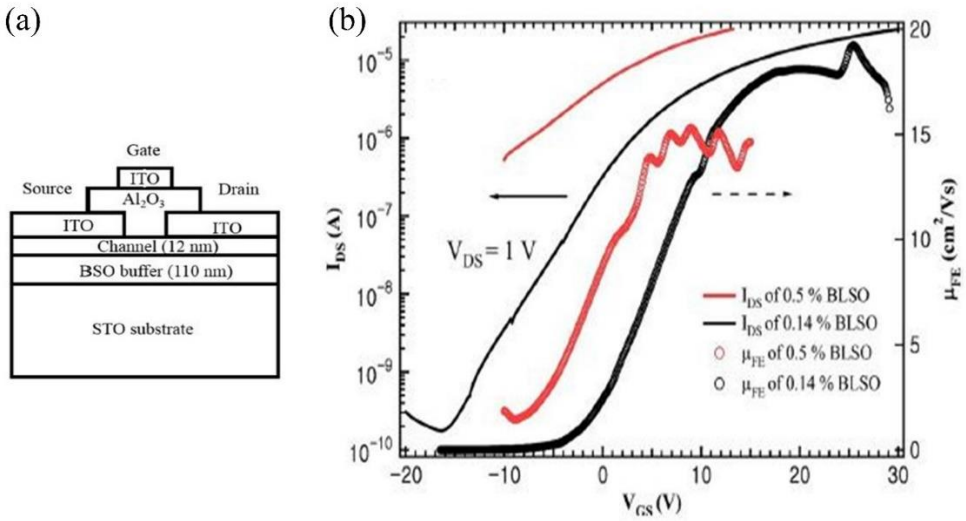

Figure 1.12: FET based on BLSO channel with Al_2O_3 dielectrics. (a) Cross sectional diagram of FET device. (b) Transfer characteristics, I_{DS}-V_{GS} and μ_{FE}–V_{GS} at V_{DS} = 1 V.

than 10^5 for V_{DS} =1 V are measured, which are higher than previously reported on other perovskite oxides in Table 1. The aging effect on the transfer characteristics after two months in ambient air indicates no appreciable change, also consistent with the stability of the BSO materials. Other gate dielectrics such as HfO_2, $BaHfO_3$, $LaInO_3$ are used to FET based on BLSO channel with μ_{FE}, I_{on}/I_{off} ratio, subthreshold swing (S), and trap density (D_{it}) presented in Table 1.

Table 1: A comparison of FET device performance for perovskite oxides

Dielectrics/Channel	μ_{FE}	I_{on}/I_{off}	S(V dec^{-1})	D_{it} (eV^{-1} cm^{-2})	References
Al_2O_3/$KaTiO_3$	0.4	10^4			[73]
Al_2O_3/$SrTiO_3$	0.1	10^2			[74]
$CaHfO_3$/$SrTiO_3$	2	~10^5			[75]
Al_2O_3/BLSO	17.8	>10^5	3.2	4.38×10^{13}	[6]
HfO_2/BLSO	24.9	>10^6	0.42	9.89×10^{12}	[8]
$BaHfO_3$/BLSO	53.7	10^7	0.8	2.06×10^{13}	[9]
$LaInO_3$/BLSO	90	10^7	0.65	8.67×10^{12}	[7]

Meanwhile, carrier modulation of undoped BSO is impossible due to its very insulating property in our group under Prof. K. Char, but Fujiwara *et al*. [76], reports FET based on BSO channel. They used $Sr_{0.5}Ba_{0.5}SnO_3$ (SBSO) buffer layer on $SrTiO_3$ substrate and high temperature annealing process to obtain an atomically smooth surface. Also they fabricated FET with a structure of parylene/SBSO/BSO(channel) to reduce interface scattering, which is a main reason of degradation in transport in FET since the conducting interface is only a few nm. Figure 1.12 shows μ vs. n_{3D} for BSO FETs and FETs, films, and single crystals of BLSO. The two-dimensional transport in FET was converted to three-dimensional carrier density (n_{3D}) by taking into account the wave function distribution. There are two appreciable points from their result. One is much steeper rise in μ in sample A (parylene/BSO interface) compared to BLSO FET (Al_2O_3 or HfO_2/BLSO interface), implying enhancement of μ by excluding chemical doping. And the other one is the importance of manipulation of the channel layer surface. When comparing sample A and C (parylene/SBSO/BSO), the increase of μ is remarkable. Although n_{3D} of sample A and C is limited by leakage of dielectrics in Figure 1.13, the recent report by Fujiwara *et al*., presents μ of 300 $cm^2V^{-1}s^{-1}$ at 50 K with the aid of electric double layer technique. First of all, because the science of oxide TFT is based on the band bending in just few nm scale, the study for improvement of interface is needed for better performance in BSO-based electronics.

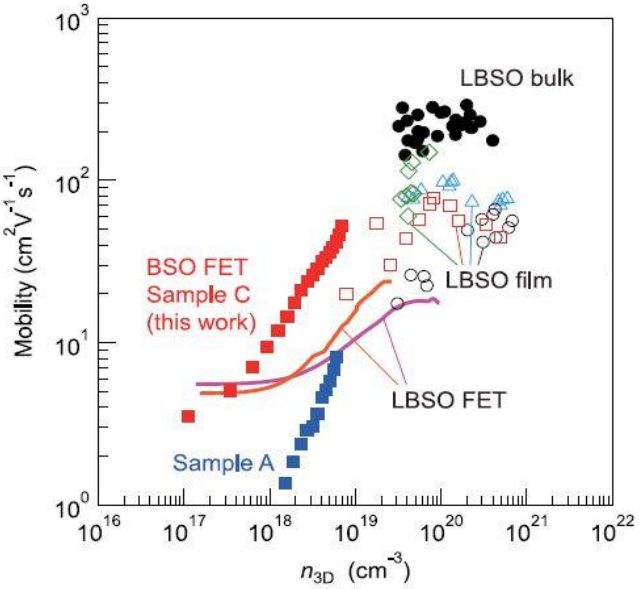

Figure 1.13: μ vs. n_{3D} for FET based on BSO and BLSO channel. Also the data for BLSO thin films and single crystal are shown.

Chapter 2

Growth of thin films and FET devices by pulsed laser deposition

In this dissertation, all the films and FET devices based on BSO are grown by pulsed layer deposition method. As illustrated in Figure 2.1 describing μ of BLSO films by various groups[24,27,77,78], PLD technique is very crucial to achieve high μ. The red and black points are data for our group [1], first reporting high μ of BLSO thin films and FET devices.

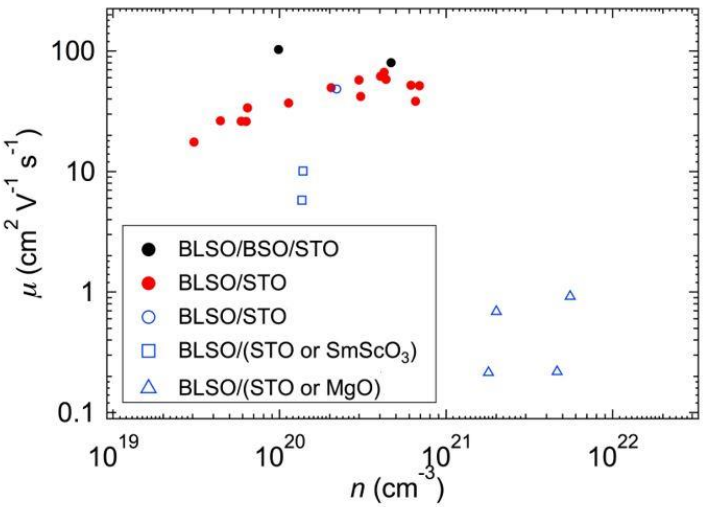

Figure 2.1: μ in BLSO films made by various groups.

2.1 Target preparation

First of all, targets of the material to be deposited on substrate should be prepared. At the initial state, polycrystalline BSO and BLSO were synthesized in our laboratory. The procedure is, a stoichiometric mixture of high-purity $BaSnO_3$, SnO_2, La_2O_3 powders is calcined at 1250 °C for 6 hours and finally fired at 1400-1450 °C for 24 hours after several intermediate grindings. The polycrystalline target is investigated by X-ray diffraction (XRD) to confirm a complete solid-reaction.

But the targets from Toshima manufacturing Co. have been frequently used since 2015. Figure 2.2 (a) describes usual BSO target with a diameter of 0.99 and a thickness of 0.25 inch. The purity is about 99.9 % and the density is 60~70 %. The datasheet from Toshima in Figure 2.2 (b) convinces a BSO phase, comparing lower green reference data. The procedure from Toshima is mixing raw materials, synthesizing (their special technique), checking XRD, grinding for small powder, hot pressing, and lastly shape processing.

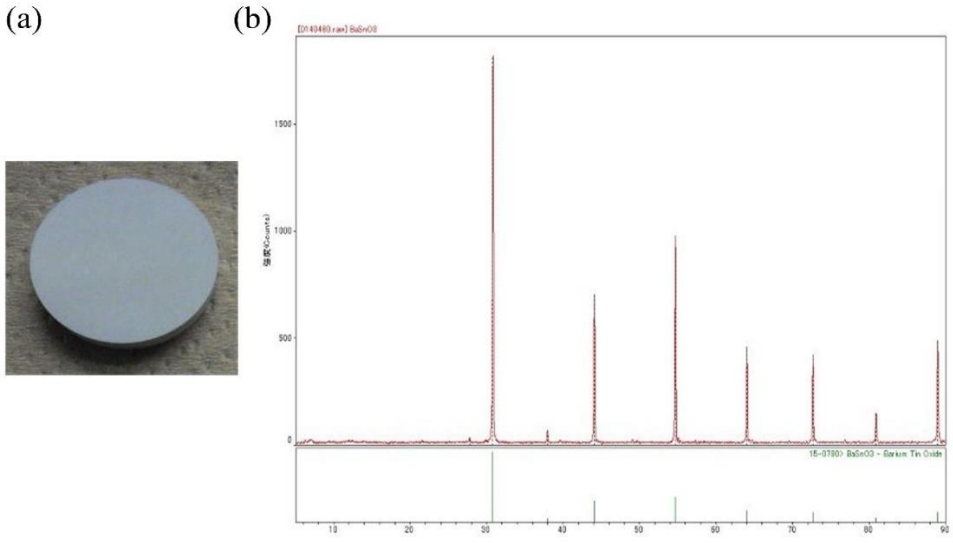

Figure 2.2: (a) Polycrystalline BSO target for PLD (b) XRD measurement for BSO target

2.2 Pulsed laser deposition

Pulsed laser deposition (PLD) is a physical vapor deposition technique [79], where a high power pulsed laser beam is focused into a target material in a vacuum chamber or in the presence of a background gas. The ablated plume then is deposited on a substrate. The process of PLD is generally divided into five stages; laser absorption on the target surface, laser ablation, dynamics of plasma, deposition on the substrate, nucleation and growth of film. Each step is crucial for the crystallinity, uniformity, and stoichiometry of film.

.

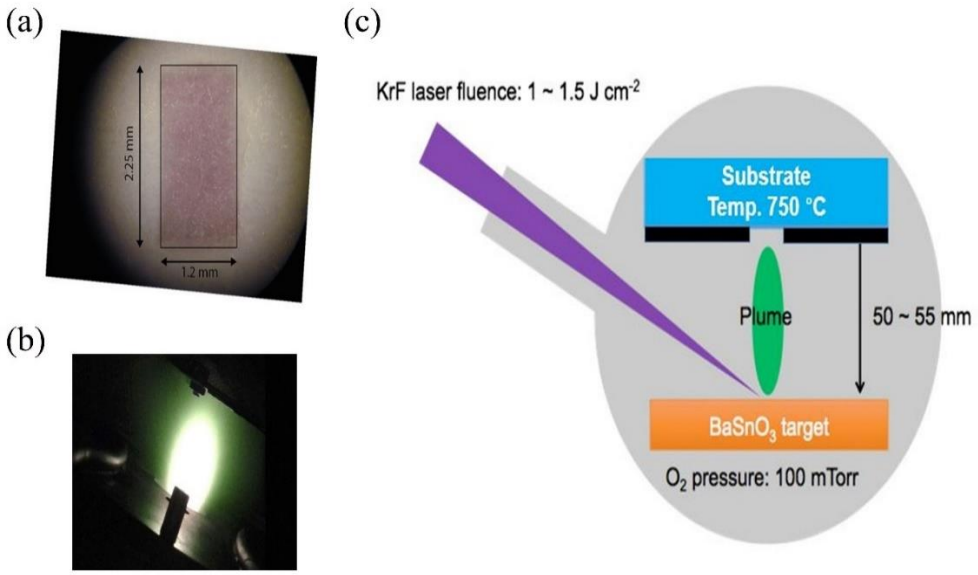

Figure 2.3: Schematics of PLD. (a) Spot. (b) BSO plume. (c) A laser ablation system in our experiment.

Figure 2.3 (a) shows spot, being absorbed on the target surface, and (b) is a photographic record for BSO plume. Actually, focusing spot with a uniform density from a distant aperture was a key for PLD and it is a time-consuming project. Figure 2.3 (c) describes PLD system employed in the following experiments. The wavelength of 248 nm from KrF excimer is used and the energy fluence of absorbed by target is 1~1.5 J cm^{-2}. The distance between target and substrate is 50~55 mm and the temperature for substrate is 750 °C for adequate arrangement of each atom. The O_2 base pressure is maintained by 100 mTorr to supply oxygen in the growth of $BaSnO_{3-x}$

2.3 Fluence and distance dependence and target tracks

The distance between target and substrate and energy fluence absorbed by target surface affects the transport property of BLSO as Figure 2.4. At 52.5 mm, 4 % La-doped BSO shows increasing La activation rate until mid-1.5 J cm^{-2}, and decrease of n above 1.6 J cm^{-2}. The μ is maximized in mid-1.4 J cm^{-2}, and saturated above 1.5 J cm^{-2}. In the case of distance of 52.5 mm, the best condition for fluence will be 1.4~1.5 J cm^{-2}. On the other hand, when increasing a distance to 60 mm, the overall property is degraded at the same fluence. The best condition for ablation, the proper selections of fluence and distance are needed.

The repeated ablation makes the target surface is different from before, so that the ablated species may have a different stoichiometry and bonding character. So the uniform ablation on the target surface is very important, especially, in the low doping regime weak to defects. Our laboratory uses two kinds of motors to rotate uniformly targets, that is, DC motor and stepping motor. DC motor makes the target to revolve, and stepping motor to rotate on its axis as shown Figure 2.5 (a). In one period, 11 tracks are ablated on the target surface by stepping motor with staying time proportional to 1(innermost radius):2:4:7:9:11(outermost radius). And the location of

center of oscillation affects uniform ablation as Figure 2.5 (b) during operation of two motors. The center of oscillation is located at out of center of circular target in the case of 120°. This, in turn, results that 70 grinding of target still leaves ablated spots but just 12 grinding is necessary to remove spots in the case of 60°. The degree means a target location since we use 6 targets at 0,60,120,180,240,300°.

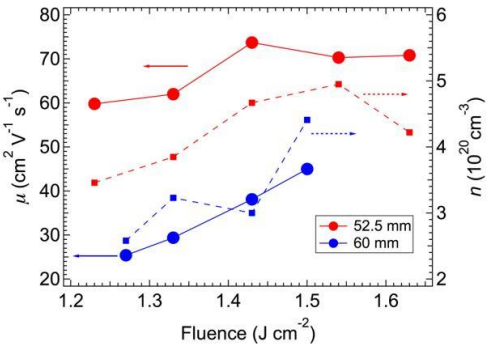

Figure 2.4: Energy fluence and distance dependence of 4 % La-doped BSO (100 nm) on $SrTiO_3$ substrate.

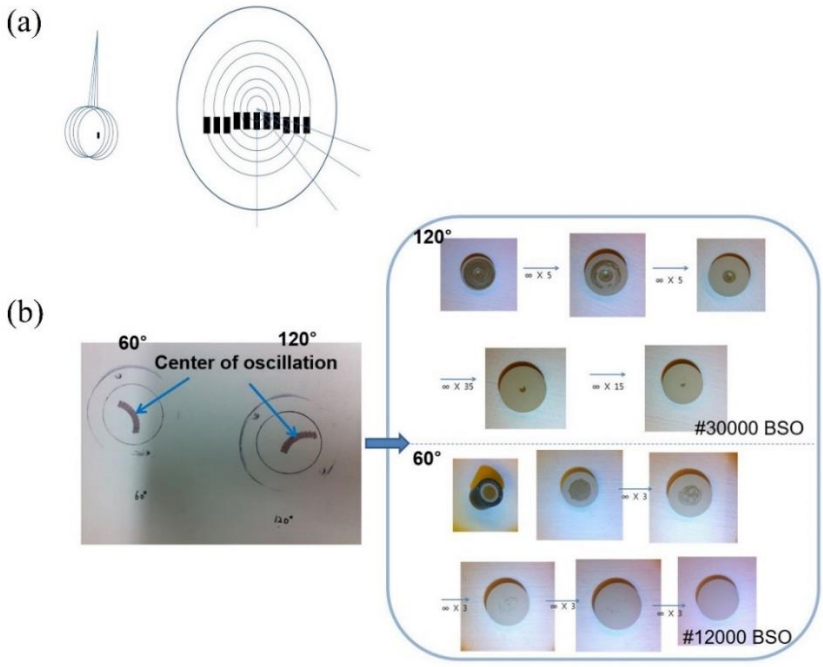

Figure 2.5: Target tracks. (a) Target tracks by stepping motor. (b) Center of oscillation for stepping motor affects uniform ablation on target surface.

2.4 Mask effect

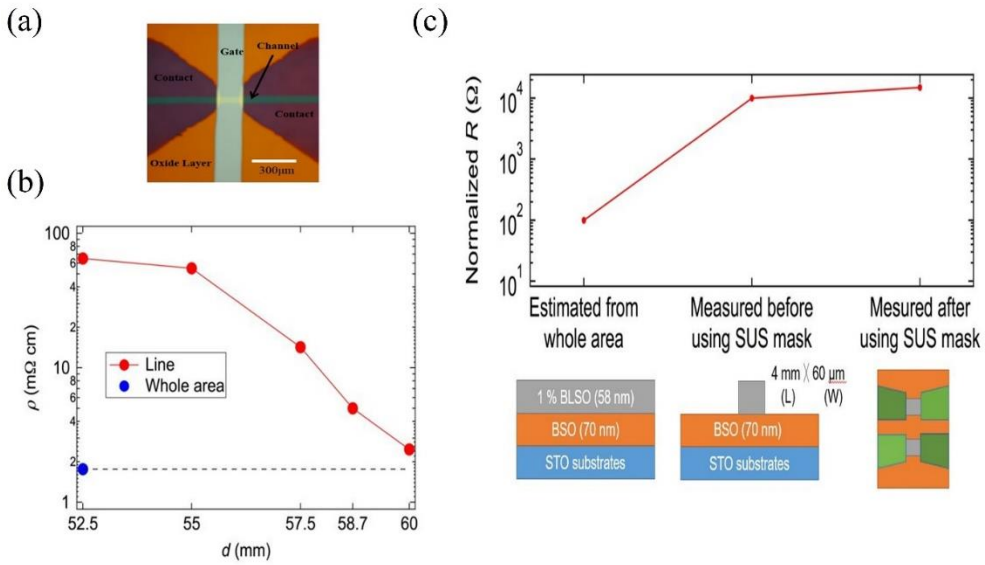

Figure 2.6: Mask effect (a) The top view of typical fabricated FET. (b) Resistivity vs. distance for films with/without Si mask. (c) Normalized sheet resistance of films without mask, with Si line mask, and with SUS mask.

.

BSO is a stable material and chemical etching is not studied, yet. To fabricate device with more or less 100 μm scale, stencil mask of Si and stainless steel (SUS) is used. But high kinetic energy (1~500 eV) of ablated species in the PLD process can eject much impurities from stencil mask. Figure 2.6 (b) describes the decrease of resistivity in lines (1 % La-doped BSO 12 nm/BSO 40 nm/BHO 62 nm on MgO substrate) using a patterned Si mask, as separating the distance between target and substrate. But the films without mask shows no critical distance dependence. Increased distance makes the energy of highly energetic species to decrease, so contamination through mask diminishes. The proper distance for matching the result with/without mask should be found out.

The mask effect is a little more severe when using SUS mask at same distance, as Figure 2.6 (c) with structures of 1 % La-doped BSO 58 nm/BSO 70 nm on $SrTiO_3$

substrate. The normalized sheet resistance, converting for square geometry, increases after Si line mask, in turn, after SUS mask. The two reason can affect the highest resistance by using SUS mask. One is that pattered dimension ($140\ \mu m \times 110\ \mu m$) when using SUS mask is small compared to Si line mask ($60\ \mu m \times 5\ mm$). As the covered region around patterning increases, the contamination would be severe. The other reason is related to the contents in SUS mask, which includes C, Si, Mn, P, S, Ni, Cr, etc. Si line mask is patterned by Si wafers, using SiN passivation layer and KOH etching technique. But SUS mask itself has a variety of impurities than Si wafers, and machined process to be pattered yields jagged edge possibly to be the source of ejection of impurities.

Chapter 3

High mobility $BaSnO_3$ films and field effect transistors on non-perovskite MgO substrate

Since the discovery of BSO as a high mobility TCO, the research efforts to date are mainly limited on films on perovskite oxide substrates such as $SrTiO_3$, $SmScO_3$, $PrScO_3$, $LaAlO_3$, and $BaSnO_3$, etc. Although such perovskite substrates are good in promoting the growth of the perovskite structure, they all suffer from a small size, a small bandgap (3~5.5 eV), a large lattice mismatch and/or oxygen instability, which limits the current BSO research. However, if the films on non-perovskite substrates have a good transport property, BSO research can be accelerated in many areas. The MgO substrate fits well from the above viewpoint due to its availability of wafers in large sizes, its large bandgap (7.8 eV), its relatively smaller lattice mismatch with BSO, its oxygen stability. Although there have been efforts to grow BSO on non-perovskite MgO substrate, they suffered from poor electrical transport properties as Table 3, when considering μ of 10~150 $cm^2V^{-1}s^{-1}$ on perovskite oxide substrate. This chapter presents the efforts to improve μ of BSO, consequently, the realization of high μ BLSO films and FET on non-perovskite MgO substrate.

Table 3: Reports for room temperature μ and n of BSO on MgO substrate

Chemical formula	μ ($cm^2V^{-1}s^{-1}$)	n (cm^{-3})	References
(Ba,La)SnO_3	0.013~0.923	~10^{21}	[27]
Ba(Sn,Nb)O_3	2~20	~10^{20}	[90]
Ba(Sn,Ta)O_3	0.5~5	10^{20}	[91]
$BaSnO_{3-\delta}$	~20	5×10^{19}	[92]

3.1 The material properties of MgO

Figure 3.1 (a) is an example of MgO crystals and substrate. Relatively low economical cost and easiness of availability for large size single crystal help to extend to wafer scale processing and commercialization of grown films. The large bandgap of 7.8 eV in Figure 3.1 (b) is reported via Kramers-Kronig analysis of the reflection data for crystalline MgO [80]. This large bandgap is surely appropriate for application in transparent electronics, in turn, being free from any mid-gap defect states, oxygen stability helps broadening in the area of high temperature and high power electronics.

The crystal structure of MgO is cubic NaCl structure with a lattice constant of 4.2 Å [81]. While most perovskite oxide substrate commercially available has a small lattice parameter as Figure 3.1 (d), compared to BSO (4.116 Å) [1], the large and cubic structure of MgO can lead the bonding angle of Sn-O to be straight, not distorted, attribute to high mobility of BSO films grown on it.

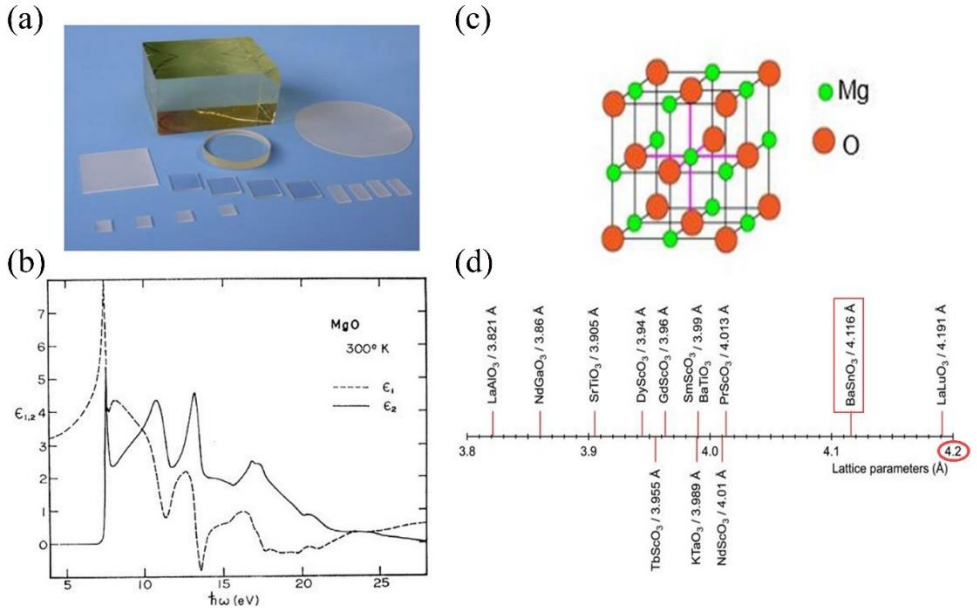

Figure 3.1: (a) An example of MgO crystals and substrates. (b) The dielectric parameters ϵ_1 and ϵ_2 of MgO from reflectance data. (c) Lattice structure of MgO. (d) Lattice parameters of commercially available perovskite oxide substrate.

3.1.1 MgO substrate for experiment

The property of MgO substrate (from MTI Korea) for experiment is outlined in Figure 3.2. The transmittance of two side polished-MgO substrate with 5 mm×5 mm×0.5 mm (width×length×thickness) shows a decrease above 6 eV, smaller than the values from published report for MgO single crystal [80]. When comparing transmittance of 10 nm thick-MgO films grown on r-Al_2O_3 substrate, the substrate can have impurities. The structure of MgO substrate was measured by scanning transmission electron microscope (STEM) in Figure 3.2 (b), showing disordered atomic arrangement in the black spots, while element analysis by energy-dispersive X-ray spectroscopy revealed no any other impurity. This defects also are presented in other papers [82] using MgO substrate. The decrease of transmittance over high photon energy will be related to a structural disorder as shown in TEM images.

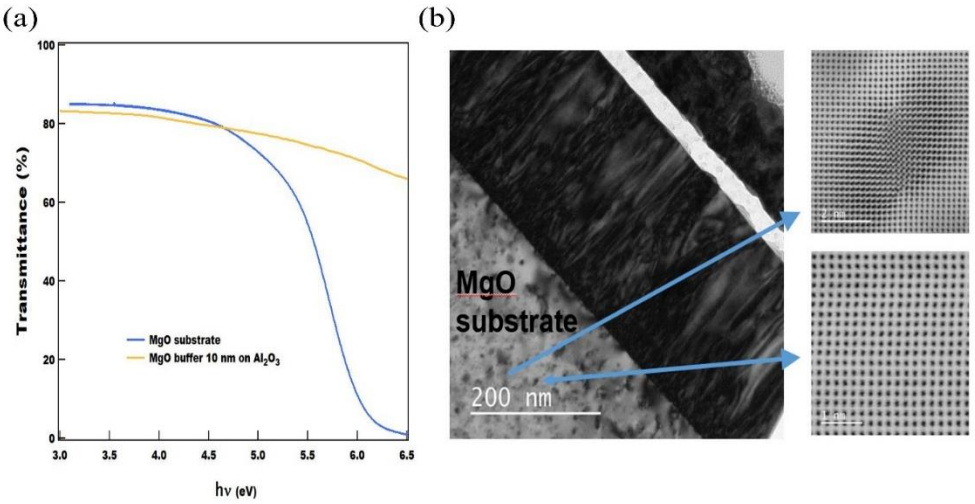

Figure 3.2: (a) Transmission spectra for MgO substrate and MgO films on r-Al_2O_3 substrate. (b) Cross-sectional TEM image for MgO substrate

3.1.2 Benefit at annealing experiment in high temperature

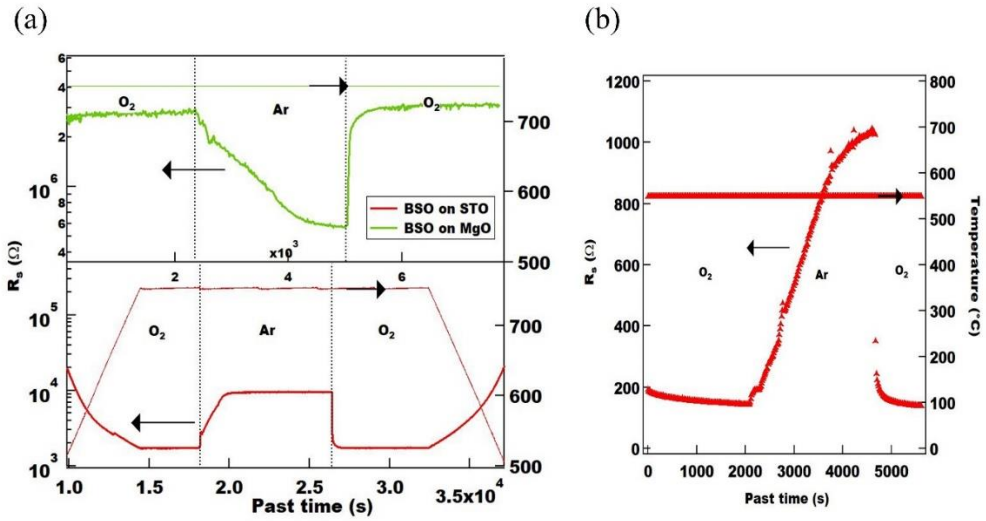

Figure 3.3: Annealing experiment. (a) Sheet resistance change for BSO film on MgO and $SrTiO_3$ substrate under O_2-Ar-O_2 atmosphere. (b) Sheet resistance change for $SrTiO_3$ substrate.

Figure 3.3 (a) describes annealing experiment for 100 nm thick-BSO film on $SrTiO_3$ and MgO substrate under O_2-Ar-O_2 atmosphere in the high temperature. The left axis

is for sheet resistance and right axis is for temperature of atmosphere. The sheet resistance was measured by 4 probe measurement with square van der Pauw geometry, accompanied with 4 % La-doped BSO metal electrode. Since samples of large resistance follows Ohm's law at small current range with somewhat accumulated potential, resistance is linearly extrapolated from current-voltage characteristics (slope) at current range of ~μA. The major two difference between two samples is the range of resistance and changed tendency in the gas flow. When comparing the resistance at 750 °C, BSO on MgO substrate is higher more than 3 order. And BSO on MgO substrate acts like electron carriers be created under O_2-poor environment, but BSO on $SrTiO_3$ substrate acts like hole carriers be created under O_2-poor environment. This assertion about a different majority carrier action is based on a guess of small change of μ in the gas flow. The very peculiar result on BSO annealing experiment is solved after annealing experiment of $SrTiO_3$ substrate alone in Figure 3.3 (b). The change of resistance in the change of gas flow is like BSO on $SrTiO_3$ substrate. The instability of oxygen in $SrTiO_3$ is well known and similar resistance change under gas flow is investigated in other papers [83]. So, the resistance from BSO film on $SrTiO_3$ substrate might be attributed by $SrTiO_3$ itself and its hole like majority carriers be due to strong scattering of electrons under high density of oxygen vacancies. Because BSO is an attractive materials for high temperature applications, MgO substrate with oxygen stability is suitable, not screening the transport of BSO. From above annealing experiment, the activation energy for oxygen vacancy of BSO can be found out;

$$\frac{R_{S,750\ C}}{R_{S,R.T}} \sim \frac{n_{750\ C}}{n_{R.T}} \sim \frac{e^{-E_A/kT(750\ C)}}{e^{-E_A/kT(R.T)}}$$

(3.1)

E_A, k, T are activation energy, Boltzmann constant, and absolute temperature, respectively. The activation energy is 0.42 eV.

3.2 Structure property of BSO on MgO substrate

The structures of grown films have a great effect on transport of carriers. The epitaxy of films can be found out by X-ray diffraction (XRD), observing the scattered intensity as a function of incident and scattered angle. It is a popular crystallographic spectroscopy to know a phase and an orientation of crystal, nondestructively. The detailed atomic arrangement can be found out by transmission electron microscopy (TEM), in which an electron beam is transmitted through a thin specimen to form an image. Carriers in thin films flow laterally, in most case, cross-sectional TEM image is analyzed in this dissertation.

3.2.1 X-ray diffraction analysis

X-ray diffraction patterns are obtained using a PANalytical X'Pert PRO diffractometer with a Cu K_α x-ray source of 1.5406 Å wavelength. According to $\theta - 2\theta$ scans in Figure 3.4 (a), epitaxial thin film of 100 nm thick- BSO grown on [001] MgO substrate exhibits well-defined (00l) diffraction peak. In oxide research area, the term epitaxy is boadly used for well-defined orientation of a single phase structure, which is different from conventional semiconductor, meaning a perfect atomic registry across interface.

Figure 3.4 (b) shows the reciprocal space map (RSM) around (103) peaks of 200 nm thick-BSO film and (204) peaks of MgO substrate. An RSM is a series of rocking curves taken over a range of 2 θ values so it represents the shape of a given Bragg reflection in a two-dimensional reciprocal space. The wave vectors q_x and q_z represent directions parallel and perpendicular to the substrate surface. As confirmed in the inset showing the enlarged RSM of (103) reflections, all intensity is well confined and there is no any polycrystalline growth. The larger mosaicity of BSO compared to that of MgO substrate is clearly visible. The mosaicity is a measure of the misorientation between individual grains and given by the circumferential spread in

RSM [84,85]. The full width at half maximum (FWHM) of (103) plane is 0.37°Due to the different crystal structures of the film and the substrate, the film have less epitaxial strain and higher defect concentration compared to the films on perovskite oxide substrate, resulting in larger spread. It is noteworthy that the spread in RSM of a BSO film on a $SrTiO_3$ substrate is slightly lower [1], although the lattice mismatch is larger with the $SrTiO_3$ substrates. In addition, the in-plane lattice constant of 4.126 Å and the out-of-plane lattice constant of 4.118 Å of the film indicate that the film is tensilely strained on MgO substrate (4.2 Å) [81]. The lattice parameter of single crystal BSO is 4.116 Å [1]. In contrast, the BSO film on $SrTiO_3$ substrates are compressively strained due to the smaller lattice constant of the $SrTiO_3$ substrate. [1]

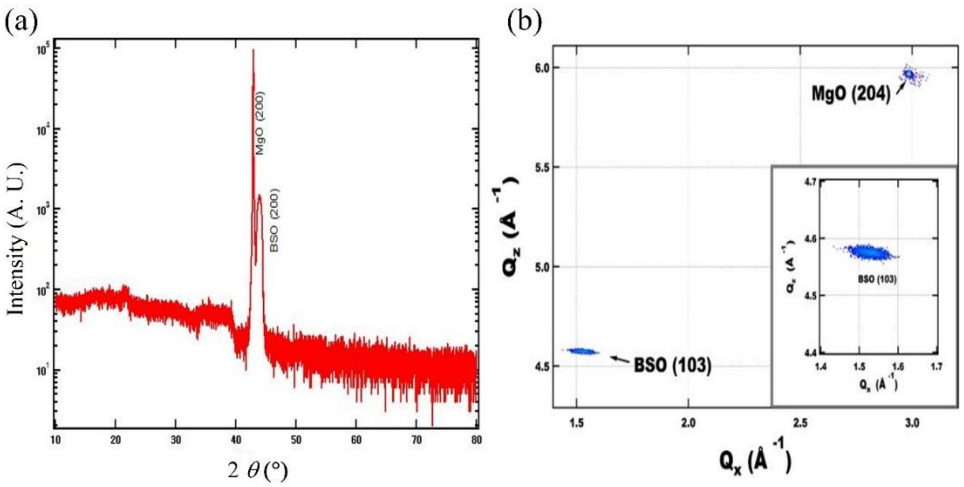

Figure 3.4: XRD result of BSO grown on [001] MgO substrate. (a) $\theta - 2\theta$ scans. (b) RSM around (103) Bragg reflection of BSO and (204) of MgO substrate.

3.2.2 Transmission electron microscopy

TEM images are obtained using JEM-ARM200F Cs corrected-TEM. The microstructural property of thin film of BLSO 50 nm/BSO 150 nm on MgO substrate by cross-sectional TEM is described in Figure 3.5. The high resolution TEM image at interface between film and substrate reveals a high density of misfit dislocations in

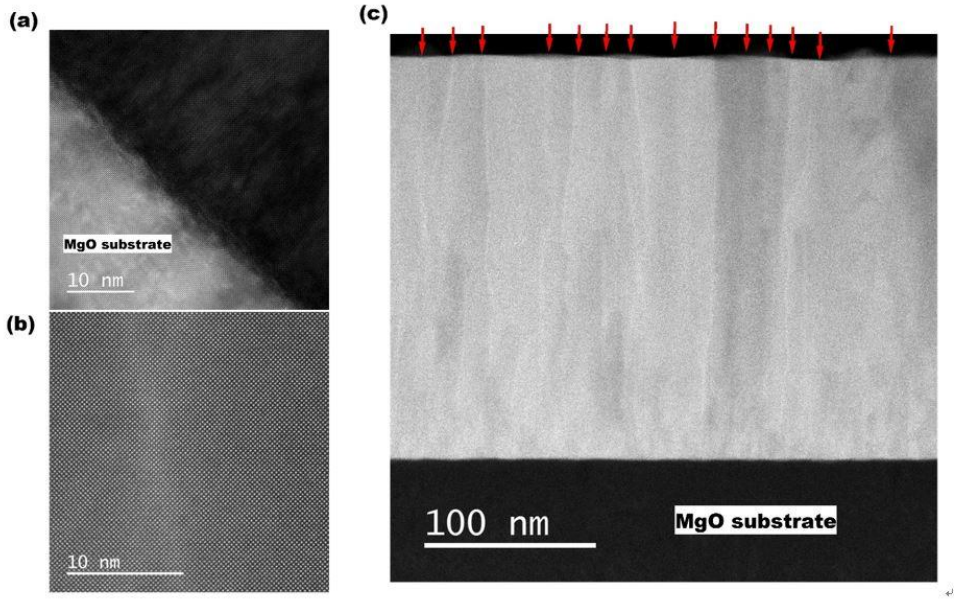

Figure 3.5: Cross-sectional TEM images of BSO films grown on MgO substrate. (a) High resolution TEM image at the interface between BSO film and MgO substrate. (b) HAADF-STEM image away from interface. (c) Low magnification HAADF-STEM image showing TDs.

Figure 3.5 (a), and the TDs throught the films, as indicated by red arrows in Figure 3.5 (c). Apart from these interface misfit dislocations and TDs, good crystalline BSO growth is confirmed in Figure 3.5 (b), which is a high-angle annular dark field scanning transmission electron microscope (HAADF-STEM) image. From the image the density of TDs is $\sim 2.0 \times 10^{11}\ cm^{-2}$, slightly higher than what observed previously with a different TEM technique [86]. The estimation of TD density from one-dimensional image is possible because the prepared TEM specimen has been thinned down to a few tens of nm scale, lower than the spacing between adjacent TDs. There are 14 red arrows in the lateral length of 300 nm. So TD density follows;

$$\left(\frac{14}{300\ nm}\right)^2 \cong 2.0 \times 10^{11}\ cm^{-2} \quad (3.2)$$

3.3 Transport property of BLSO film on MgO substrate

To improve transport property of BLSO films on MgO substrate, buffer layer technique using undoped BSO is investigated at first. Then as fixing a buffer layer, transport property dependent on La doping is presented. BLSO films grown on $SrTiO_3$ substrate are also compared. Lastly, trapped electrons at TDs and possible further improvement is introduced. We measured resistivity and Hall effect using the van der Pauw method with square geometry and the roughness using Cypher Atomic Force Microscope.

3.3.1 Buffer effect

Figure 3.6 shows the resistivity (ρ), μ, and n of 0.5 % La-doped BSO (50 nm) and 0.37 % La-doped BSO (50 nm) on MgO substrate while varying the BSO buffer layer thickness. Former case with more La doping shows nearly unchanged transport in the range of 100~300 nm thick-BSO. However, in the latter case, the ρ abruptly decreases with the 100 nm thick-buffer layer and thicker buffer layer than 150 nm are not more helpful in improving the transport properties of the BLSO films. The difference between Figure 3.6 (a) and (b) is attributed by high density of charge traps on BLSO films, so the latter case with smaller n is sensitive to buffer effect.

On the other hand, the surface of film is very important because transport in device such as FET is seriously affected on that. According to atomic force microscope image, the surface roughness (R_{RMS}) increases monotonically with the increasing buffer layer thicknesses and there is a jump at 150~200 nm thickness. As a result, 150 nm thick-buffer layer is the best for 50 nm thick-BLSO on top in terms of transport and top gated-FET application.

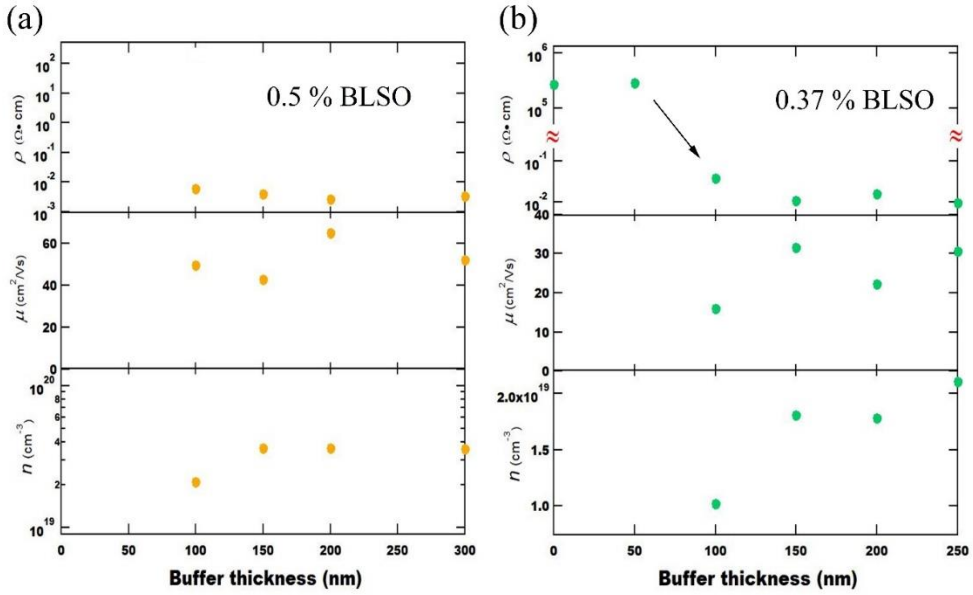

Figure 3.6: Undoped BSO buffer effect on BLSO films (a~b) ρ, μ, and n as varying buffer thickness.

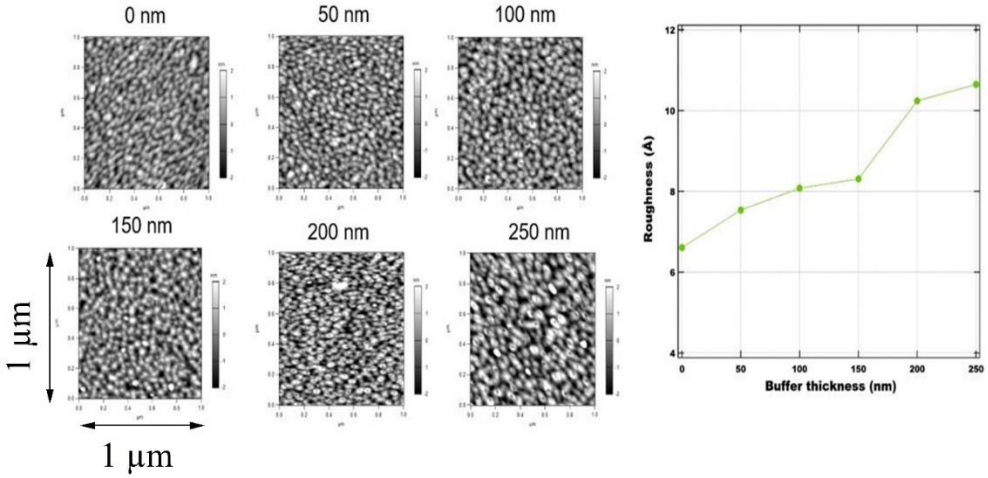

Figure 3.7: The image of surface morphology and R_{RMS} as varying buffer thickness.

3.3.2 La doping dependence

To see the overall trend of the transport properties (ρ, μ, and n), BLSO films with a fixed 150 nm thick-BSO buffer layer grown on MgO substrate are measured while varying La doping rate, shown in Figure 3.8 (a). The ρ continues to decrease and n increases with more La doping. The μ value, however, peaks at 2 % La doping, beyond which it starts to be limited by the ionized La dopant scattering. It is surprising that the μ of BLSO films on non-perovskite MgO substrate reaches at 97.2 $cm^2V^{-1}s^{-1}$ at 2.53×10^{20} cm^{-3} and 76.2 $cm^2V^{-1}s^{-1}$ at 4.94×10^{20} cm^{-3}. For example, the μ values of BLSO films deposited by PLD on BSO single crystal substrates by W.-J. Lee *et al*. [26], are ~80-100 $cm^2V^{-1}s^{-1}$ near 1.0×10^{20} $cm^{-3}$and ~75 $cm^2V^{-1}s^{-1}$ at ~5.0×10^{20} cm^{-3}. The transport properties of BLSO thin films with a 150 nm buffer layer on MgO substrate are comparable to those of homoepitaxial films on BSO single crystals both in the low doped regime where the TD scattering prevails and in the high doped regime where the ionized La impurity scattering is dominant. Transport properties of BLSO films with a 150 nm buffer layer on $SrTiO_3$ substrate are also included in Figure 3.8 (a), similar values compared to on MgO substrate. It seems that PLD technique is very important for high mobility BLSO films, so in this stage there is no remarkable degradation on transport using MgO substrate. However, our μ values are lower than the recent values 150 $cm^2V^{-1}s^{-1}$ at ~7×10^{19} cm^{-3} reported by an oxide MBE group [25] on $PrScO_3$ substrates, which suggests a possibility that out μ values are partly limited by cation off-stoichiometry.

When plotting μ as a function of n makes a bell-shaped curve, which implies TDs-limited μ in the lower doped regime [1]. The TDs diminish the μ by scattering and the dangling bonds along dislocation lines act as electron acceptors.

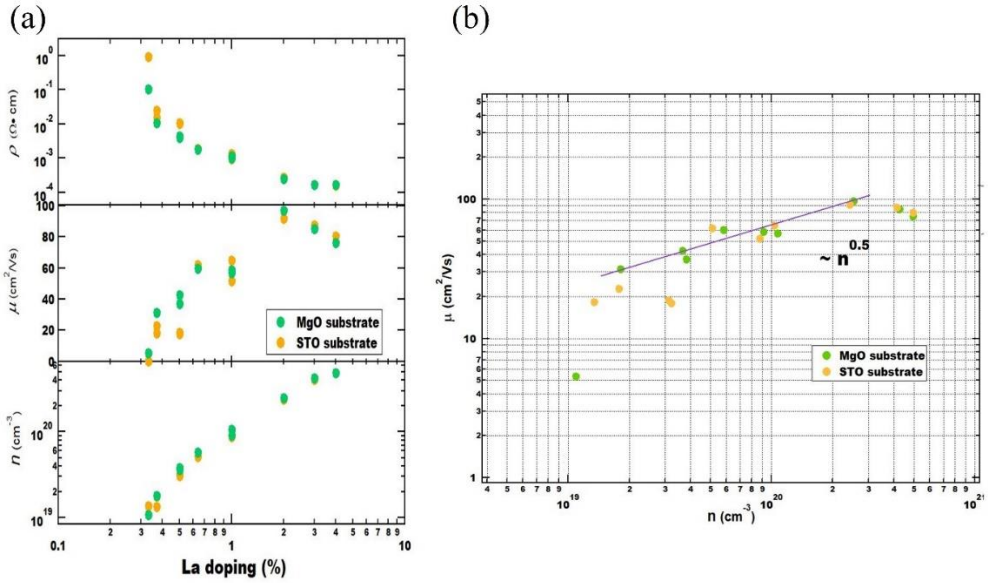

Figure 3.8: Transport property of BLSO films with 150 nm thick buffer layer on MgO and $SrTiO_3$ substrates as varying La doping rate. (a) ρ, μ, and n as a function of La doping rate. (b) μ vs. n

3.3.3 Trapped electrons in TDs and further strategy

When plotting n as a function of La doping rate, as in Figure 3.9 (a), the trapped electron density from the offset value in the graph is about 4.0×10^{19} cm^{-3} . These trapped electrons are likely to reside near or at the TD cores. A number of trapped charged per TD can be estimated;

$$\frac{4.0\times10^{19}cm^{-3}\times50\ nm/2.0\times10^{11}cm^{-2}}{50\ nm/4.116\ \text{Å}} \cong 8$$

(3.3)

to be 8e per unit cell thickness, not far from 6e which can be obtained from an assumption that the both cations, Ba^{2+} and Sn^{4+}, are missing in TDs. For comparison, the TD density on $SrTiO_3$ substrates are about 5×10^{10} cm^{-2} [68], smaller than what observed on MgO substrates. However, the μ and n on $SrTiO_3$ substrates in the low doped regime are not much different from those on MgO in Figure 3.8, suggesting

that the scattering strength by TDs may depends on the exact atomic structures near and at the TD cores. For example, the effect of the strain type (tensile or compressive) in the films on the TD core structures is not known.

Figure 3.9 (b) is a transport property for 0.33 % La-doped BSO as varying BSO buffer layer thickness with a structure of BLSO 50 nm/BSO/$BaHfO_3$ 62 nm grown on MgO substrate. According to Figure 3.6 (b), there is a seven order difference of ρ at 100~150 nm thickness. But in this case, the ρ changes gradually with BSO buffer thickness. The lattice constant of $BaHfO_3$ (4.171 Å [87]), larger than BSO (4.116 Å [1]) and smaller than MgO (4.2 Å [81]) may drive this result. As a result, appropriate choice of buffer and its thickness is very important to enhance μ of BLSO further. The study using another material as well as $BaHfO_3$, considering a stiffness of a solid material not only constrained lattice-matched buffer, is required.

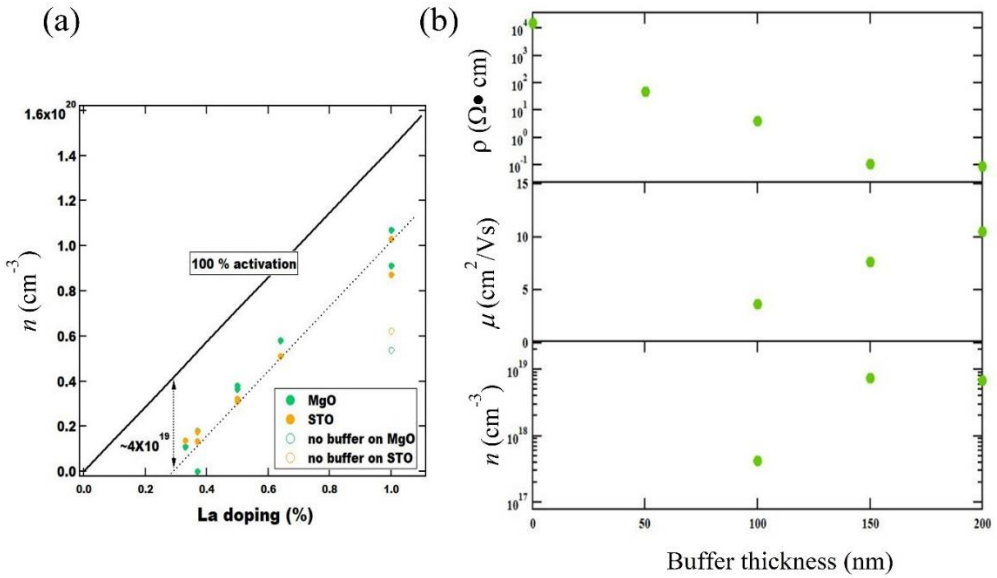

Figure 3.9: (a) *n* vs. La doping rate from Figure 3.8 (a). (b) ρ, μ, and *n* of BLSO as a function of BSO buffer thickness when $BaHfO_3$ is deposited on MgO susbstrate.

3.4 Field effect transistor based on BLSO channel on MgO substrate

Field effect device based on BLSO channel with HfO_2 gate dielectric layer is presented. 0.35 % La-doped BSO layer was chosen to observe effective band-bending by the field.

3.4.1 FET fabrication process

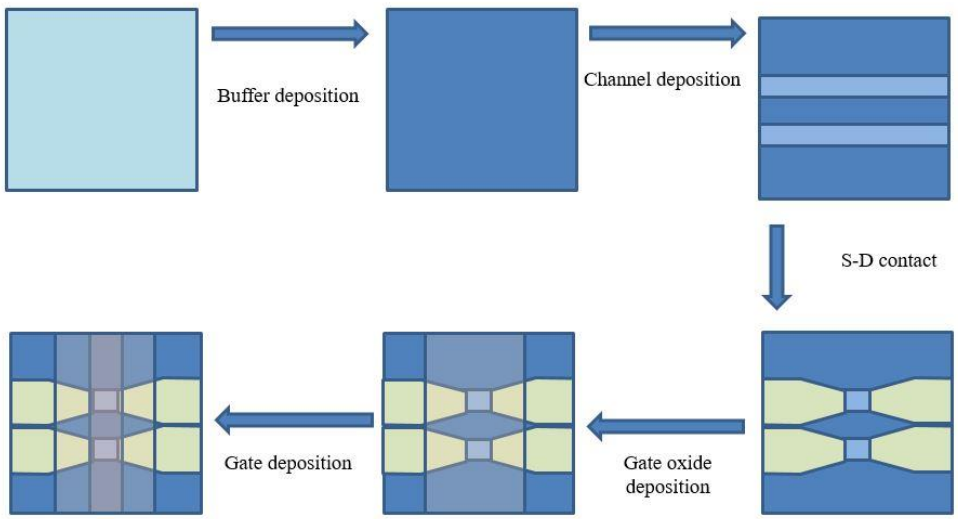

Figure 3.10: Fabrication process for FET based on BLSO with HfO_2 dielectrics.

As a first step, 180 nm-thick undoped BSO buffer layer is deposited on $5 \times 5 \times 0.5\ mm^3$ MgO (001) substrate. Next, two line-patterned 0.35 % La-doped BSO layers is deposited with a thickness of 12 nm using Si stencil mask. Then the length from the surface of BLSO to MgO substrate is ~192 nm, near the previous best result of buffer effect (50 nm (BLSO)+150 nm (buffer)= 200 nm). In the third step, the patterned In_2O_3:Sn electrode is deposited using a SUS mask at 10 mTorr of O_2 at 150 °C by PLD. Then, the HfO_2 gate dielectric layer is deposited by atomic layer deposition

(ALD). Because the conductance of BLSO channel layer increases after ALD process, probably due to hydrogen, the device is annealed in O_2 atmosphere at 750 °C for 4 hours. In the final step, In_2O_3:Sn electrode is deposited as the gate electrode using another Si line stencil mask to cover the entire channel area.

3.4.2 Theory for metal-insulator-semiconductor FET

The term MOS structure with metal-oxide-semiconductor interface is ambiguous when incorporating oxide semiconductors. Since the traditional MOSFET uses Si or GaAs as semiconductors and oxide as a dielectrics, the term is frequently used. However, when focusing only its function, its structure consists of metal-insulator (dielectrics)-semiconductor interface. The term MOS will be referred as a representative for metal-insulator-semiconductor structure from now on, as usual.

A MOSFET is based on the modulation of charge concentration by a MOS capacitance between a body of semiconductor and a gate electrode. The modulated carrier flows between source and drain contact. So it can be viewed as a gate voltage controlled current source.[50]

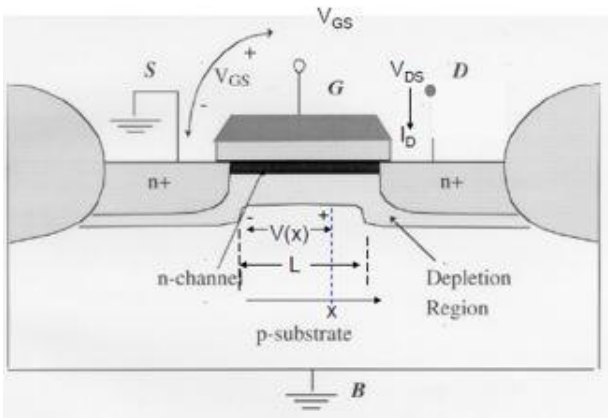

Figure 3.11: An example of FET.

At Figure 2.11, the accumulated carrier density (n_s), depending on lateral position (x)

from source to drain, can be written by capacitance formula,

$$\mathrm{q}n_s(x) = \ C_{ox}[V_{GS} - V_{th} - V(x)] \tag{3.4}$$

where, C_{ox}, V_{GS}, V_{th}, *V(x)* are capacitance per unit area, gate-source voltage, threshold voltage, voltage between source and position x, respectively. Threshold voltage is a voltage over which the free carriers start to accumulate at interface. And current between source and drain (I_{DS}) is driven based on a drift motion under Ohm's law,

$$I_{DS} = \ -\mathrm{v(x)}qn_s(x)W \tag{3.5}$$

where, v(x) and *W* are velocity of carriers at position x and width of device, respectively.

$$\mathrm{v(x)} = -\mu_{FE}\frac{dV}{dx} \tag{3.6}$$

v(x) is connected with field effect mobility (μ_{FE}) in (3.6) formula. And from (3.5) and (3.5), following differential equation is driven.

$$I_{DS}\ \mathrm{dx} = \ \mu_{FE}C_{ox}[V_{GS} - V_{th} - V(x)]dV \tag{3.7}$$

When integrating over length (*L*) between source and drain,

$$I_{DS} = \mu_{FE}C_{ox}\frac{W}{L}[(V_{GS} - V_{th})V_{DS} - \frac{{V_{DS}}^2}{2}] \tag{3.8}$$

is given. (3.8) only holds for $V_{GS} - V_{th} - V(x)$>0, that is, $V_{DS} < V_{GS} - V_{th}$ should be satisfied. This region is a non-saturated region.

When $V_{DS} > V_{GS} - V_{th}$, the region in which carrier does not exist but conduct current occurs. This region is called a saturation region and we says that pinch-off occurs. The saturation current ($I_{DS,sat}$) is given by integration of (3.7) right part from source to the boundary which carrier does not exist, that is, $\mathrm{V(x)} = V_{GS} - V_{th}$.

$$I_{DS,sat} = \frac{1}{2}\mu_{FE}C_{ox}\frac{W}{L}(V_{GS} - V_{th})^2 \tag{3.9}$$

μ_{FE} can be evaluated from (3.8) by differentiation at fixed V_{DS}, that is,

$$\mu_{FE} = \frac{\partial I_{DS}}{\partial V_{GS}}\Big|_{V_{DS}} \left(\frac{L}{C_{ox} W V_{DS}}\right) \tag{3.10}$$

The subthreshold swing (*S*), is an applied voltage to increase of I_{DS} by 10 times at cutoff region ($V_{GS} < V_{th}$). A device characterized by steep subtheshold slope exhibits a faster transition between low current (off) and high current states (on).

$$\mathrm{S} = \left(\frac{\partial log I_{DS}}{\partial V_{GS}}\right)^{-1} \tag{3.11}$$

3.4.3 FET based on BLSO channel on MgO substrate

The cross-sectional diagram and top view of the fabricated FET device are shown in Figure 3.12 (a~b). The channel length and width are 140 and 110 μm, respectively. Due to superior transparency of device on MgO substrate, the dotted lines is drawn to show boundary lines. Figure 3.12 (c) shows the output characteristics of device, which are I_{DS} vs. V_{DS} at various V_{GS}. Increase of I_{DS} with increase of V_{GS} indicates the device operates in an n-type accumulation mode. And pinch-off at high V_{DS} occurs as expected from a high performance FET. Figure 3.12 (d) represents transfer characteristics which are $I_{DS} - V_{GS}$, $I_{GS} - V_{GS}$, and $\mu_{FE} - V_{GS}$ curves in the linear region of $V_{DS} = 1$ V. The maximum μ_{FE} is 43.9 $cm^2V^{-1}s^{-1}$, I_{on}/I_{off} is about 3.0×10^7 and *S* is 0.21 V dec^{-1}. And μ_{FE} was found to decrease sharply after $V_{GS} = 4.4$ V, presumably due to the surface roughness. [88,89]

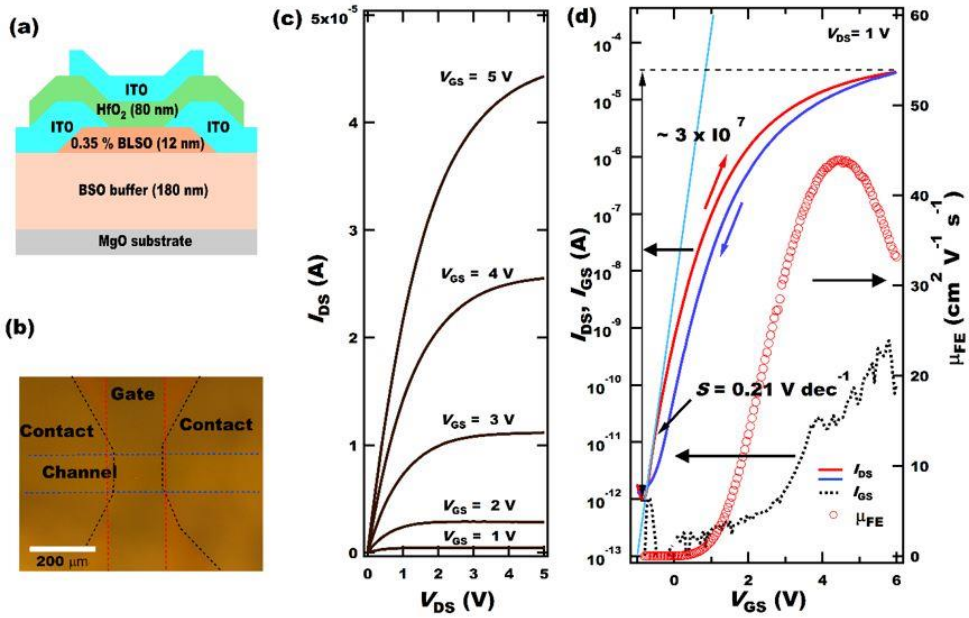

Figure 3.12: BLSO FET on MgO substrate with HfO_2 dielectrics (a) Cross-sectional diagram. (b) Top view taken by an optical microscope. (c) Output characteristics (d) Transfer characteristics

BLSO FET with HfO_2 dielectrics was previously reported using $SrTiO_3$ substrate [8]. Figure 3.13 compares BLSO FET on MgO substrate and on $SrTiO_3$ substrate. The maximum μ_{FE} is 24.9 $cm^2V^{-1}s^{-1}$, I_{on}/I_{off} is about 6.0×10^6 and S is 0.42 V dec^{-1}. The performance of device on MgO are slightly better than on $SrTiO_3$. When plotting μ_{FE} vs. n_s, the higher μ_{FE} on MgO, in spite of more La doping (0.35 %) than the FET on $SrTiO_3$ (0.25 %) is noteworthy. But the μ_{FE} sharply decrease than FET on $SrTiO_3$, probably due to large surface roughness than the latter case [88,89]. At Figure 3.7, R_{RMS} is ~8 Å, but is smaller than 4 Å for the latter case. Therefore, further efforts in reducing the surface roughness may increase the field effect mobility more.

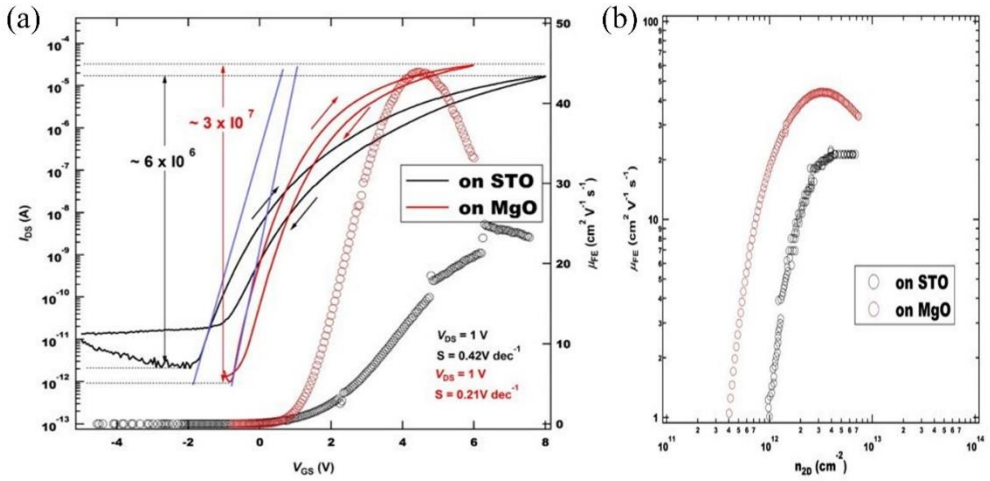

Figure 3.13: Comparison between BLSO FET on MgO substrate and on $SrTiO_3$ substrate. (a) Transfer characteristics (b) μ_{FE} vs. n_s.

Chapter 4

Bandgap engineering of $BaSnO_3$ by Hf substitution

Confined electron layer located at the interface of certain heterojunctions was predicted about sixty years ago by Anderson [93]. Esaki and Tsu [94], in 1969, proposed a heterostructure in which ionized impurities and free electrons could be spatially separated, described in Figure 4.1 (a), giving rise to a reduced Coulomb scattering. In 1978, Dingle *et al*. [95] observed μ enhancement in modulation-doped superlattices ($Al_xGa_{1-x}As$/GaAs), beyond the limit set by dopant scattering in bulk crystal. This was possible because MBE technology was sufficiently developed that such structures were grown. The μ has eventually increased by a remarkable factor of ~4000 from ~10^4 $cm^2V^{-1}s^{-1}$ in 1978 to ~3.6×10^6 $cm^2V^{-1}s^{-1}$ in 2007 over a 30 year period, shown in Figure 4.1 (b) [96] in GaAs-based modulation-doped two-dimensional electron gas (2DEG) system, presenting for a new generation of high-speed semiconductor device.

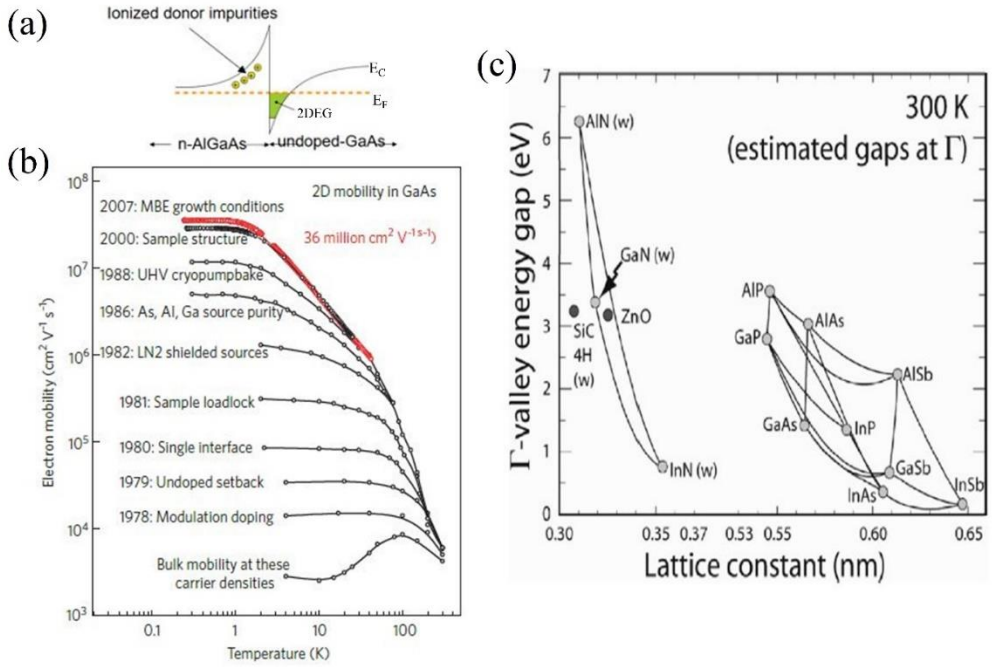

Figure 4.1: (a) An example of modulation doped heterostructure. (b) The m progress achieved for GaAs over the last three decades. (c) Energy gap vs. lattice constant for Ⅲ-Ⅴ compound semiconductors.

To realize high μ in modulation doping, selection of appropriate material to make heterointerface is very important. The first consideration is their band alignment, which makes a proper density of confined electrons on a desired site. The band offset between interface and ionized impurity density in large bandgap material affects primarily. The second consideration is an epitaxial growth; a single phase and a well-defined lattice orientation. The epitaxial growth supports an uniform and low atomic disorder at interface, while each material maintains its bulk property, e.g. bandgap, band structure.

The modulation doping in BSO system is not studied, yet, anywhere, and bandgap engineering will be a necessary step for it. Bandgap engineering is the process of controlling the band gap of a material by altering the composition of alloys. Because alloying may drive creations of second phases or microstructures, isovalent (the valence of the atoms being exchanged is the same) and isostructural (same structure)

materials are used to make a stable material. The study for bandgap engineering is extensively studied in Ⅲ-Ⅴ compound semiconductors such as GaAs and GaN, since optoelectronic properties as well as electronic properties has been got the limelight. Figure 4.1 (c) [97] shows two key parameters in bandgap engineering, that is, bandgap energy and lattice constant for Ⅲ-Ⅴ compound semiconductors, which are related to band alignment and epitaxial growth, respectively.

In this chapter, bandgap engineering controlled by Hf substitution for Sn site of BSO is investigated through modified band structure, crystal structure, and the bandgap using density functional theory (DFT) calculation, XRD, optical transmittance spectra. And La-doping in $BaSn_{1-x}HfO_3$ (BSHO) is studied to investigate the modulation doping possibility for BSO/BSHO heterostructures.

4.1 $BaSnO_3$ vs. $BaHfO_3$

Hf substitution on Sn-site on BSO can be a good candidate for the bandgap engineering of BSO. $BaHfO_3$ (BHO) has a larger optical gap than BSO (indirect bandgap: 2.95 eV [2]), where 4.8 eV [98] for indirect bandgap case and 5.8 ~6.1 eV [9,99] for direct bandgap case. Since bandgap of perovskite oxides are mostly driven by B-site cation and oxygen, substitution of Sn atoms in BSO can effectively change the band structure and bandgap. And recent reports about FET based on BLSO channel layer and the BHO gate oxide reached up to μ of 52.7 $cm^2V^{-1}s^{-1}$, demonstrating their excellent interface property. [9]

Actually, Hf substitution can really be a good candidate than any other perovskite oxide to enhance μ of BSO channel when considering Sn-O bonding angle. One possible reason is B-site substitution and the other one is larger lattice constant (4.171 Å [87]) with cubic structure than BSO (4.116 Å [1]).

Substitution of A-site cations with other atoms usually distorts the cubic crystal

structure of the perovskite oxide [100], so that the strain at the interface between the cubic BSO and non-cubic epitaxial layer might disturb the straight Sn-O-Sn bond of BSO. The previous research on the La-doped $SrSnO_3$ films found that only a few films are conductive [57,58] and reported the highest μ of 40 cm^2/Vs at 9 x 10^{19} cm^{-3} [101] with an increase of bandgap from 3.50 eV to 4.27 eV [102], implying the large effect of tilted and/or rotated SnO_6 octahedra on the electron transport.

Moreover, Hf substitutions will pose tensile and cubic strain on an adjacent BSO layer, when making heterostrucures, guessing from crystal structure of BHO. So cubic structure with straight Sn-O bonding angle of BSO will be maintained after creation of heterointerface.

4.2 Density functional theory calculation of $BaSn_{1-x}Hf_xO_3$

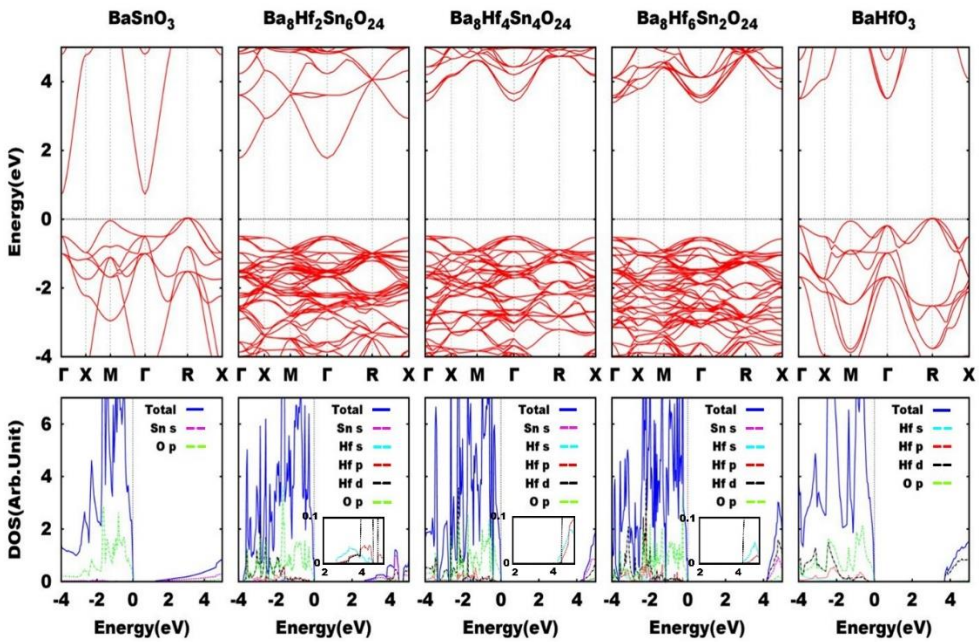

Figure 4.2: Band structure (top) and PDOS (bottom) of $BaSn_{1-x}Hf_xO_3$ (x=0, 0.25, 0.5, 0.75, 1) from DFT calculations. The inset is the enlarged PDOS plot for Hf orbitals only.

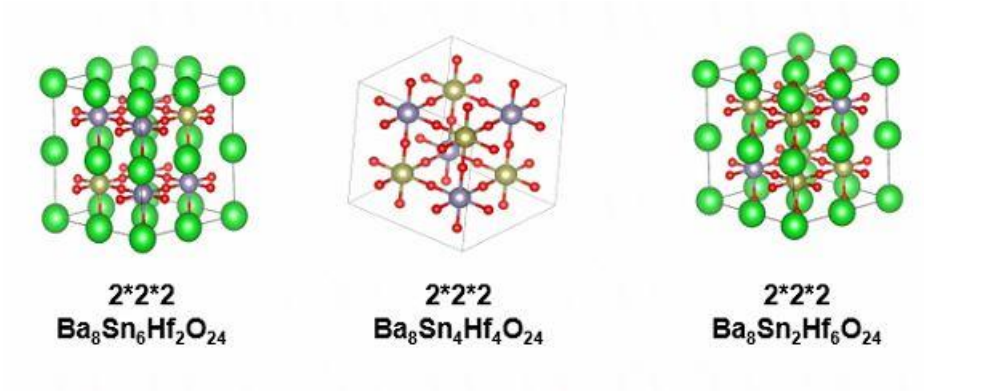

Figure 4.3: Atomic configuration of supercell of BSHO, which is in most stable state.

The band structure of $BaSn_{1-x}Hf_xO_3$ (x=0, 0.25, 0.5, 0.75, 1) was calculated in the scheme of the generalized gradient approximation with the revised Perdew-Burke-Ernzerhof functional for solids (GGA-PBEsol) in DFT as implemented in the Vienna *ab initio* simulation package code.[103] This most commonly used version in solid-sate calculations today was found to work well for perovskite oxides [104,105]. Especially, we chose the scheme because Hf atom is heavy and have complicated orbitals, not adequate by using local density approximation (LDA). Figure. 4.2 shows the band structure and the total density of states (TDOS) /partial density of states (PDOS) per atom as varying Hf content. The 2 x 2 x 2 supercell is used for $BaSn_{1-x}Hf_xO_3$ (x=0.25, 0.5, 0.75) and the TDOS is scaled down to 1/8 to show each orbital characteristics effectively. The stable atomic configuration of each supercell is show in Figure 4.3. The effective mass of conduction band is 0.2 m_0 for BSO and 0.62 m_0 for BHO, respectively, consistent with the previous calculations based on DFT [106,9]. Importantly, the substitution of Hf for Sn increases the band gap and do not create gap states, which is a crucial condition for bandgap engineering of BSO.

Meanwhile, while the O-2p orbital contribution continues to dominate near the valence band maximum (VBM), the feature of the conduction band minimum (CBM) abruptly changes. As the Hf content increases, the major contribution of the Sn-5s orbital decreases and the Hf-5d orbital becomes dominant in the CBM, decreasing the conduction band dispersion. The inset shows the enlarged PDOS plot only for Hf

orbitals to show the characteristics in the conduction band edge (CBE). As the Hf content increases, the major contribution to CBE changes from the Hf-6s to the Hf-5d orbital, while the s orbital remains as the major contribution to CBE in the case of Sn.

4.3 Structure property of $BaSn_{1-x}Hf_xO_3$ films

The crystal structure, such as latter parameter, of BSHO films is studied using XRD measurement. BSHO films of 100 nm was deposited by sequential laser ablation of BSO and BHO targets on [001] MgO substrate ($5 \times 5 \times 0.5\ mm^3$).

The θ-2θ scans in Figure 4.4 (a) confirms the epitaxial growth of all the films ($BaSn_{1-x}Hf_xO_3$; x=0, 0.2, 0.4, 0.6, 0.8, 1) on MgO substrate. And the (002) BSHO peaks move toward the (002) peak of MgO substrate with increasing Hf content due to the larger lattice constant of BHO. The full widths at half-maximum (FWHM) of the ω-scan, presented in the inset, for $BaSn_{1-x}Hf_xO_3$ (x=0.2, 0.4, 0.6) films were smaller than for BSO on MgO, which is probably a consequence of better lattice matching with increasing Hf content. Due to proximity of the (002) peak of BHO to the substrate peak, we could not measure the ω-rocking curve around the (002) peak of $BaSn_{1-x}Hf_xO_3$ (x=0.8, 1) films.

The in-plane lattice structure of BSO and BHO is invetigated by the reciprocal space mapping (RSM) in Figure 4.4 (b). Although the confined intensity in RSM indicates no polycrystalline growth, the larger spreads in the in-plane direction in both films may suggest the high density of misfit dislocations. The large lattice mismatch of BSO (4.116 Å [1]) compared to the MgO substrate (4.2 Å [81]) generates the larger mosaicity in the in-plane direction than BHO (4.171 Å [87]), involving the largest FWHM of 1.2° for the (002) peak of BSO in Figure 4.4 (a). On MgO substrates, the structural quality improves as the Hf contents increases.

Figure 4.4 (c) describes the out-of-plane lattice constant of BSHO calculated from the θ-2θ scans in Figure 4.4 (a) and GGA-PBEsol with varying Hf contents.

Conventionally, the lattice constant of alloy ($A_{1-x}B_x$) follows a linear equation conformable by the Vegard's law [107], that is,

$$a(\mathrm{x}) = (1 - \mathrm{x})a_A + xa_B \tag{4.1}$$

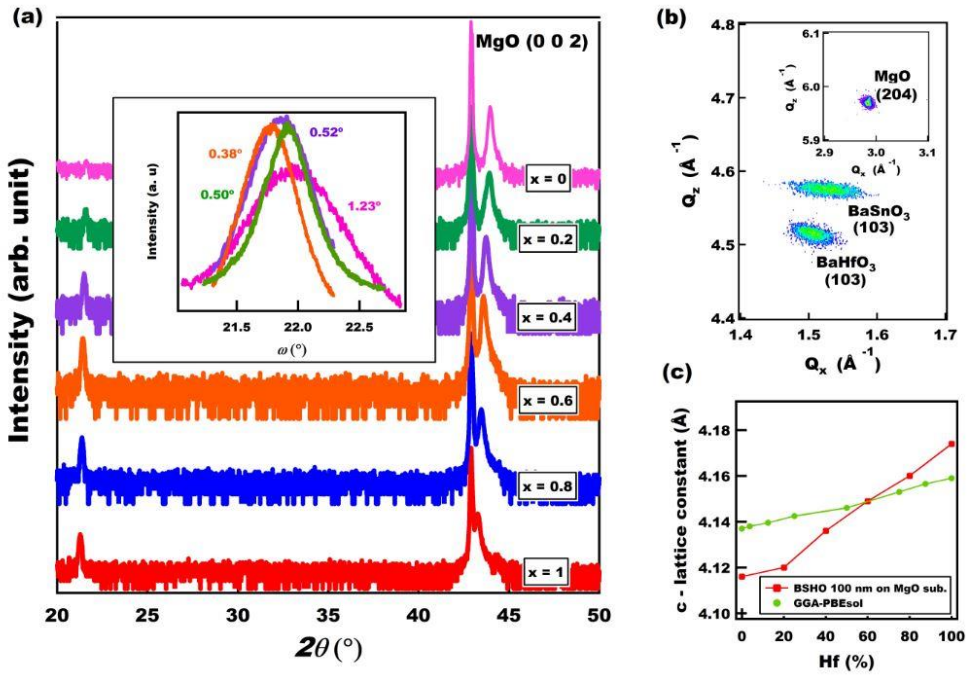

Figure 4.4: XRD result of BSHO films grown on MgO substrate. (a) θ-2θ scans and its rocking curves around (002) peaks. (b) RSM around (103) reflection of each BSO and BHO films. (c) Lattice constant from θ-2θ scans and calculation based on GGA-PBEsol as varying Hf content.

since the lattice parameter is determined by an ensemble average over a significant volume of the material. The lattice constants increase with more Hf content but the small deviation from the perfect linear line in the experimental result arises from the different degree of tensile strain (BSO: 4.126 Å, BHO: 4.168 Å in the in-plane direction) on MgO substrate, as exhibited in Figure 4.4 (b).

Lattice parameter from GGA-PBEsol calculation follows perfectly the Vegard's law. But there is a discrepancy of BSO (4.116 Å) and BHO (4.171 Å) compared to single crystal data. The calculated result in this case, BSO is 4.137 Å and BHO is 4.159 Å. Y. Zhang *et al*. [108], reported that lattice of BSO is larger for GGA-PBEsol (4.139

Å) than LDA (4.100 Å). In case of BHO, LDA predicts more inconsistent result of 4.2499 Å by A. Bouhemadou *et al*. [109]

4.4 Optical property of $BaSn_{1-x}Hf_xO_3$ films

The optical property, such as a bandgap energy of BSHO films is studied using optical transmission spectra. The same samples, which were measured in chapter 4.3, were also investigated. And the tendency of bandgap with increasing Hf content, which is different from conventional semiconductor alloys, is discussed.

4.4.1 Bandgap energy of $BaSn_{1-x}Hf_xO_3$ films grown on MgO substrate

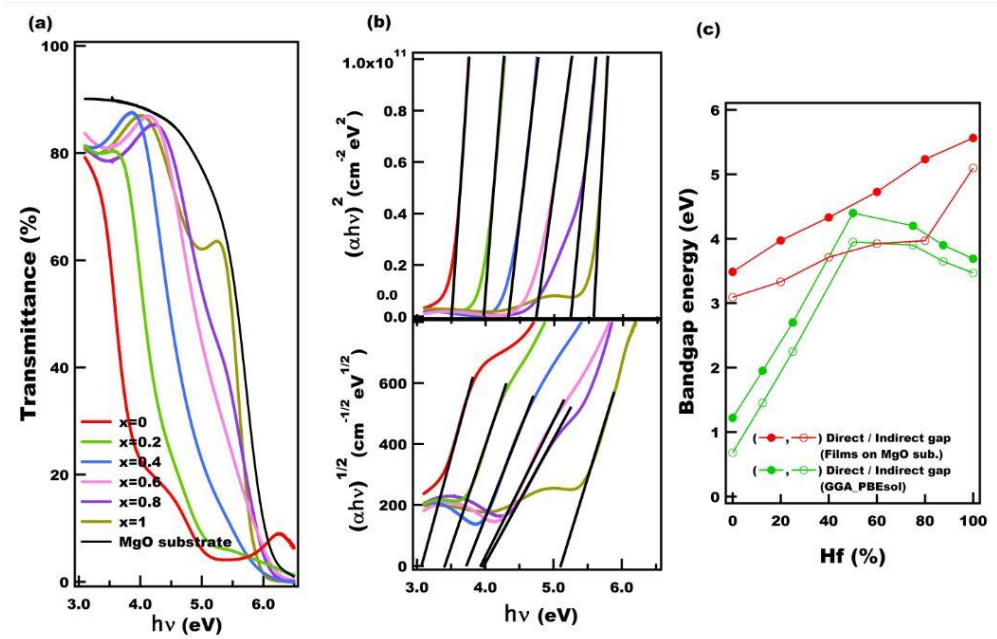

Figure 4.5: Optical properties of BSHO films grown on MgO substrate. (a) Optical transmittance. (b) $(\alpha h\nu)^2$ vs. hν plot and $(\alpha h\nu)^{1/2}$ vs. hν plot. (c) Direct and indirect bandgap as varying the Hf content from the optical transmission spectra and the calculations based on GGA-PBEsol.

The optical transmittance measurement of $BaSn_{1-x}Hf_xO_3$ films (x=0, 0.2, 0.4, 0.6, 0.8, 1) on MgO substrate is shown in Figure 4.5 (a), in the range of 3~6.5 eV, which is smaller than the optical bandgap of MgO substrate (7.8 eV [80]). All the films exhibit a high transparency of ~ 80 % in the edge of the visible region and increasing Hf content does not reduce the transmittance until ~ 4.5 eV. The oscillation of spectra is due to the interference effect of film of 100 nm thickness. The optical absorption coefficient (α) is extracted.

The optical bandgap can be estimated from Tauc plots [110],

$$(\alpha h\nu)^n = \mathrm{A}(h\nu - E_g) \tag{4.2}$$

where h, ν, A, and E_g are Planck's constant, frequency, a constant, and the band gap, respectively, and n is a constant that indicates the nature of transition, which is 1/2 for indirect and 2 for direct. The extrapolated linear portion is described in Figure 4.5 (b) for the direct (top) and indirect (bottom) allowed bandgaps.

As a result, in Figure 4.5 (c) the bandgap increases with the Hf content from 3.09 eV to 5.10 eV for the indirect gap and from 3.49 eV to 5.56 eV for the direct gap. All the solid solutions are indirect bandgap insulators. Most importantly, Hf substitution increase the bandgap of BSO. On the other hand, significant discrepancies exist between bandgaps of BSHO extracted from the optical transmittance spectra and the calculations based on GGA-PBEsol. The optical bandgap increases linearly (direct gap) or with a downward bowing (indirect gap). But calculated bandgap changes with an upward bowing (both) and even have the largest value at $BaSn_{0.5}Hf_{0.5}O_3$. And the smaller bandgaps of BSO and BHO in the calculated results than the measurements can be attributed to underestimation of bandgap which often occurs in PBEsol [111]. When considering hybrid functional that incorporate a portion of exact exchange from Hartree-Fock theory, e.g, Heyd-Scuseria-Ernzerhof (HSE) exchange-correlation functional, the indirect bandgap of BSO is 2.905 eV and BHO is 5.274 eV. But the overall tendency is not changed.

4.4.2 Bandgap bowing

Typically, the bandgap (E_g) of alloy (A_xB_{1-x}) is characterized by the bowing parameter (b) [112];

$$E_g^{AB}(\mathrm{x}) = \mathrm{x}E_g^A + (1-\mathrm{x})E_g^B - \mathrm{bx}(1-\mathrm{x}) \tag{4.3}$$

Conventional semiconductors, which has p-like VBM and s-like CBM has a positive bowing parameter (downward bowing) because very different characters between VBM and CBM makes the intraband coupling stronger than the interband coupling. [113] In the case of perovskite oxide semiconductor, the change of bandgap on the composition has not been studied in depth. [114]

Unusual value of b is observed such as, when large atomic size difference and large chemical mismatch arises like $Zn_{1-x}Be_xO$, $Mg_{1-x}Be_xO$ [115], direct-indirect transition occurs like $Al_{1-x}Ga_xAs$ [97], strong localization is involved like $Ni_xCd_{1-x}O$ [116], and strain is induced like ZnO nanowires [117]. The latter case is observed in GaAs film [118], too.

The upward bowing in calculated result in BSHO may relate to the smaller contribution of Hf-s orbital at the CBE as increasing Hf content, described in the inset of Figure 4.2. Figure 4.6, illustrating the optical properties of $BaSn_{1-x}Hf_xO_3$ (x:0, 0.25, 0.5, 0.75, 1) films deposited on r-plane Al_2O_3 substrate with 5 nm MgO buffer layer, supports that the strain also affects the bandgap of BSHO films so that upward bowing occurs for the direct gap. Because the optical gap is sensitive to strain, the appropriate doping control of Hf is required for desired bandgap.

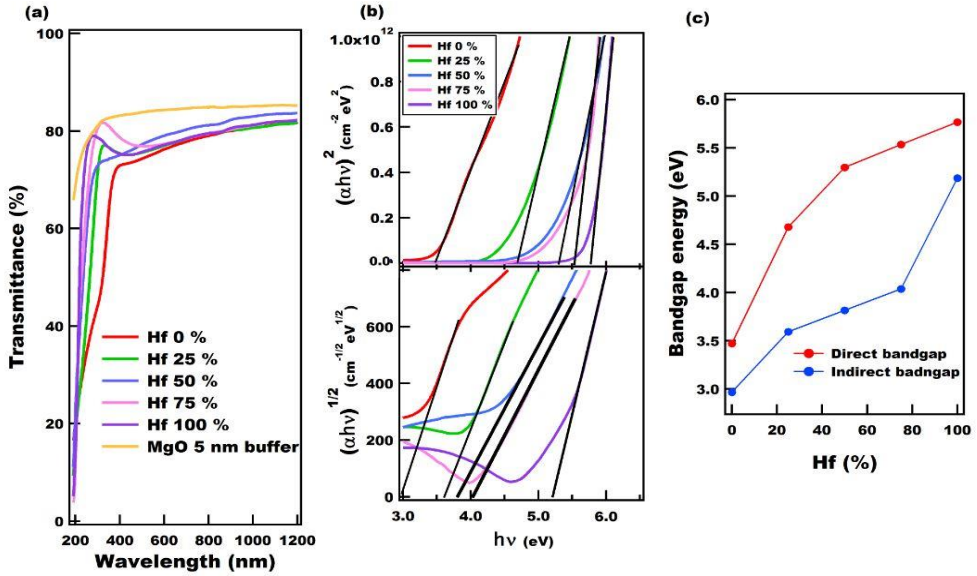

Figure 4.6: Optical properties of BSHO films grown on r-Al_2O_3 substrate. (a) Optical transmittance. (b) $(\alpha h\nu)^2$ vs. hν plot and $(\alpha h\nu)^{1/2}$ vs. hν plot. (c) Direct and indirect bandgap as varying the Hf content from the optical transmission spectra.

4.5 Transport property of n-type (Ba,La)(Sn,Hf)O_3 films

The large bandgap material in modulation-doped heterostructure, donates free electrons. Electron doping on insulating BSHO films can be done by La doping on Ba site like BLSO. 50 nm thick La-doped BSHO films (BLSHO) were grown on MgO substrate with 60 nm BHO buffer layer. The control of La and Hf doping rate is done using sequential deposition of 2 or 3 targets from $Ba_{0.99}L_{0.01}SnO_3$, $Ba_{0.96}L_{0.04}SnO_3$, $Ba_{0.96}L_{0.07}SnO_3$, and BHO, while maintaining less than 1 unit cell thickness per each cycle. The transport property is measured by Hall effect using square van der Pauw geometry.

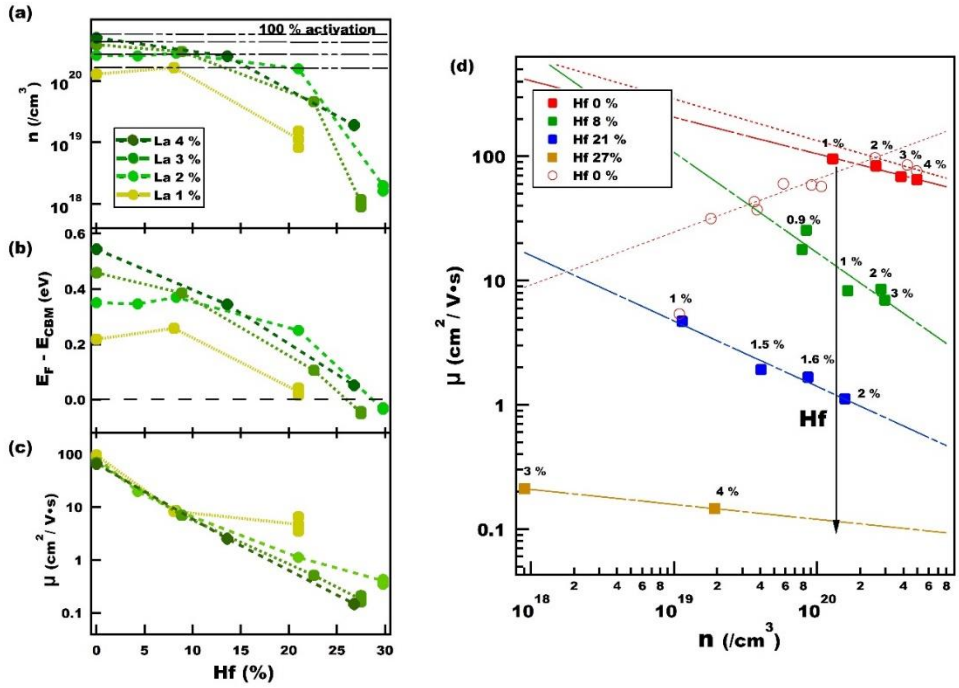

Figure 4.7: Transport property of BLSHO films grown on MgO substrate with BHO buffer layer. (a) *n* as varying Hf content in each La doping rate. (b) E_F-E_{CBM} as varying Hf content. (c) μ as varying Hf content. (d) μ as a function of *n* for each Hf content.

Figure. 4.7 (a) shows the *n* as varying the Hf content for each La doping rate. Each horizontal dotted line indicates a 100 % activated *n* and it is noteworthy that in BLSO films dopants are almost fully activated. While increasing the Hf content, the *n* continually decreases, as the Fermi level moves closer to the CBM. The Fermi levels (E_F) apart from the CBM in Figure 4.7 (b) are estimated by computing the Fermi-Dirac integral from the measured *n* with the effective mass of 0.42 m_0 [18]. We found that BLSHO remains degenerate up to ~ 30 % of Hf content, suggesting the La dopants act as an effective donor despite the increased bandgap. Although above 30 % Hf content free carriers rarely does not exist, there is a possibility that the carriers, hidden below the measurement limit by acceptor levels as in the case of BLSO in low doped regime, can be driven by electric field or manipulation of band bending. On the other hand, the GGA-PBEsol result in Figure 4.8 predicts 3.7 % La-doped

$BaSn_{0.6}Hf_{0.4}O_3$ to be degenerate with n = 2.2 x $10^{20}/cm^3$, which is in contrast to experimental results of the large resistivity of the film. More careful study for the origin of smaller La activation rate in BLSHO films, i.e, the formation energy of the cation vacancy and the La anti-site defects as well as TDs, will help to increase free carriers in BLSHO films.

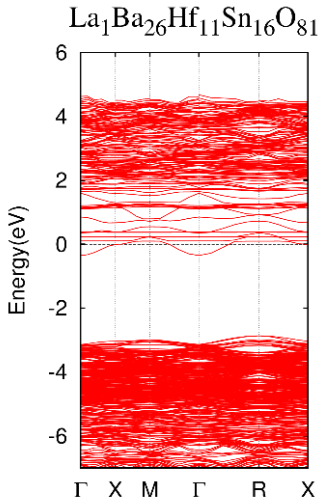

Figure 4.8: Band structure of BLSHO (3×3×3) supercell by GGA-PBEsol.

The μ vs. Hf content is plotted in Figure 4.7 (c), where μ sharply decreases as the Hf content increases for each La doping rate. This reduced μ is not surprising because most of compositional alloys exhibit mobility generally lower than the linear interpolation due to alloy scattering [97,119], in which the fluctuations in local chemistry leads to fluctuations in electronic states. Although there is a small change of the effective mass from 0.2 m_0 (Hf=0 %) to 0.62 m_0 (Hf=100 %), the μ determined by both the band structure and the scattering rate sharply decreases with Hf substitution. However, this phenomena does not affect on the role of BLSHO for the doping layer since the transport will occur in the lower bandgap BSO layer. Sb^{5+} doping on Sn-site on BSO also supports the large scattering on the Sn-site substitution due to the nature of SnO_6 conduction channel. [18]

Figure 4.7 (d) is a log-scale plot of μ as a function of the *n* for the Hf content of 0, 8, 21, 27 %. The strong scattering by Hf is remarkable, indicated by the vertical arrow line, showing the change of the highest μ of 95.3 cm^2/Vs at $1.28 \times 10^{20}/cm^3$ in BLSO to the lowest μ of 0.2 cm^2/Vs at 2×10^{19} $/cm^3$ in BLSHO with 27 % of Hf substitution.

The negative slope in graph, ranging from γ values of $-0.12 \sim -0.8$ in the relation of $\mu \propto n^{\gamma}$, as indicated by the dotted lines, is different from the La-doped BSO and the Sb-doped BSO films in the similar *n* regime [1,18]. Usually, the high density of dislocations makes a bell-shaped curve [1], which results from the ineffective screening of charge traps in low doping regime coupled with strong dopant impurity scattering in high doping regime, as represented by blank red circle plots of BLSO films with BSO buffer on MgO substrate [120]. In BLSHO the ionized impurity scattering seems stronger than in BLSO in the region of 10^{18}~10^{21} cm^{-3}, which probably shifted the dome in the bell-shaped curve toward the lower *n* regime.

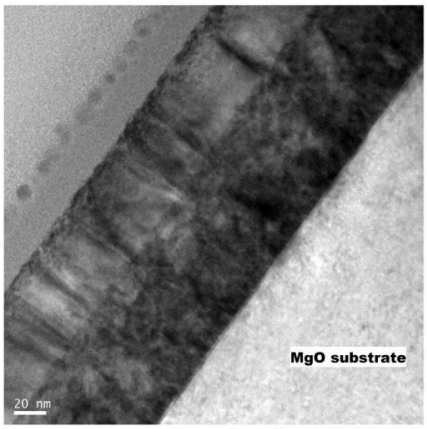

Figure 4.9: Cross-sectional TEM image of BSO 50 nm/BHO 60 nm grown on MgO substrate

It is worth noting that, despite the large amount of Hf substitution in Sn-O-Sn conduction channel, low μ and *n* values can be measured in the Hall measurement, which is difficult in the case of BLSO film due to large resistivity below $n \sim 1 \times 10^{19}/cm^3$. Figure 4.9 is a cross-sectional TEM image of BSO 50nm/BHO 60 nm grown

on MgO substrate, still confirming TDs in upper BSO films. Although the change of structure is not sure from TEM image, measurable *n* in the range of 10^{18}~10^{19} cm^{-3} may imply that appropriate lattice-matched grading by BSHO on MgO substrate may enhance electron transport in low doping regime of BLSO.

4.6 Possibility for enhancement of mobility by $(Ba,La)(Sn,Hf)O_3/BaSnO_3$ interface

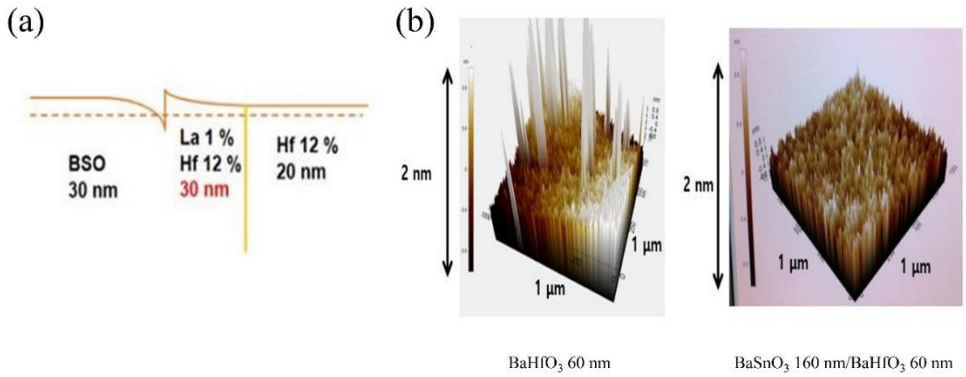

Figure 4.10: (a) Band bending diagram estimated for a trial for BSO/BLSHO interface. (b) Surface morphology from AFM for BHO 60 nm and BSO 160 nm/BHO 60 nm film on MgO substrate.

As a first trial, we fabricated BSO/BLSHO interface like Figure 4.10. First, 60 nm thick-BHO is deposited on MgO substrate. And $BaSn_{0.88}Hf_{0.12}O_3$ and $Ba_{0.99}La_{0.01}Sn_{0.88}Hf_{0.12}O_3$ is deposited. Then we measured before and after 30 nm thick BSO deposition. The estimated conduction band offset from Figure 4.5 is ~0.18 eV. The transport property changes from 0.0366 Ω·cm, 1.51 $cm^2V^{-1}s^{-1}$, 1.13×10^{20} cm^{-3} to 0.0289 Ω·cm, 1.73 $cm^2V^{-1}s^{-1}$, 1.25×10^{20} cm^{-3}. Slight increase of μ is shown. Much efforts is required to enhance the surface quality due to large roughness of BHO film. Laser ablation of large bandgap material is difficult. Figure 4.10 (b) shows the

roughness is much better when covering BHO by BSO buffer. (0.764→ 0.398 nm)

Chapter 5

Modulation doping in $LaInO_3/BaSnO_3$ polar interface

Even if high-quality single crystals are made with small defects such as impurities and dislocations, dopants providing mobile electrons themselves severely limit the μ. However, a two-dimensional electron gas (2DEG) where mobile electrons are spatially separated from ionized dopant or other scattering sites, can solve this problem. Three different approaches such as field effect doping (Si), modulation doping (GaAs, AlAs, etc.), polarization doping (GaN) have been used with conventional semiconductors. This 2DEG science is important because electronic device operation is mainly based on it, besides, a new science can be generated using metallic state in the middle of non-metallic states.

To date, field effect doping has been realized in BSO system, but modulation doping has not been studied, yet. Recently, a paper about polarization doping in BSO system by $LaInO_3$ (LIO)/$BaSnO_3$ interface is reported [121]. Unlike polarization doping in GaN system [122], La doping is required to get enough density of electrons confined. Since La ionized dopant exists in 2DEG in LIO/BLSO interface, modulation doping on smaller bandgap BLSO layer with a structure of LIO/BSO/BLSO may enhance μ than LIO/BLSO interface. It is a first step whether modulation doping technique is working in LIO/BSO polar system.

This chapter starts from an introduction about various 2DEG, depicting each feature and limitations. And scattering theory for 2DEG follows, including Coulomb

scattering from charged impurities, phonon scattering, and interface roughness scattering. Then LIO/BSO polar interface is introduced with its main advantage of oxygen stability. Next, the Hall measurement result is discussed about modulation doping with LIO/BSO/BLSO structure. The inserted undoped BSO spacer layer did not show the effective enhancement of μ. The characteristic of LIO/BSO/BLSO structure is investigated and electron density profile is calculated by a self-consistent 1D Poisson-Schrodinger equation. Eventually, the enhancement of μ in LIO/BSO/BLSO is confirmed using FET and further effort is discussed. A peculiar transport property on LIO/BSO, related to LIO thickness, is described at last.

5.1 Various 2DEG

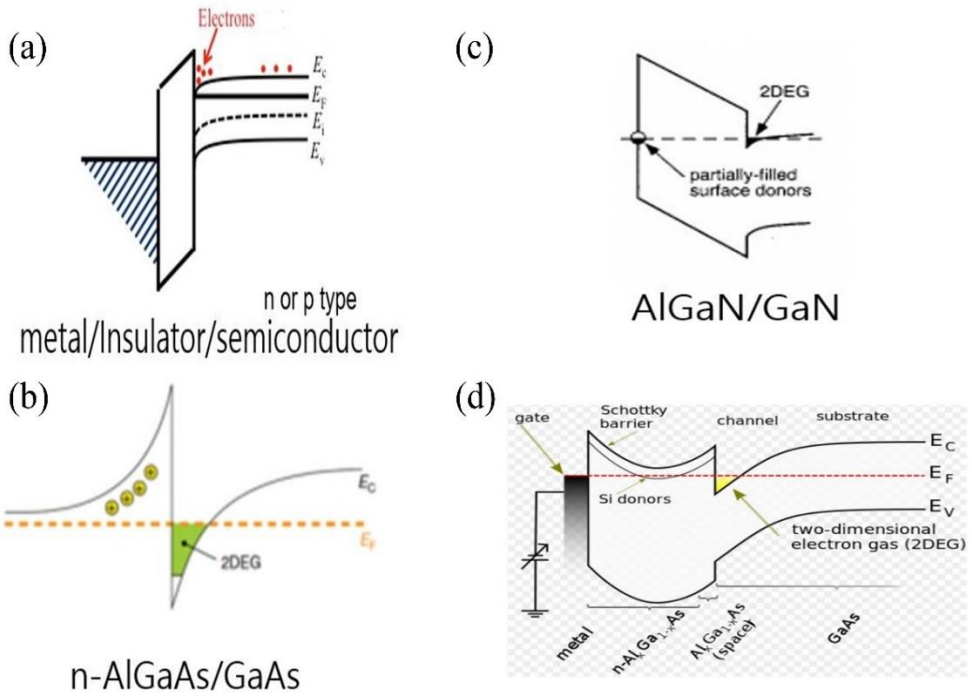

Figure 5.1: Examples about band bending diagram of various 2DEG. (a) MOS structure. (b) Modulation doped structure. (c) Polarization doped structure. (d) HEMT

In this section, three types of 2DEG is outlined, such as field effect doping (metal-insulator-semiconductor (MIS)), modulation doping ($Al_xGa_{1-x}As/GaAs$), and polarization doping ($Al_{1-x}Ga_xN/GaN$). Figure 5.1 (a~c) shows an example of band bending diagram for these three type of 2DEG.

Most of the work on 2DEG with MIS systems has been done on a technologically well-developed example, the metal-SiO_2-Si structure [123-127]. The Si MOSFET was developed in the 1960s and 1970s as an amplifying and switching device and is now one of the major electronic components of memory and logic circuits [125-127]. It works that the charge on the metal plates of a MOS capacitor is changed by application of a voltage in order to modulate the conductance of semiconductor surface [50,123]. In Si, μ of 1500 $cm^2V^{-1}s^{-1}$ is a typical value at low doping level.

Modulation doping technique has prompted exceedingly high μ to be obtained, using the concept of separating electrons from their parent donors [93-95,128]. This gave rise to the high electron mobility transistor (HEMT) as shown in Figure 5.1 (d). In modulation doped quantum structures in GaAs system, there are 7000-fold μ enhancement from 5×10^3 $cm^2V^{-1}s^{-1}$ in 1977 to 3.6×10^7 $cm^2V^{-1}s^{-1}$ in 2007 [96]. This astonishing result has been possible through suppression of ionized impurity scattering as well as a triumph of material science, such as high crystallinity, low charged impurity density, and interface control in GaAs system [129,130]. This high μ also leads to the discovery of fractional quantum Hall effect [131,132], which is a new phenomena.

The Ⅲ-Ⅴ nitrides have supported the high temperature and high power applications [10-12], vacant to Si-MOSFET and GaAs-HEMT technology, emerging as an important semiconductor system with already commercially available optoelectronic products [133]. The large polarization and large band offsets create 2DEG, even without any intentional doping [122,134]. This polarization induces very high density of carriers in the order of 10^{13} cm^{-2}. Even if the μ is much lower (maximum~10^5 $cm^2V^{-1}s^{-1}$) [135] than GaAs system due to lower crystallinity, the high carrier density

enables to make smaller chips and higher device impedance. GaN HEMT [136-139] is also extensively investigated. Actually, the larger bandgap and high breakdown voltage of this system is a priority to high μ, when high power device application is considered. On the other hand, modulation doping technique is often used to increase carrier density more, that is, n-type $Al_{1-x}Ga_xN$ is depart from GaN with undoped $Al_{1-x}Ga_xN$ (spacer) in the middle [140-141]. But there is a propensity that modulation doping is working in GaN system [142-144], probably due to large defect, interrupting the effect of spacer [145-147].

5.2 Scattering mechanisms of 2DEG

The scattering theory of 2DEG is somewhat different from usual scattering mechanism of carriers in three-dimensional transport. Because the motion of carriers is constrained in the confined well, the tendency of μ vs. temperature and μ vs. two-dimensional carrier density (n_s) is different from bulk single crystal [148], and also interface roughness (IR) scattering is included. In this section, Coulomb scattering related with charged traps such as remote ionized dopant, background impurities, and dislocation is discussed. And phonon scattering such as deformation potential acoustic, piezoelectric acoustic, and polar optical scattering, which are most important process in Ⅲ-Ⅴ compound semiconductors, is presented. Lastly, IR and alloy-disorder scattering, dominant at high n_s, is presented. Figure 5.2 represents a universal curve of μ vs. electric field in Si MOSFET [124] and temperature dependent μ in $Al_xGa_{1-x}As$/GaAs 2DEG [149].

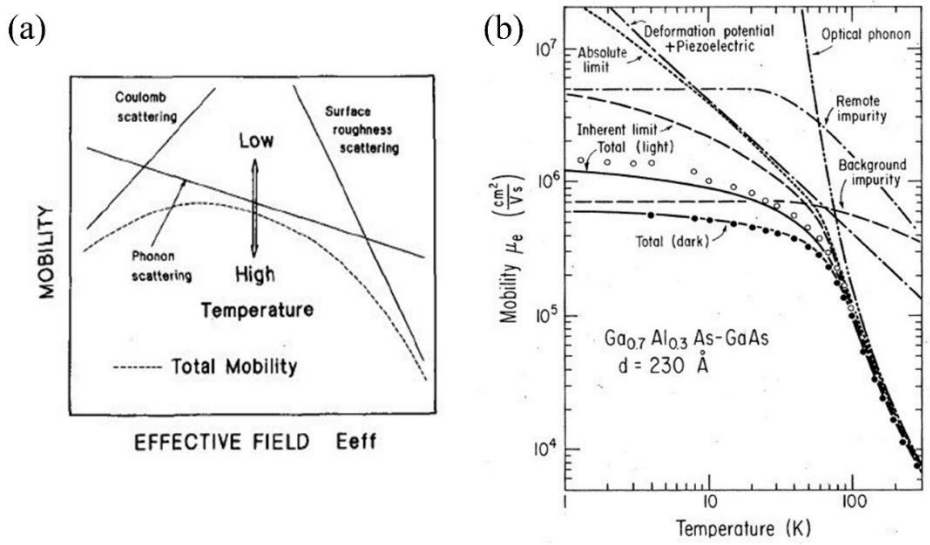

Figure 5.2: (a) Universal curve of μ vs. electric field in Si. (b) μ vs. temperature in $Al_xGa_{1-x}As/GaAs$.

Each scattering rate is evaluated using Fermi's golden rule. The wavefunction of electrons in 2DEG is [148,150],

$$\langle r|k\rangle = \frac{1}{\sqrt{A}} e^{ik\cdot r}\chi(z)u_{nk}(r) \tag{5.1}$$

in which is decomposed into a plane-wave part in the 2-dimensional x-y plane of area A and a finite extent in the z-direction governed by $\chi(z)$. k, r are two-dimensional vectors in x-y plane and $u_{nk}(r)$ are the Bloch wavefunction. Fang and Howard [151] first proposed $\chi(z)$ with a variational parameter b_0 by;

$$\chi(z) = \begin{cases} \left(\frac{b_0}{2}\right)^{1/2} z \, exp\left(-\frac{b_0 z}{2}\right) & (z > 0) \\ 0 & (z < 0) \end{cases} \tag{5.2}$$

For elastic scattering, the scattering rate from a state $|k>$ to a state $|k'>$ is written as[148-150],

$$\frac{1}{\tau} = \int dz \;\; N(z) \;\; \sum_{k'} \frac{2\pi}{\hbar} |\langle k'|V(r,z)|k\rangle|^2 \delta(\epsilon_k - \epsilon_{k'}) (1 - cos\theta)$$

(5.3)

Where $N, \hbar, V(\mathrm{r},\mathrm{z}), \epsilon, \theta$ are density of scatters in z direction in area A, Dirac constant, scattering potential, energy of state, and scattering angle, respectively.

5.2.1 Coulomb scattering

At low temperature, mostly the dominant scattering is Coulomb scattering. An ionized charge at a distance z_0 from the heterointerface has a Coulomb potential [148,150];

$$V_{uns}(\mathrm{r}, z_0) = e^2/4\pi\varepsilon_0\varepsilon(0)\sqrt{r^2 + {z_0}^2} \tag{5.4}$$

where $V_{uns}, \varepsilon_0, \varepsilon(0)$ are unscreened potential, vacuum permittivity, relative dielectric constant at zero frequency, respectively. Then, the Fourier-transformed screened potential is given,

$$\mathrm{V(q)} = \frac{V(q,z_0)}{\varepsilon(q)} = \int_0^\infty r dr \;\; \int_0^{2\pi} d\theta \;\; \frac{e^2}{4\pi\varepsilon(q)\sqrt{r^2+{z_0}^2}} exp^{iqrcos\theta} = \frac{e^2}{2\varepsilon_0\varepsilon(0)} \frac{exp^{-qz_0}}{q+q_{TF}}$$

(5.5)

The damped term exp^{-qz_0} is shown if ionic charge is remote, and q_{TF} is a Thomas-Fermi screening wavevector, q_{TF} (n_s, T), becomes $\frac{2m^*e^2}{4\pi\varepsilon_0\varepsilon(0)\hbar^2}$ in low temperature, being independent in temperature.

Based on (5.3) and (5.5), when all ionized impurities are located a distance d (substitution for z_0 in this case) from heterointerface with areal density of N_{2D}, like delta-doped sheet, the scattering rate becomes;

$$\frac{1}{\tau} = N_{2D} \frac{m^*}{2\pi\hbar^3 {k_F}^3} \int_0^{2k_F} |V(q)|^2 \frac{q^2}{\sqrt{1-(\frac{q}{2k_F})^2}} \tag{5.6}$$

where $k_F = \sqrt{2\pi n_s}$ is the Fermi wavevector. The detailed scattering rate depends on the distribution of electron wavefunction.

For remote ionized dopants ($k_F d \gg 1$), i.e., when 2DEG and dopants are far apart, a simple analytical formula for μ at T=0 is;

$$\mu_{remote,delta} = \frac{8e(k_F d)^3}{\pi\hbar N_{2D}} \tag{5.7}$$

which has a $n_s^{3/2}/N_{2D}$ dependence [129].

For background charged impurities with donor density of N_{res}, μ can be approximated to a form,

$$\mu_{res} \approx \frac{4(2\pi)^{5/2}\hbar^3(\varepsilon_0\varepsilon(0))^2}{(m^*)^2 e^3} \times \frac{n_s^{3/2}}{N_{res}} \tag{5.8}$$

which has a $n_s^{3/2}/N_{res}$ dependence [148].

For dislocation scattering with TD density of N_{dis}, scattering rate becomes [152];

$$\frac{1}{\tau} = N_{dis}\frac{m^*}{2\pi\hbar^3 {k_F}^3}\int_0^{2k_F}|V(q)|^2\frac{q^2}{\sqrt{1-(\frac{q}{2k_F})^2}} \tag{5.9}$$

And it is found to be $\mu_{dis} \propto n_s^{3/2}/N_{dis}$ for a perfect 2DEG with a line dislocation with a uniform charge density. Figure 5.3 (a) illustrates μ vs. n_s as varying spacer layer thickness (d) for $Al_xGa_{1-x}As$/GaAs, calculated when charged dopant exists in $Al_xGa_{1-x}As$ layer [153]. Figure 5.3 (b) shows as μ vs. n_s as varying N_{dis} in $Al_xGa_{1-x}N$/GaN, which have predominantly dislocation limited transport [145].

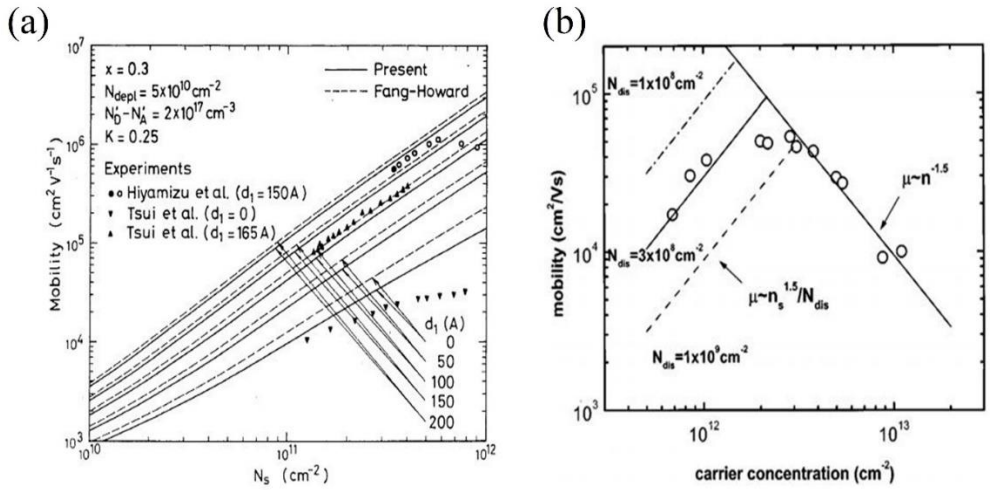

Figure 5.3: (a) μ vs. n_s for ionized dopant scattering in n-$Al_xGa_{1-x}As$/GaAs (b) μ vs. n_s for dislocation scattering in $Al_xGa_{1-x}N$/GaN

5.2.2 Phonon scattering

Deformation potential acoustic, piezoelectric acoustic, and polar optical phonon scattering are most important process in Ⅲ-Ⅴ compound semiconductors [141,149,154] .

Acoustic phonon scattering is essentially elastic because its linear dispersion makes its energy low. When displacement of atoms from their lattice sites are induced by crystal vibrations, a modification of band structure arise. So electrons in the conduction band have relations to the deformation potential acoustic phonon. Piezoelectric scattering arises in strongly polar materials and has a complicated angular dependence.

Polar optical phonon scattering is highly inelastic due to large optical phonon energy. So it is hard to find an analytic expression.

The details is not outlined in this dissertation, because the transport of BSO films is not limited by phonon scattering now. There are many charged defect and impurities limiting its transport.

5.2.3 Interface roughness scattering and alloy disorder scattering

As n_s increases, 2DEG tends to shift closer the interface. Since it is impossible to grow perfectly atomically flat surface, interface roughness (IR) scattering [155] can be severe if n_s is high. The influence of IR on μ is not precise to determine because of the difficulty of modeling the roughness itself. Ferry and Goodnick [156] have addressed this problem and led to be approximately $\mu \propto n_s^{-2}$, which also depends on interface roughness and correlation length.

In Ⅲ-Ⅴ compound semiconductors, as n_s increases, alloy disorder scattering [149, 153] originates from the randomly varying alloy potential in the barrier. Alloy scattering occurs as a result of the finite penetration of the 2DEG into the barrier.

All the scattering rate can be combined by Mattiessen's rule;

$$\frac{1}{\tau_{total}} = \frac{1}{\tau_{Coulomb}} + \frac{1}{\tau_{phonon}} + \frac{1}{\tau_{IR}} + \frac{1}{\tau_{others}} \tag{5.10}$$

5.3 Polar interface

The formation of 2DEG by polarization doping have been most widely investigated in $Al_xGa_{1-x}N$/GaN interface, in which the inherent piezoelectricity of spontaneous and tensile strain induced, enables making high density n_s~10^{13} cm^{-2} [122,134,157]. Quantum Hall effects [158] were observed and this system and HEMT [136-139] using such interface are already commercialized in RF applications and power devices. Another polarization doped heterointerface is $Mg_xZn_{1-x}O$/ZnO [159], which is a WBGs and have a wurzite structure like GaN. $Mg_xZn_{1-x}O$/ZnO exhibits also high n_s without any extrinsic charged dopant and quantum Hall effects [160] were observed, too. These two type of polar interface are driven basically by intrinsic polar structure, even making larger polarization under appropriate strain.

For more than a decade, 2DEG behavior at $LaAlO_3/SrTiO_3$ perovskite oxide interface

has been studied extensively. Ohtomo and Hwang [161] observed 2DEG in $LaAlO_3/SrTiO_3$ without any extrinsic charged dopant, having insulating property of each own layer with large bandgap ($LaAlO_3 \approx 5.6$ eV, $SrTiO_3 \approx$ 3.2 eV), only if the termination of $SrTiO_3$ layer is TiO_2 layer, with extremely high μ exceeding 10^4 $cm^2V^{-1}s^{-1}$ in low temperature. In addition, superconductivity [162] and magnetism [163] have been reported in $LaAlO_3/SrTiO_3$ interface. In this system, the polar nature of $LaAlO_3$ layer is believed to play an important role in the formation of 2DEG [164,165], but there is another possible assertion related with instability of $SrTiO_3$ substrate [166-168]. Many report have pointed out the oxygen instability of this interface.

Recently, U. Kim *et al*. [121], reports 2DEG at $LaInO_3$ (LIO)/$BaSnO_3$ polar interface. Each layer is an insulator with large bandgap (LIO≈5 eV, BSO≈3 eV). The interface exhibits a sheet conductance enhancement up to several orders of magnitude by polarization doping. In this system, the doping level of BSO by La, is found to be a critical parameter for the formation of 2DEG. The major advantages of LIO/BSO interface are its excellent oxygen stability and high μ expected from BSO channel layer.

In this section, 2DEG in the perovskite oxide interface driven by polarization doping is discussed. Polar catastrophe model, explaining the origin of $LaAlO_3/SrTiO_3$ conducting interface, is presented and the problem about oxygen instability is discussed. And properties of LIO/BSO interface and its special advantages are described.

5.3.1 Mechanisms and limitation of $LaAlO_3/SrTiO_3$ interface

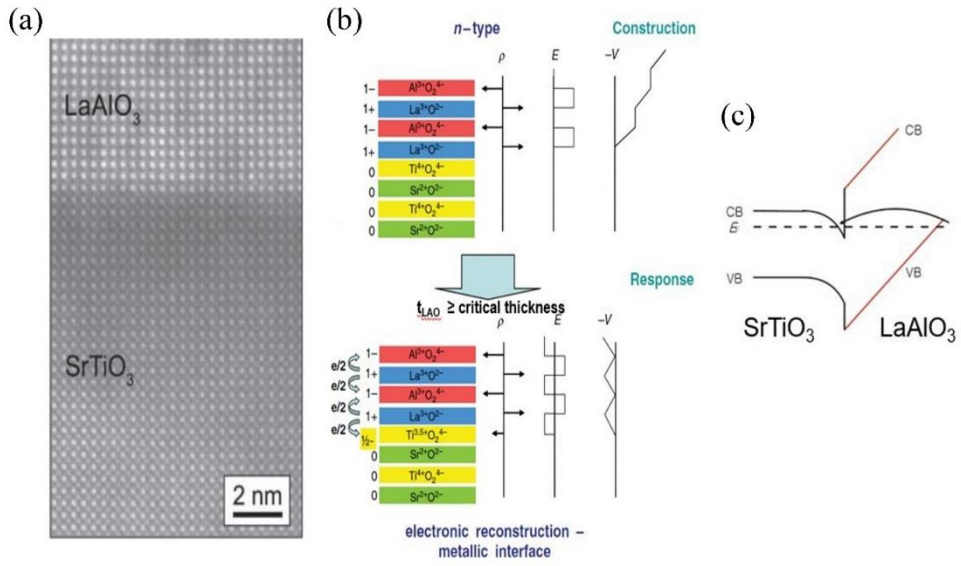

Figure 5.4: $LaAlO_3/SrTiO_3$ interface (a) STEM image of interface (b) Polar catastrophe model (c) Band bending diagram

Figure 5.4 (a) shows a HAADF-STEM image of the sharp interface between $LaAlO_3$ film and $SrTiO_3$ substrate [162]. Figure 5.4 (b) describes redistribution of electrons to break polar catastrophe in the scheme of atomically abrupt valence discontinuity with TiO_2 termination layer in $SrTiO_3$ substrate [169]. If each layer of LaO^+ and AlO_2^- in $LaAlO_3$ film continues to have alternating net charges by its valence nature, electric potential diverges with increasing thickness. This divergence catastrophe can be solved if half of an electron is added to the last TiO_2 layer. This electronic reconstruction makes a metallic interface between $LaAlO_3$ and $SrTiO_3$ and the end AlO_2 layer loses half of an electron. Figure 5.4 (c) illustrates band bending diagram based on the polar catastrophe model, which is different from GaN system [122]. In this case, The origin of electrons is valence band of $LaAlO_3$, not surface donor state.

While the existence of critical thickness and the observation of the built-in electric field in the $LaAlO_3$ layer support this scenario [164-165,170], the deviation of oxygen stoichiometry in $SrTiO_3$ also well explains the formation and many properties of 2DEG in $LaAlO_3/SrTiO_3$interfaces. Figure 5.5 (a) [166] show a disappearance of conducting interface when the deposition of $LaAlO_3$ is done in oxygen rich

environment. Annealing the $LaAlO_3/SrTiO_3$ interface in O_2 environment also reduces the 2DEG density as illustrated in Figure 5.5 (b) [171]. Numerous study for the observation of 2DEG at $SrTiO_3/SrTiO_3$ [168], amorphous $LaAlO_3/SrTiO_3$ [172], amorphous $SrTiO_3/SrTiO_3$ [173], Co-doped $(La,Sr)TiO_3/SrTiO_3$ [166,174] also support the origin of conducting $LaAlO_3/SrTiO_3$ interface is strongly related with oxygen vacancy of $SrTiO_3$. And this instability is a major flaw for $LaAlO_3/SrTiO_3$ 2DEG.

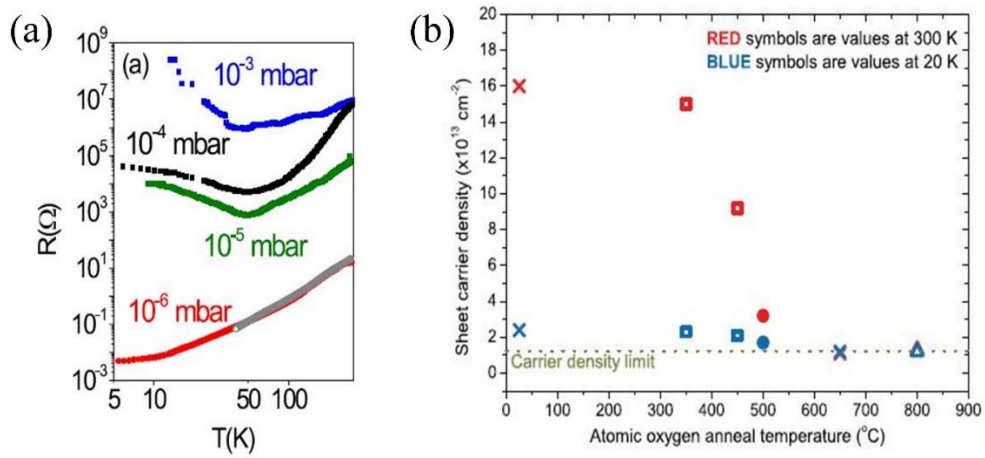

Figure 5.5: Oxygen instability of $LaAlO_3/SrTiO_3$ interface. (a) Resistance vs. temperature as varying the O_2 deposition pressure. (b) n_s change as a function of annealing temperature.

5.3.2 Mechanism and advantages of $LaInO_3/BaSnO_3$ interface

LIO/BSO interface has an atomic configuration like $LaAlO_3/SrTiO_3$ interface, that is, each atomic plane of LIO has an alternating charges. Figure 5.6 (a) shows excellent epitaxial growth of LIO layer on BLSO layer on $SrTiO_3$ substrate with undoped BSO buffer layer. And Figure 5.6 (b) show the sheet conductance enhancement as varying La doping rage of BLSO layer after deposition of LIO layer. This conductance enhancement is as large as a factor of 10^4 in low La doping rate, and as La concentration exceeds 1 % the slight enhancement is shown due to metallic nature of BLSO in high doping rate.

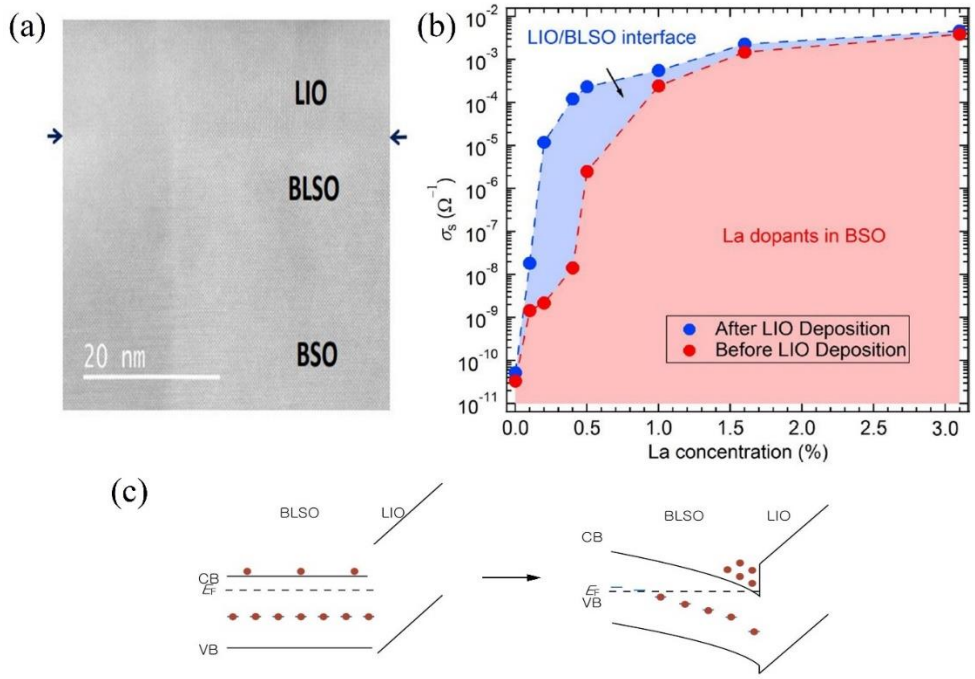

Figure 5.6: LIO/BSO interface. (a) STEM image. (b) Sheet conductance changes as varying La concentration in the LIO/BLSO interface. (c) Band diagram model describing the origin of 2DEG.

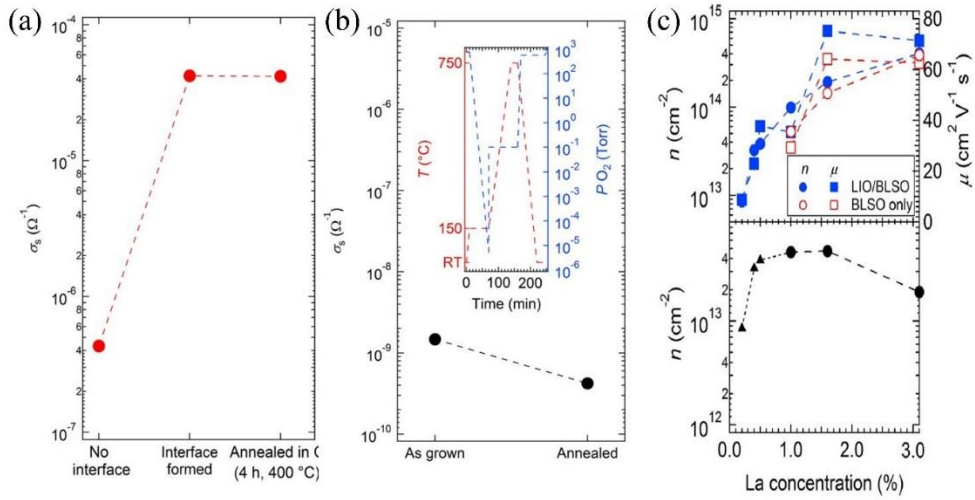

Figure 5.7: Oxygen stability of LIO/BSO interface (a) Sheet conductance variation of LIO/BLSO interface after annealing in O_2 environment in 1 atmosphere. (b) Sheet conductance variation of BLSO layer after annealing in the conditions of following LIO deposition (inset). (c) n_s and μ as varying La concentration.

The mechanism of 2DEG in LIO/BSO polar interface is related to a polar nature of LIO and a control of Fermi level by La doping on BSO layer. Because same experiment to see the conductance enhancement in BHO/BSO and $SrZrO_3$/BSO interface did not show improved conductance, the polar nature of LIO is a key for the formation of metallic states in LIO/BSO interface. And insulating property in LIO/undoped BSO in Figure 5.6 (b) indicates La doping is required. At this stage, Figure 5.6 (c) model suggests the origin of 2DEG in LIO/BSO interface on $SrTiO_3$ substrate. The trapped electrons in large density of TDs in BLSO are attracted by polarization of LIO and confined in the well, and complete the formation of 2DEG.

Advantages of LIO/BSO interface than $LaAlO_3$/$SrTiO_3$ interface are its oxygen stability and availability of high μ BSO channel layer. Figure 5.7 (a) shows the formed 2DEG in LIO/BLSO interface not exhibiting considerable change of sheet conductance after annealing in O_2 atmosphere. And Figure 5.7 (b) describes oxygen stable BLSO layer when annealed in the condition of following LIO deposition, indicating the excellent stability of BSO. The stability of LIO/BSO interface is also confirmed in Figure 5.7 (c), describing n_s and μ as a function of La concentration, implying the importance of Fermi level in BLSO layer. The control of transport property in 2DEG as changing La doping rate on BSO layer is possible because LIO/BSO interface has a robust oxygen stability. Instable interface formed by unintentional oxygen vacancy will make hard to control carrier density by external doping. Also, high room temperature μ of BSO have a great potential to realize high μ polar interface, compared to $LaAlO_3$/$SrTiO_3$ interface.

5.4 Modulation doping in $LaInO_3/BaSnO_3$ polar interface (LIO/BSO/BLSO)

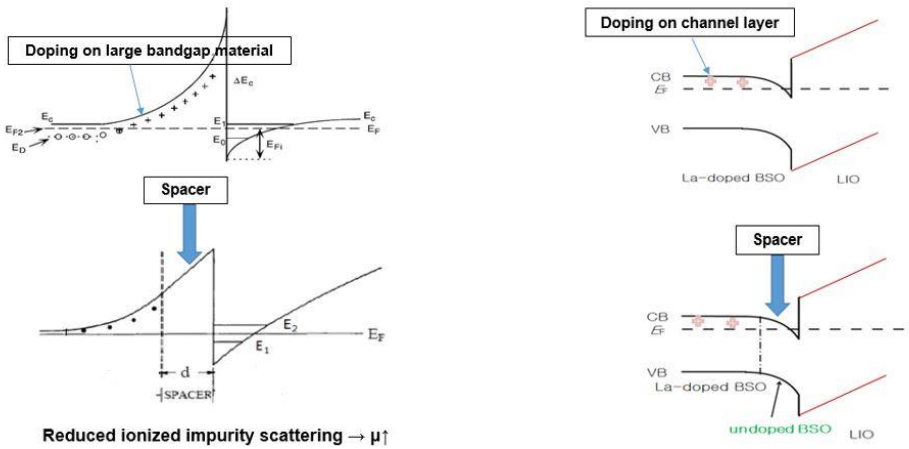

Figure 5.8: Conventional modulation doping vs. modulation doping in LIO/BLSO polar interface

The stable LIO/BSO interface requires a slight La doping on BSO layer to make high n_s in the order of 10^{13} cm^{-2} by forming LIO/BLSO interface [121]. The best idea for creating high n_s in 2DEG is a doping on a larger bandgap of LIO material, like n-$Al_xGa_{1-x}N$/GaN interface [140-141], because BLSO channel layer may suffer from La ionized dopant scattering. It remains to seen if the large bandgap LIO material can be doped in spite of its 5 eV bandgap. Meanwhile, it is very important to confirm that modulation doping technique is working as designed in the LIO/BLSO polar interface to make sure that the future efforts to reduce the defects and increase its mobility will be worthwhile. Figure 5.8 illustrates the difference between conventional modulation-doped heterostructure and modulation-doped LIO/BLSO polar interface. Undoped spacer layer, which has no ionized impurities, are inserted in channel layer instead of larger bandgap barrier layer.

5.4.1 Hall measurement (LIO/BSO/BLSO interface)

The fabrication process of LIO/BSO/BLSO interface is described in Figure 5.9 by four thermal cycle (room temperature→750 °C→ room temperature). First 110 nm thick-undoped BSO buffer layer is deposited on $SrTiO_3$ substrate (5×5 mm^2). Then 12 nm thick 0.2 % La-doped BSO layer is deposited with a square shape of (2×2 mm^2) using a Si stencil mask. In this step, undoped BSO layer (spacer) is also sequentially deposited. The 4 % La-doped BSO as a metal electrode is deposited using another Si mask with 4 overlapped areas of (0.2×0.2 mm^2). Finally, 10 nm thick-LIO layer is deposited over the area of (3×3 mm^2) to cover the lower BLSO layer.

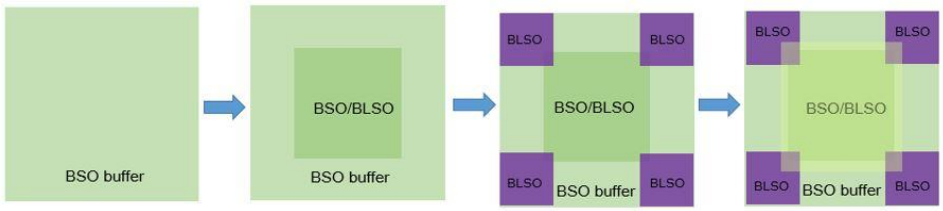

Figure 5.9: Fabrication process of LIO/BSO/BLSO interface

Figure 5.10 (a) and (b) describes the lateral and vertical structures of LIO/BSO/BLSO interface for the Hall measurement using the square van der Pauw geometry. The distinguishing feature is the inserted undoped BSO spacer layer on top of the fixed donor density of BLSO layer, so we can investigate the transport dependence on the distance to remote La ionized impurities.

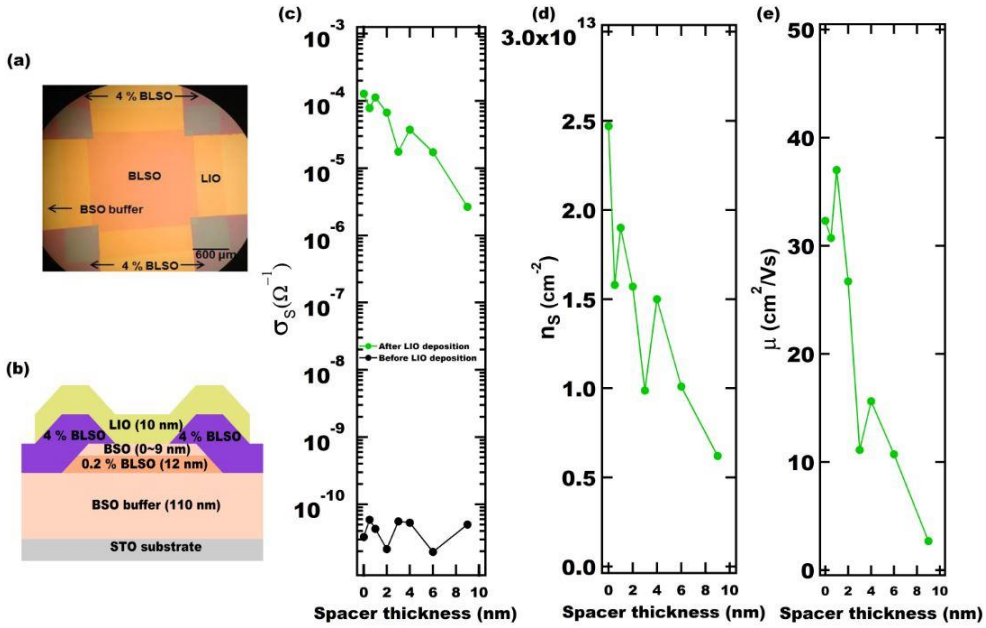

Figure 5.10: The Hall measurement result of LIO/BSO/BLSO interface as varying spacer thickness. (a) Top view of structure by optical microscope. (b) Cross-sectional diagram of structure. (c~e) σ_s, n_s, and μ_H vs. d.

The sheet conductances (σ_s) as a function of varying spacer thickess (d) are shown in Figure 5.10 (c). In each sample, we measured σ_s before and after the LIO deposition, exhibiting conductance enhancement of up to 6 orders of magnitude. Before LIO deposition, the samples were insulating with or without a spacer layer because the threading dislocations of a large density of 10^{10}~10^{11} cm^{-2}, trap substantial electrons of about 4 x 10^{19} cm^{-3} in BLSO films [68,120]. However, the polarization doping after LIO deposition makes substantial band bending, resulting in the conducting interface. This result also confirms earlier report, showing that the origin of 2DEG at LIO/BLSO interface is not from La diffusion or the creation of oxygen vacancies. As d increases, σ_s of 2DEG continually decreases, resulting in about 2 orders of magnitude decrease at the spacer layer thickness of 9 nm.

At the same time n_s and μ_H continually decreases with increasing d as plotted in Figure 5.10 (d) and (e). The n_s changes from 2.47 x 10^{13} cm^{-2} to 6.20 x 10^{12} cm^{-2}

and μ_H from 32.3 cm^2/Vs to 2.68 cm^2/Vs as *d* increases from 0 to 9 nm, which, at first sight, does not seem the desired effect of the spacer layer and modulation doping. Because the carriers originate from the smaller bandgap BLSO layer and are drawn to the interface by polarization, n_s sharply decrease. This is different from the conventional modulation doped structures of III-V semiconductors [175-177], in which diffusion of the electrons from the larger bandgap material are hardly hindered by insertion of a spacer layer. Roughly, when thinking about conventional modulation-doped heterostructure, driving force due to diffusion is inversely proportional to distance. So n_s becomes [178];

$$n_s \sim \frac{dN_D}{dx} \sim \frac{1}{d} \tag{5.11}$$

where N_D, x are donor density and distance between donor site and heterointerface, respectively. And if we treat a free charge distant *d* apart from bound charged plates (dipole), not considering any screening, the force is proportional to $\frac{1}{d^\alpha}$ $(2 < \alpha < 3)$, where α depends on *d* and dipole size (a). So n_s becomes;

$$n_s \sim \frac{a(2d+a)}{d^2(d+a)^2} \sim \frac{1}{d^{2\ or\ 3}} \tag{5.12}$$

This is rough estimation, not considering any screening and band bending effect. But the steep decrease of n_s with spacer thickness is expected from this picture.

The first possible origin for the decrease of μ_H with *d* is that the Coulomb scattering by La dopant is not dominant in transport, inhibiting the advantages of modulated structure. The effect of inserting spacer can be seen if the dominant scattering is driven by remote ionized impurities in that system. It is well known that the transport of BLSO film is limited by threading dislocations [1,68], and a recent FET experiment on BSO [179] has found a dependence of $\mu \propto n_s^\gamma$ where $\gamma \cong 1.5$, as reported in 2DEG in GaN [145].

Another possibility is that the screening for remote charges by two dimensional free carriers is not very effective; μ becomes higher as increasing n_s by enhanced kinetic energy in the well. Coulomb scattering is reduced when the velocity of free

carriers is high. So, Coulomb scattering by doped ionized impurity for two-dimensional carriers has a dependence of $\mu \propto n_s^{\gamma}$, where $\gamma =$ 1~1.7, as reported in 2DEG of Si and the compound semiconductors [123,153,180]. Therefore μ enhancement in modulated structure is negated by the decrease of n_s by the inserted spacer layers. This is reinforced by the fact that μ_H remains similar in spite of up to 36 % decrease of n_s in the range of d = 0~2 nm, although μ_H decrease sharply from d = 3 nm. This suggests that μ of modulated structure may be enhanced if n_s is supported by other means, for example by field effect.

5.4.2 Self-consistent 1D Poisson-Schrodinger calculation

Under the assumption that defect-free system except intentional charged impurity doping, the band bending profile in heterostructure can be obtained by calculating one dimensional (1D) Poisson-Schrodinger equation self-consistently [181]. Poisson equation in 1D with x coordinate follows;

$$\frac{d}{dx}\left(\varepsilon_s(x)\frac{d}{dx}\right)\phi(x) = \frac{-q[N_D(x)-n(x)]}{\varepsilon_0} \tag{5.13}$$

where ε_s, ϕ, N_D, n, ε_0 are dielectric constant, electrostatic potential, ionized donor concentration, free electron density distribution, and vacuum permittivity, respectively. And Schrodinger equation, precisely estimating electron distribution in quantum well, follow;

$$-\frac{\hbar^2}{2}\frac{d}{dx}\left(\frac{1}{m^*(x)}\frac{d}{dx}\right)\psi(x) + V(x)\psi(x) = E\psi(x) \tag{5.14}$$

where $\hbar$, m^*, ψ, V, E, are Dirac constant, conduction band effective mass, electron wave function, potential energy, and respectively. The potential energy V is related to ϕ as follows;

$$V(x) = -q\phi(x) + \Delta E_c(x) \tag{5.15}$$

where, ΔE_c is the pseudopotential energy due to the band offset at the heterointerface.

Gregory Snider provides a 1D Poisson-Schrodinger program in the web site [], using

the finite difference method with a nonuniform mesh size. This program finds an accurate band bending profile and electron density distribution of heterostructure very efficiently.

The input condition for performing this program are boundary condition of each end, such as flat, Ohmic contact, Schottky contact, E-field slope, and basic material parameters, such as, bandgap, conduction band/valence band offset, dielectric constant, electron/hole effective mass, conduction band/valence band degeneracy, donor/acceptor ionization energy, electron/hole mobility, electron/hole lifetime, polarization, donor/acceptor concentration. Figure 5.11 illustrates an example of 1D Poisson-Schrodinger program result, i.e., conduction band and the electron wave function profile in heterostructure.

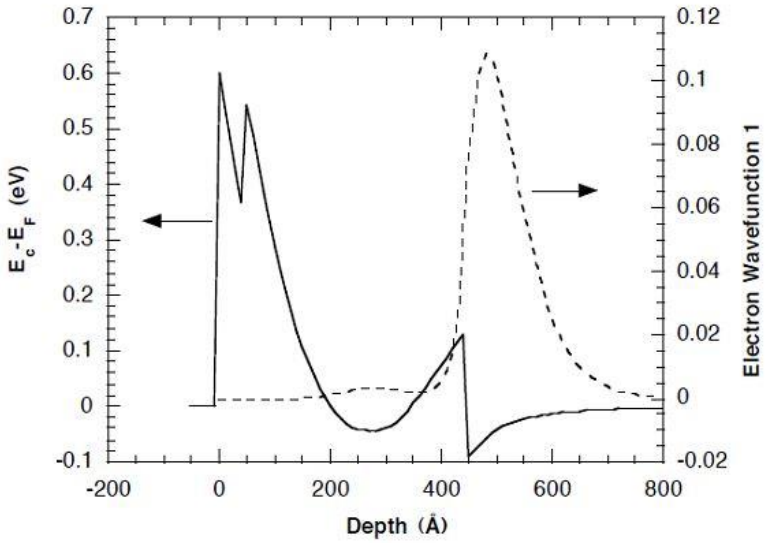

Figure 5.11: An example of performing 1D Poisson-Schrodinger program for n-GaAs/n-AlGaAs/AlGaAs/GaAs/AlGaAs/p-AlGaAs structure.

The result for performing snider program in LIO/BSO/BLSO interface is shown Figure 5.12. Band bending profile is described in Figure 5.12 (a) and three dimensional free carrier density (n_{3D}) distribution is in Figure 5.12 (b). The

dimensions of the structure are based on Figure 5.10 (b).

The values of bandgap energy and band offset are based on the band alignment reported in APL materials by U. Kim *et al* [121], which submitted the first paper about LIO/BLSO polar interface. We set $m^* = 0.42\ m_0$ [18] for the conduction band of BSO, while its s-like band structure helps using 1D Poisson-Schrodinger equation. The density of acceptor and donor are 4×10^{19} cm^{-3} and 2.87×10^{19} cm^{-3}, respectively. Because dislocations trap electrons in BLSO films [1,68], acceptor levels should be imposed and the value is based on the previous Hall result as a function of varying La doping [120].

Also we set P = 12.5 μC/cm^2 in 10 nm thick LIO layer in order to satisfy the experimental n_s value at d = 0. There exist uncertainty in the polarization magnitude as well as the thickness of the LIO with such polarization, which will require subatomic resolution study of the interface structure. However, as illustrated in Figure 5.12 (a), such polarization enables a confined well at the interface. The width and depth of the well decrease as increasing the spacer thickness, which is well illustrated in the inset of Figure 5.12 (a) and Figure 5.13.

The free carrier density at the interface continuously decreases as described in Figure 5.12 (b) and exists in the length scale of 1~2 nm. The peak n_{3D} decreases from 2.03×10^{20} cm^{-3} to 7.88×10^{19} cm^{-3}, as the spacer layer thickness increases from 0 to 9 nm. Recent thermoelectric power measurement has found the confinement length to be about 1 nm. [183]

The plot in Figure 5.12 (c) compares n_s from the experiment results in Figure 5.10 with those from the calculation as varying the spacer thickness. The two results agree quite well, but the experimental results decrease slightly faster as increasing d. The discrepancy in n_s for the 9 nm spacer layer case is 2.31×10^{12} cm^{-2}.

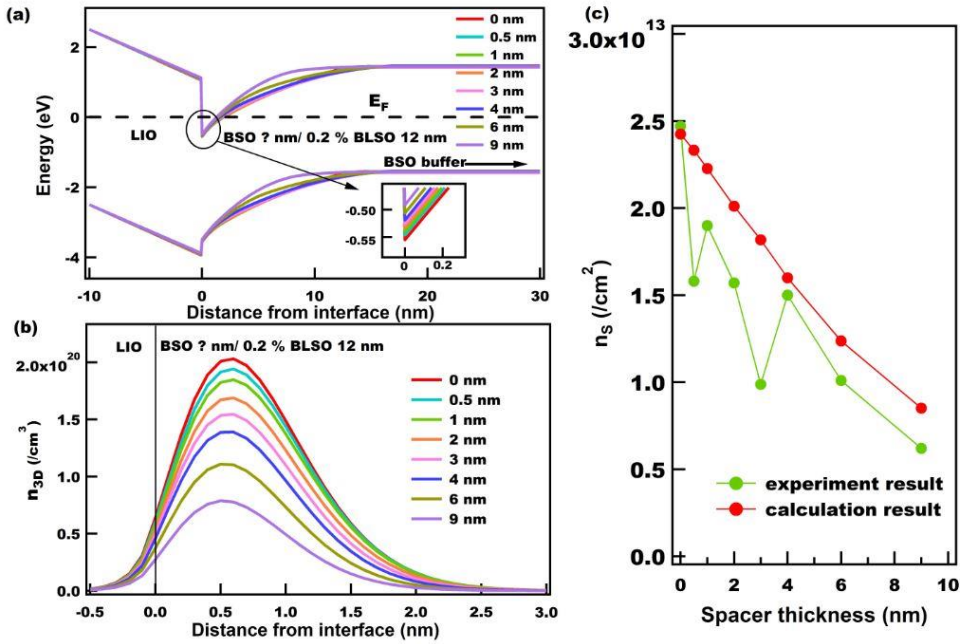

Figure 5.12: 1D Poisson-Schrodinger calculation result for LIO/BSO/BLSO interface (a) Band bending profile. (b) Free electron concentration profile. (c) n_s vs. d for Hall measurement result and calculation result.

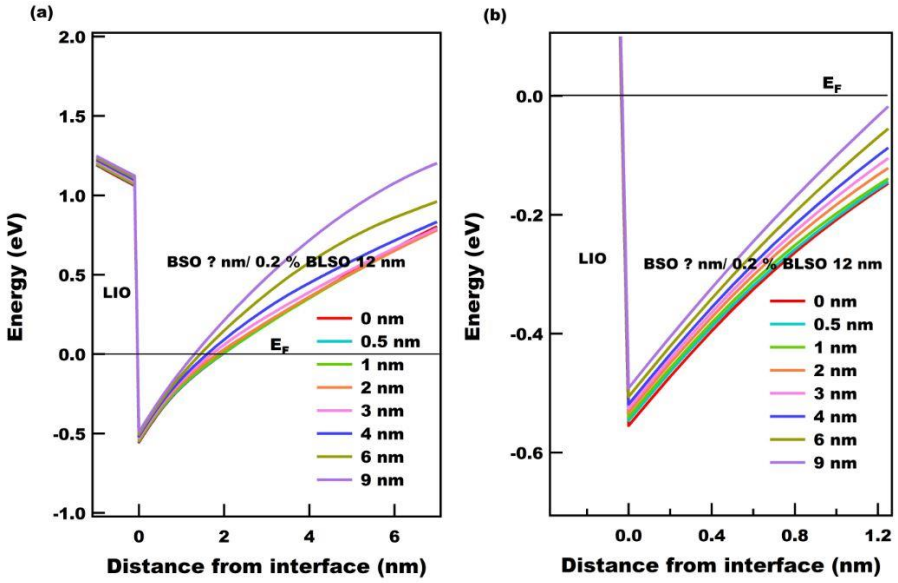

Figure 5.13: Conduction band edge profile, which is enlarged version of Figure 5.11 (a). The difference of band bending (a) and the difference of well depth (b) are well shown.

5.4.3 Field effect transistor based on LIO/BSO/BLSO interface

We fabricated the field effect device to control n_s continuously at fixed d. This also reduces the error coming from the fluctuation of the spacer layer thickness. Previous study of FET using epitaxial BLSO and LIO demonstrates the excellent interface property [7]. The fabrication process is like the outlines introduced in ″3.4.1 FET fabrication process″, except using a highly conductive 4 % La-doped BSO for the electrodes and 244 nm thick LIO as the gate oxide. Total five thermal cycle (room temperature→750 °C→ room temperature) is performed to make one FET device.

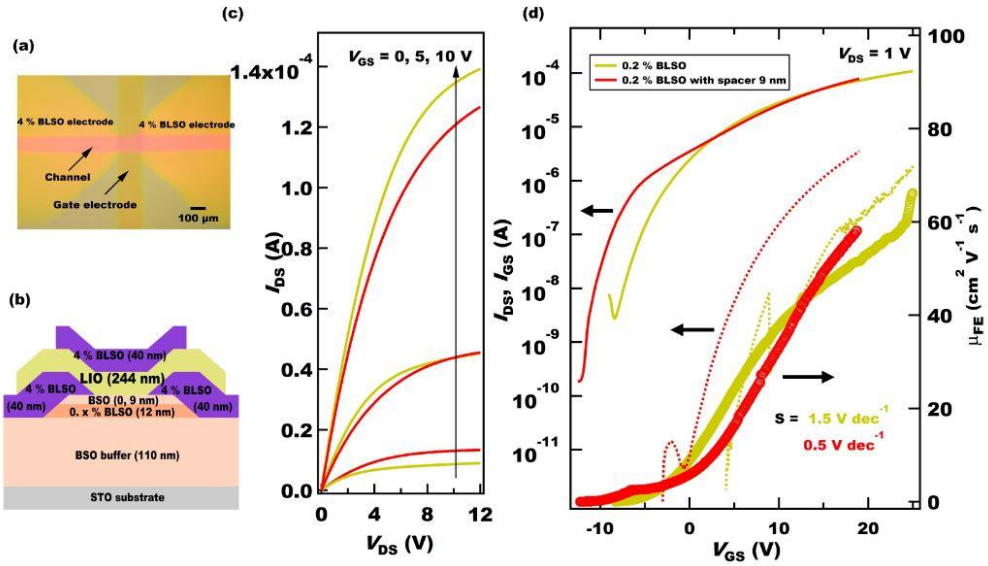

Figure 5.14: FET result of LIO/BSO (d=0,9 nm)/BLSO (La doping rate=0.2%). (a) Top view of device by optical microscope. (b) Cross-sectional diagram of device. (c) Output characteristics. (d) Transfer characteristic.

The top view and vertical view of structures are shown in Figure 5.14 (a) and (b). We fabricated four transistors with interfaces of LIO/0.2 % La-doped BSO, LIO/BSO(9 nm)/0.2 % La-doped BSO, LIO/0.4 % La-doped BSO and LIO/BSO(9 nm)/0.4 % La-doped BSO, respectively. The channel length and the width are around 140 μm and

110 μm, respectively. The typical output and transfer characteristics for transistor with and without a spacer layer with the same 0.2 % La-doped BSO channel layer are plotted in Figure 5.14 (c) and (d). The properties of 0.4 % La-doped BSO channel layer are shown in Figure 5.15. The drain-source current (I_{DS}) versus the drain-source voltage (V_{DS}) at various gate-source voltages (V_{GS}) in output characteristics indicates that the devices operate in an n-type accumulation mode and pinch-off occurs at high V_{DS}. The transfer characteristics in Figure 5.14 (d) represents I_{DS} versus V_{GS} at the linear region of V_{DS} = 1 V as confirmed in Figure 5.14 (c). In all devices, we applied V_{GS} while keeping the gate-source current (I_{GS}) level 1~2 orders of magnitude lower than I_{DS} to avoid a breakdown of gate oxide. I_{DS} reach around 10^{-4} A in the both cases in highly accumulated region. It should be pointed out that μ_{FE} in the devices with a spacer layer are higher than those without a spacer layer above 13 V. This phenomenon occurs also for FETs with 0.4 % La-doped BSO channel layer. μ_{FE} with 9 nm spacer shows steeper increase above V_{GS} = 17 V.

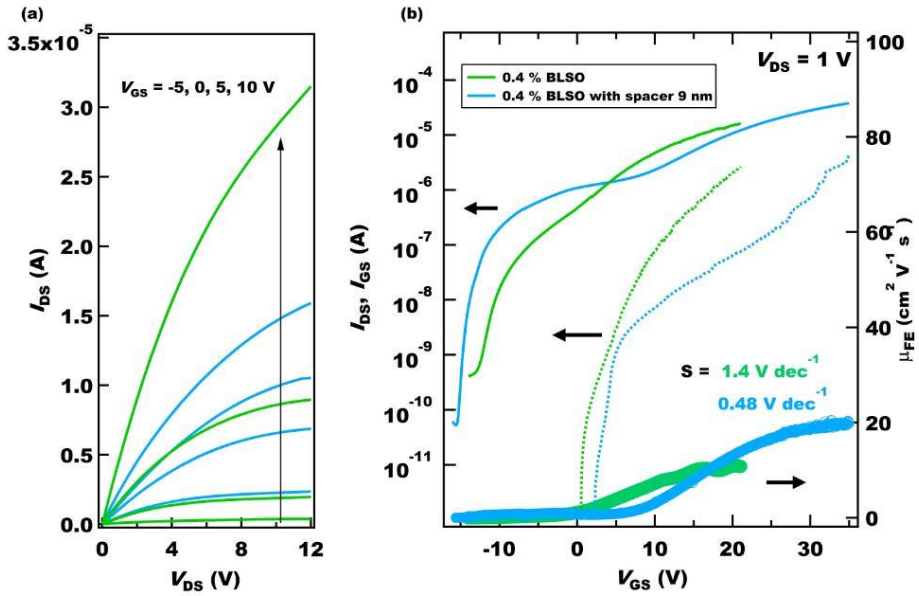

Figure 5.15: FET result of LIO/BSO (d=0,9 nm)/BLSO (La doping rate=0.4%). (a) Output characteristics. (b) Transfer characteristic.

Threshold voltage (V_{th}) is -1.45 V and 0.2 V (with spacer) for 0.2 % BLSO channel, and -1.2 V and 4 V (with spacer) for 0.4 % BLSO channel as shown in Figure 5.16 by extrapolation of the linearly fitted line of $I_{DS}^{1/2}$ vs. V_{GS} according to the standard square-law theory of FET: $I_{DS,sat} \propto (V_{GS} - V_{th})^2$ where $I_{DS,sat}$ is the saturation current in (3.9). [7,184]

It is interesting that the spacer FET in Figure 5.16 (d) shows additional linear decrease in the subthreshold region. In such subthreshold region, which is related to a diffusion current in MOSFET and to the pinch-off of both the drift current and the hopping mechanism in thin film transistor through the trap states, the relations of $I_{DS} \propto \exp(\frac{qV_{GS}}{nkT})$ and $S = \mathrm{n}\frac{kT}{q}\ln(10)$, where k, T, q, and n are Boltzmann constant, absolute temperature, electron charge, and a factor n, respectively, hold. [184,185] In our modulated structures, there is a possibility that La- doped layer below spacer layer contributes parallel conduction in the region of negative or small positive bias of V_{GS}, where n_s at LIO/BSO interface is small. This is manifested in the unusual transport in Figure 5.14 (c) and Figure 5.15 (a), where I_{DS} of the spacer FET is larger than that of the no spacer FET at small V_{GS} but I_{DS} of the no spacer FET eventually become larger than those of the spacer FET at high V_{GS}, leading to higher off-state current levels in the case of the spacer FETs. Similar behavior is seen in the transfer curves in Figure 5.14 (d) and Figure 5.15 (b) and it is more pronounced for the higher doped 0.4% BLSO channel layer.

On the other hand, *S* values for the spacer FETs are smaller (~1/3) than their counterparts in both 0.2 % La-doped and 0.4 % La-doped BSO channel, indicating smaller density of deep states at LIO/BSO interface than LIO/BLSO interface. [186] The analysis of the subthreshold region in our modulated structure with two parallel conduction channels, which usually arises in highly accumulated region by excessive forward bias in conventional MODFET [187], needs more careful study.

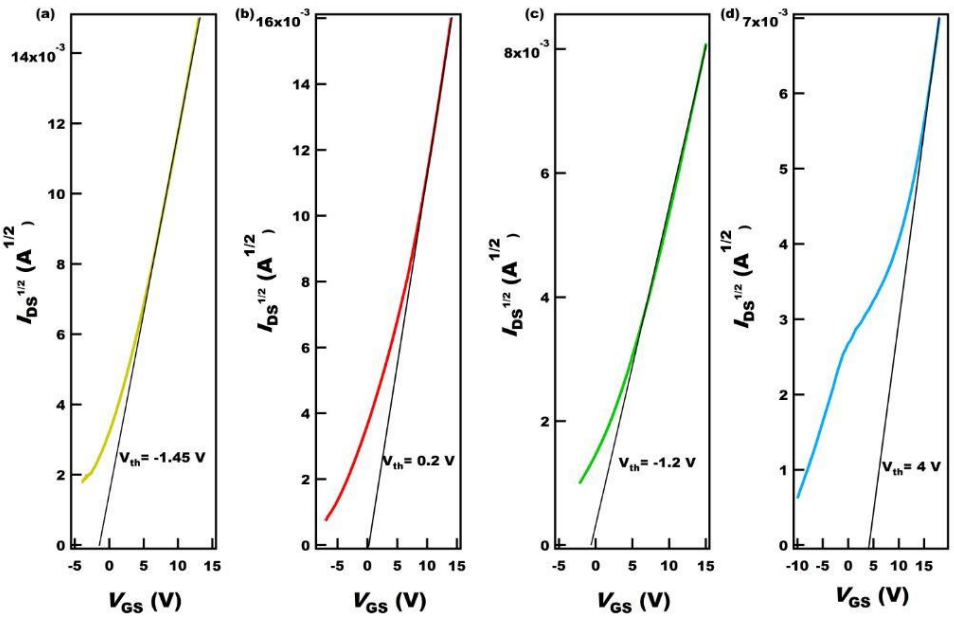

Figure 5.16: Transfer characteristic of LIO/BSO/BLSO FET in the saturated region of V_{DS}=13 V. (a) No spacer FET and (b) Spacer FET (d=9 nm) with 0.2 % La-doped BSO supply layer. (c) No spacer FET and (d) Spacer FET (d=9 nm) with 0.4 % La-doped BSO supply layer.

Figure 5.17 describes μ_{FE} versus n_s in our four types of FETs, where n_s is evaluated from the relation;

$$n_s = \frac{C_{OX}}{q}(V_{GS} - V_{th}) \tag{5.16}$$

If dislocation scattering is dominant, which depend on n_s and not on the doping rate of La ionized impurity, all four curves should have the same slope and be on the same line, assuming having the same density of dislocations. [145,179] FETs with 0.4 % La-doped BSO layer have smaller μ_{FE} than those with 0.2 % La-doped BSO, an indication that La dopant imposes strong Coulomb scattering centers in our case.

However, the μ_{FE} of FET with a spacer layer is higher than that without a spacer layer in each La doping rate. The continuous control of n_s enables us to figure out the enhanced μ in the modulated structures albeit a small effect. This confirms the difficulty of interpreting the mobility results deduced from Hall measurement in

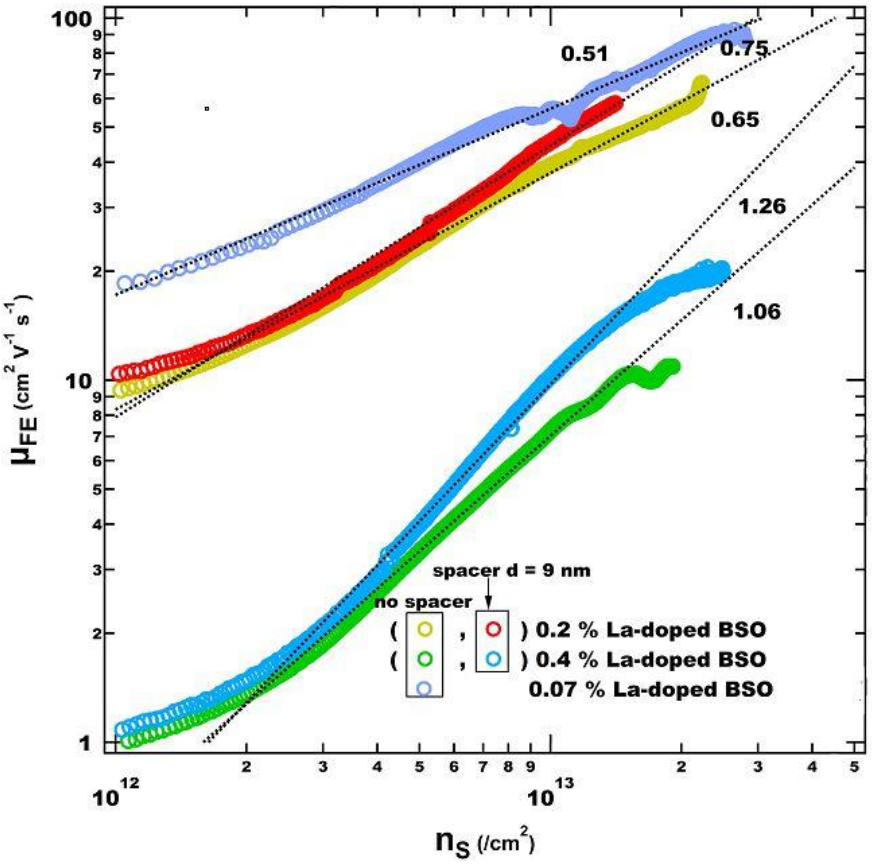

Figure 5.17: μ_{FE} vs. n_s for all FET devices based on LIO/BSO(d=0, 9 nm)/BLSO interface. γ values are written.

Figure 5.10, in which the decrease of μ due to sharp decrease of n_s screens the small enhancement of μ_{FE} by insertion of a spacer layer. Moreover, the distinctive feature between the spacer FET and the no spacer FET is their slope; γ values in the relation of $\mu \propto n_s^{\gamma}$ change from 0.65 to 0.75 for 0.2 % La-doped BSO FET after inserting a spacer layer and from 1.06 to 1.26 for 0.4 % La-doped BSO FET. The larger γ values as increasing *d* are found in GaAs/AlGaAs modulation doped structure, especially, $\mu \propto \frac{n_s^{1.5}}{N_{i,sheet}}$, where $N_{i,sheet}$ is a δ-doped ionized sheet carrier density, in unscreened limit of very large *d*. [130,153,180]

On the other hand, the enhancement of μ_{FE} is small in spite of the 9 nm spacer layer,

the length scale of which is quite larger than $1/k_F$ (k_F: Fermi wavenumber in 2D, $k_F = (2\pi n_s)^{1/2}$) of 1~2 nm in the range of $n_s \cong 10^{13}$ cm^{-2}. This makes μ_{FE} depend more on La doping rate, yielding smaller μ_{FE} for all the spacer FET than 0.07 % La-doped BSO FET. Also the decrease of slope with reducing La doping indicates that there exists upper bound of transport in LIO/BLSO polar interface by other origins for scattering, such as background charged impurities. [129]

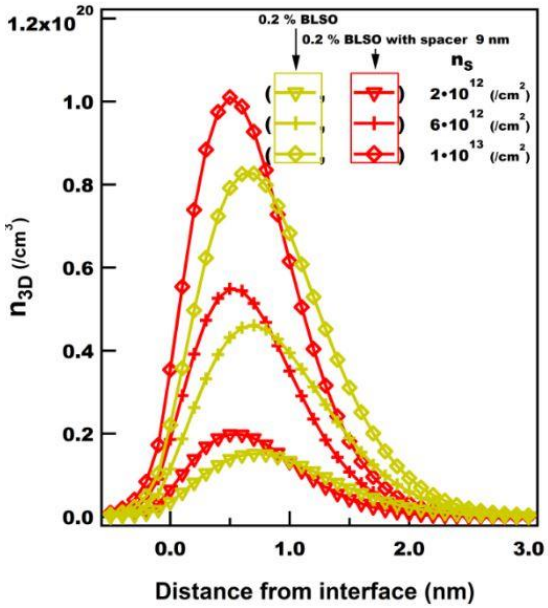

Figure 5.18: Simulation results for n_{3D} distribution as varying the n_s from 2 x 10^{12}/cm^2 to 1 x 10^{13}/cm^2 in the case of with and without modulation doping.

Figure 5.18 illustrate the free carrier distribution at fixed n_s of 2 x 10^{12} cm^{-2}, 6 x 10^{12} cm^{-2} and 1 x 10^{13} cm^{-2}, respectively, in the cases of heterostructures with and without a 9 nm spacer layer at 0.2 % La-doped BSO layer from Snider program. To control n_s, we simulated them by varying the polarization magnitude of LIO (7.85, 8.75, 9.7 μC/cm^2 for no spacer interface and 11.15, 12, 13 μC/cm^2 for spacer interface with LIO 10 nm/BSO (0, 9 nm)/BLSO 12 nm/BSO buffer 110 nm structure), which in turn modifies the band bending of BSO region. The distribution at fixed n_s is

relatively similar between heterostructures with and without a 9 nm spacer layer, while Figure 5.12 (b) shows sharp decrease in n_{3D} from d = 0 to 9 nm.

The enhancement of μ by modulation doping would be significant if only the remote ionized impurity scattering is dominant in transport; the dramatic increase of μ is well reported in GaAs/AlGaAs structures of high crystallinity. [96] However, it is known that unintentional charged background impurities lower μ in 2DEG of GaAs/AlGaAs [129,149] and Si/SiGe [188]. For GaN/AlGaN interface which has a large transport dependence on substrate [142], μ even does not depend on the donor density of the charge supply layer [143,144], indicating the dominant scattering is not due to remote ionized dopant.

BSO has a large density of trap states mainly originating from dislocations, which suggests that further studies as varying the substrate, deposition method, and fabrication process (e.g. in-situ fabrication) will enable much improved mobility in modulation doped LIO/BSO(spacer)/BLSO interface.

5.4.4 Remark on LIO/BSO polar interface

There are several remarks on LIO/BSO polar interface for further improvement of its property.

First, even if the larger conductance of spacer FET than no spacer FET in subthreshold region, in which transport is governed by diffusion current, as shown in transfer characteristics in Figure 5.14 ~5.16, can be explained by parallel conduction in under La-doped layer, σ_s measured by a multimeter between source and drain contact without bias of a gate electrode is somewhat different from Hall measurement result of Figure 5.10. The σ_s from Hall measurement decreases about 2 order of magnitude by inserting spacer layer of d=9 nm, but the measured values of σ_s in the device have yielded similar values between spacer FET and no spacer FET. The

difference of structure using for Hall measurement and FET is the thickness of LIO. It is 10 nm in former case and 244 nm for latter case.

Figure 5.19 (a) shows σ_s from transfer characteristics of each device, that is, V_{DS}/I_{DS} at $V_{GS} = 0$ in the linear region ($V_{DS} = 1$ V). These values are close values by measuring the resistance between source and drain contact without gate bias. Moreover, V_{th} in five FETs are in the range of slight change of I_{DS}, so we can compare σ_s at $V_{GS} = 0$ V with the assumption of similar turn-on behavior. The larger thickness (244 nm) of LIO in FET may induce smaller σ_s and smaller dependence on La doping rate than LIO (10 nm)/BLSO interface. And slight larger σ_s in spacer FET than no spacer FET seems to be related to the parallel conduction of under La-doped layer. While this σ_s is estimated from the boundary of subthreshold region, decrease of σ_s with spacer in Figure 5.10 (c) is related to the drift current by accumulated free carriers in thin layer of 1~2 nm.

The analysis of the subthreshold region in our modulated structure with two parallel conduction channels as well as LIO thickness dependence needs more careful study, but Figure 5.17 given from the transport property in the drift current driven by fully accumulated free carriers is not related this issue when we focusing only enhancement of μ.

Figure 5.19 (b) shows σ_s, n_s, and μ for LIO/BLSO interface as a function of LIO thickness. It seems that polarization of LIO decreases with increasing thickness. The exact mechanism, why its polar nature decreases with thickness, requires further study. The transport property of LIO/BSO interface as varying LIO thickness and BLSO doping rate, detailed atomic structure related to its polar nature, and scattering mechanism inside 2DEG well will help to find out it.

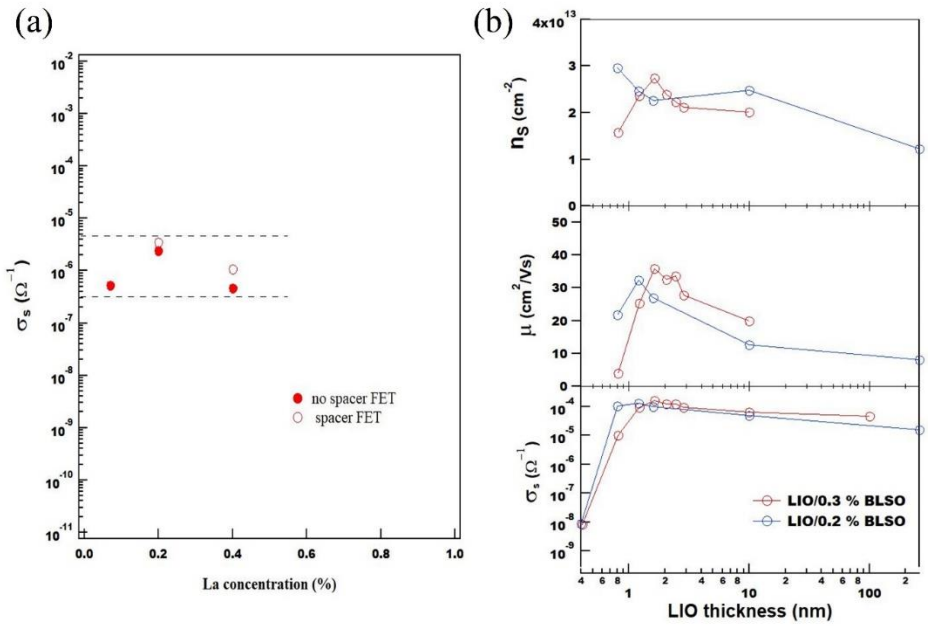

Figure 5.19: (a) σ_s vs. La concentration from FET result.(b) σ_s, n_s, μ as varying LIO thickness.

Second, although availability of modulation doping on LIO/BSO polar interface is found out, the enhancement of μ is small. Doping in large bandgap LIO and control of trap states may be a key to improve μ. At this stage, TDs play a great role on trap states. But charge distribution in TDs core in LIO/BSO polar interface seems to be different from usual TD-limited transport in 2DEG, having $n_s^{3/2}/N_{res}$ dependence in (5.8). In our case, the slope decrease with reduced La doping rate as in Figure 5.17. However, K.Fujiwara et al. [179], reported steeper slope in BSO FET than BLSO FET, implying decrease of slope by La doping. Different tendency of μ $vs. n_s$ calculated as varying filling occupancy of TD-trap state is reported in GaN system [146]. Also, if we treat trapped electrons in TD cores are major background impurities, LIO/BSO/BLSO interface seems to more suffer from it than LIO/BLSO, when comparing μ of spacer FET and no spacer FET (using lower La-doped BSO layer) with (d=9 nm >> well thickness=1~2 nm). This implies different charged background impurity distribution with modulation doping.

Meanwhile, K.Fujiwara et al. [179], reported 300 $cm^2V^{-1}s^{-1}$ of μ at 50 K, as shown Figure 5.20, in undoped BSO FET using electric double layer, enabling high n_s. They used $Sr_{0.5}Ba_{0.5}SnO_3$ buffer layer and annealing at 1200 °C for flat surface. Because the surface quality is very important in 2DEG, though much effort to improve crystalline perfection and purity of films should be done, the study for atomically flat surface is also needed.

Third, the μ in Hall measurement in 5.4.1 is small compared to in FET in 5.4.3 when comparing same n_s. Two reasons may drive it. One is large area in Hall measurement (2×2 mm^2) than in FET (110×140 μm^2), which may induce large defects on it. The other one is probably the existence of charged impurity in LIO. The large polarization of LIO will be depolarized in certain distance by charged impurity. The larger polarization in small thickness of LIO in Figure 5.19 may require high density of charged impurity close to heterointerface to depolarize it. This will reduce μ.

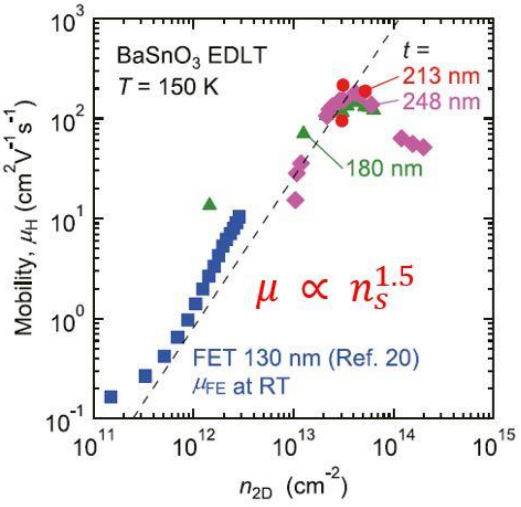

Figure 5.20: Field induced μ_H vs. n_s for BSO EDLT.

Chapter 6

$SrSn_{1-x}Ru_xO_3$ and $BaSn_{1-x}Ru_xO_3$ system (p-type possibility)

While perovskite oxides has a wide variety of physical properties and attracts intensive research in the form of heterojunctions, there are a few p-type semiconductors, making difficult to build p-n junction and CMOS technology in integrated circuits. Because most oxides are intrinsically n-type due to oxygen vacancies and has valence band of filled O 2p orbitals tending to be localized with poor dispersion, there are few examples such as ZnO doped with N [189], Cu_2O [190] and $CuAO_2$ (A: Al, Ga, In) [191-193], etc. On the other hand, perovskite $LaRhO_3$ doped with Sr and Ca and itself is reported to be a p-type semiconductor [194,195], 4d orbital of Rh^{3+} making band-insulting state (band gap of 1.1 eV) with low-spin state by increasing the crystal field splitting energy [196].

$SrRuO_3$ is a ferromagnetic metal with 4 t_{2g} electrons [197], and $SrSnO_3$ and $BaSnO_3$ are band gap insulators with optical gap of about 4.2 eV and 3.1 eV, respectively. In this chapter, $SrSn_{1-x}Ru_xO_3$ and $BaSn_{1-x}Ru_xO_3$ (x: 0.1~0.3) system are studied to find p-type possibility and band structure by Ru substitution. Epitaxially grown films are confirmed by X-ray diffraction and Hall measurement reveals hole carriers, especially, having high mobility of 16.2 cm^2/Vs at 4.98 X 10^{15} cm^{-3} for Ru 12 % substitution for $SrSn_{1-x}Ru_xO_3$. The midgap state by Ru substitution is confirmed by optical transmission spectra and comparison of I-V characteristics of heterojunctions with 0.5 % La-doped BSO (n-type semiconductor) and 1 % La-doped BSO (metal). Lastly, another issue for half metallic state for (x~0.9) and dilute magnetic semiconductor (x~0.3) is introduced.

6.1 $SrSn_{1-x}Ru_xO_3$ (x: 0.1~0.3)

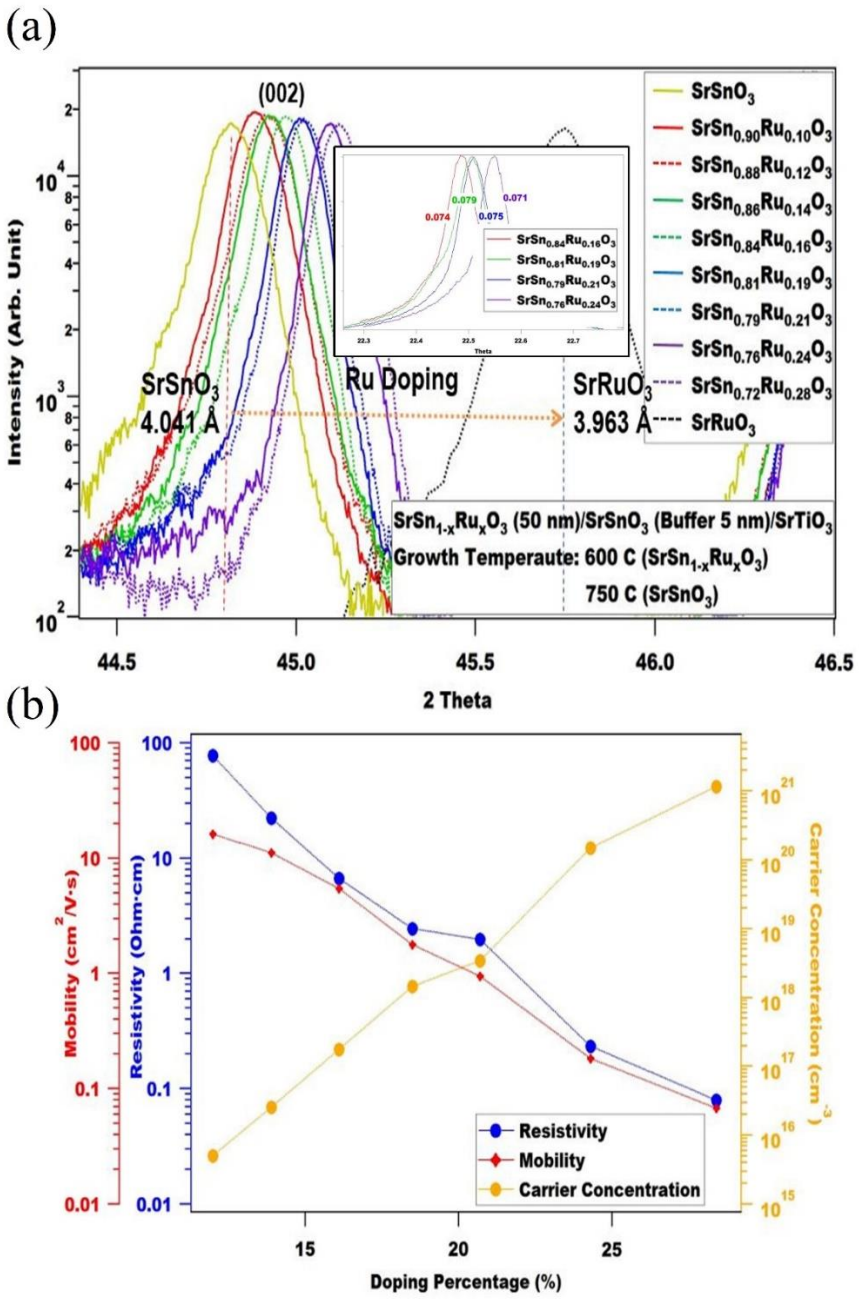

Figure 6.1: Structure and transport properties of $SrSn_{1-x}Ru_xO_3$ (x: 0.1~0.3) (a) $\theta - 2\theta$ scans. (b) Hall measurement result.

$SrSn_{1-x}Ru_xO_3$ (x: 0.1~0.3) (SSRO) films (50 nm) is grown on $SrTiO_3$ substrate with a $SrSnO_3$ buffer layer (5 nm). Ru is comparatively volatile so that the growth temperature of SSRO films is 600 °C lower than that of BSO growth (750 °C).

As confirmed by Figure 6.1 (a), all the films are epitaxially grown with a single phase. Ru substitution makes the out-of plane lattice constant to decrease, so (002) peak moves continually right. Very small value of FWHM about 0.07° indicates high crystallinity of films.

Figure 6.1 (b) illustrates p-type transport data in Hall measurement. As increasing Ru content, the resistivity continually decreases. The mobility decreases and carrier density increases with increasing Ru. It is noteworthy that the highest hole mobility is 16.2 cm^2/Vs, which is high compared to other p-type oxides, usually having values lower than 1 cm^2/Vs [189,192,193].

Because the start of possible measurement range (~12 %) is near the percolation threshold in 3-dimensional system, there exists a question whether Ru clusters contribute to conduction. However, the high crystallinity of films in X-ray diffraction, high hole mobility of 16.2 cm^2/Vs at 4.98 X 10^{15} cm^{-3} for Ru 12 % substitution, and following heterojunction result in chapter 6.2 imply no correlation with percolation. There needs more detailed study to eliminate the percolation issue.

The band structure by Ru substitution is drawn by optical transmittance result in Figure 6.2. $SrSnO_3$, $SrSn_{0.86}Ru_{0.14}O_3$, $SrSn_{0.7}Ru_{0.3}O_3$ grown on $LaAlO_3$ substrate are plotted log (1/transmittance) vs. photon energy. d-d transition (t_{2g}-t_{2g}) at ~1 eV and charge transfer transition (O_{2p}-t_{2g}) at ~3 eV occur by Ru substitution. The linearly extrapolated line about ~4 eV indicates Sn_{5s}-O_{2p} transition. The band structure in the inset, speculated from the optical properties, describes that the gap between spin-down t_{2g} states decreases as increasing bandwidth with increasing Ru content, so that optical absorption at d-d transition and charge transfer transition (O_{2p}-t_{2g}) get being stronger.

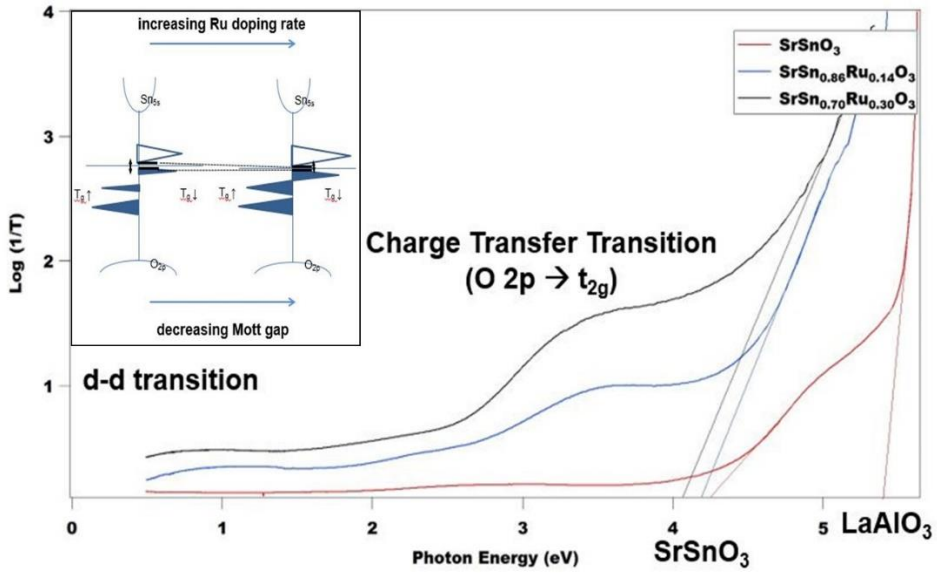

Figure 6.2: Optical properties of $SrSn_{1-x}Ru_xO_3$ (x: 0~0.3). Inset shows an expected band structure by Ru substitution.

6.2 $BaSn_{1-x}Ru_xO_3$ (x: 0.1~0.3)

$BaSn_{1-x}Ru_xO_3$ (x: 0.1~0.3) (BSRO) films (100 nm) is grown on $SrTiO_3$ substrate with a $BaSnO_3$ buffer layer (100 nm). Ru is comparatively volatile so that the growth temperature of BSRO films is 700 °C lower than that of BSO growth (750 °C), however, which is higher than SSRO (600°C) due to more large lattice mismatch between films and substrate.

As confirmed by Figure 6.3 (a), all the films are epitaxially grown with a single phase. Ru substitution makes the out-of plane lattice constant to decrease, so (002) peak of BSRO moves continually right. FWHM is about 0.05 ° ~ 0.1 °.

Figure 6.3 (b) illustrates p-type transport data in Hall measurement. As increasing Ru content, the resistivity continually decreases. The mobility decreases and carrier density increases with increasing Ru. The mobility of BSRO is smaller than SSRO in

the similar carrier concentration region, which is maybe related with high crystallinity of SSRO films and orthorhombic distortion of SSO system.

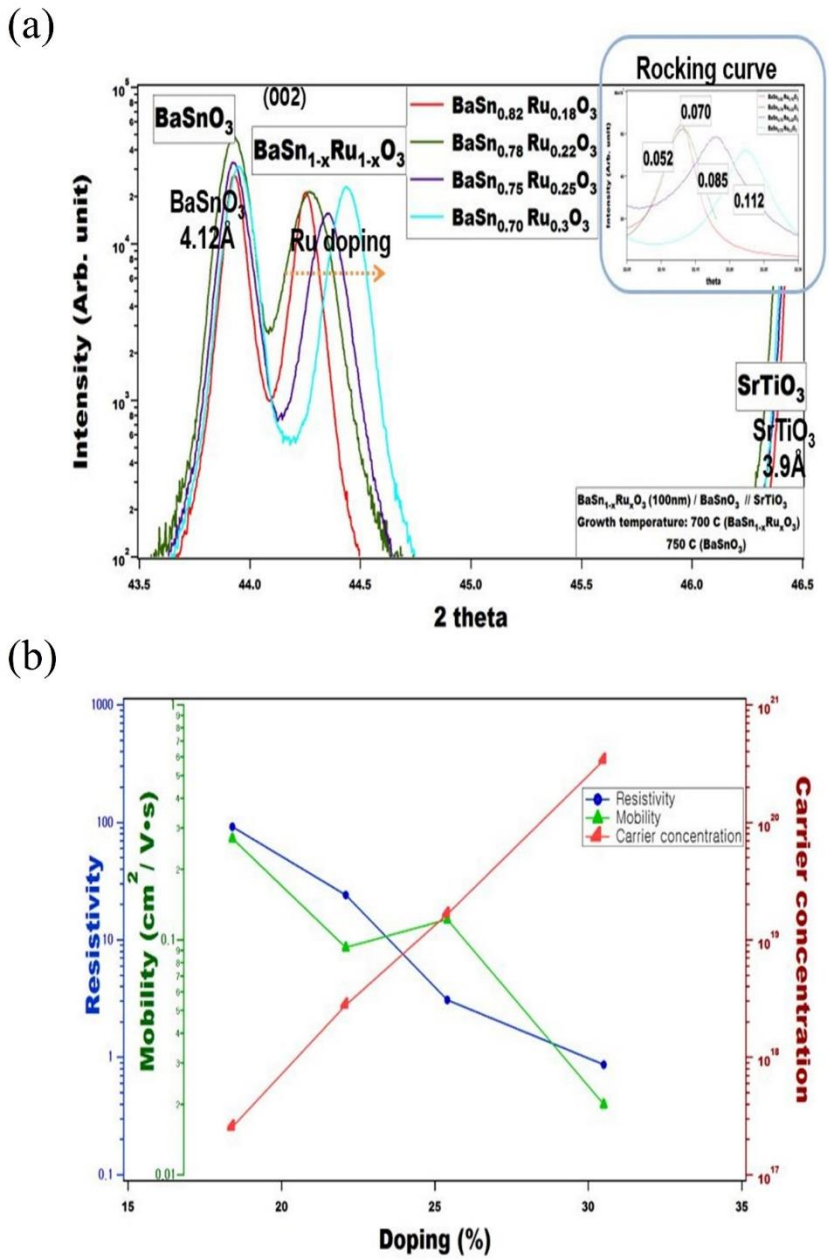

Figure 6.3: Structure and transport properties of $BaSn_{1-x}Ru_xO_3$ (x: 0.1~0.3) (a) $\theta - 2\theta$ scans. (b) Hall measurement result

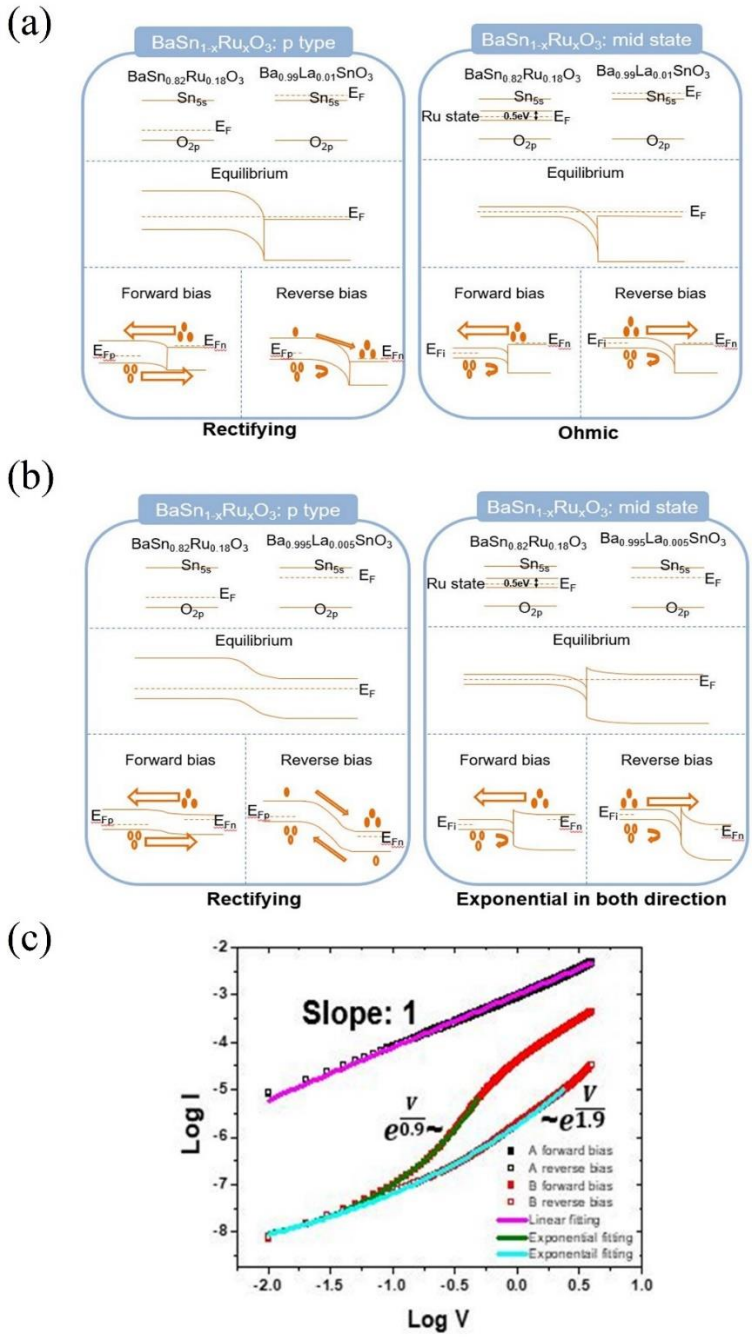

Figure 6.4: Heterojunctions of $BaSn_{0.82}Ru_{0.18}O_3$/(Ba,La)SnO_3. Expected band diagrams of (a) $BaSn_{0.82}Ru_{0.18}O_3$/$Ba_{0.99}La_{0.01}SnO_3$ (junction A) and (b) $BaSn_{0.82}Ru_{0.18}O_3$/$Ba_{0.995}La_{0.005}SnO_3$ (junction B) are shown when BSRO is a p-type band semiconductor and a disorderd correlation insulator (c) I-V characteristics of junction A and B.

To identify the band structure of BSRO, heterojunction devices using $Ba_{0.99}La_{0.01}SnO_3$ as a metal and $Ba_{0.995}La_{0.005}SnO_3$ as a n-type semiconductor were fabricated. Figure 6.4 (a) illustrates the band diagram of $BaSn_{0.82}Ru_{0.18}O_3/Ba_{0.99}La_{0.01}SnO_3$ (junction A) in the two cases, where one is that BSRO is a p-type band semiconductor, Ru substitution only donates hole carriers, the other one is BSRO is a disordered correlation insulator, Ru substitution makes mid-gap states between Sn_{5s}-O_{2p} states and small Ru content makes small bandwidth as opening the gap. The former case is expected to represent a rectifying behavior, but the latter case to show an ohmic behavior.

Figure 6.4 (b) illustrates the band diagram of $BaSn_{0.82}Ru_{0.18}O_3/Ba_{0.995}La_{0.005}SnO_3$ (junction B) in the two cases like the preceding. . The former case is expected to represent a rectifying behavior, but the latter case to show an exponential behavior having a barrier in transport.

The measured I-V characteristics of junction A and B are shown in Figure 6.4 (c). The junction A shows an ohmic behavior and junction B shows an exponential behavior, which agrees with the expectation where Ru substitution makes BSRO as a disordered correlation insulator. The reverse bias for junction B shows more slow increase than forward bias due to higher barrier as described in Figure 6.4 (b). This result agrees with the band structure of SSRO in Figure 6.2.

As a result, Ru substitution in SSO and BSO makes mid-gap states between Sn_{5s} and O_{2p} states and hole carriers arise from opened gap in spin-down t_{2g} states. The best simple idea for making p-type band semiconductor is that electron in valence band (O_{2p}) jumps to acceptor level. However, Co, Y, Nb, K-doped BSO [198-200,67] have high activation energy. The other is a heavy overlap of O_{2p} and d^{10} bands such as cuprates [190-193]. And lastly increasing crystal splitting energy in 4d Rh^{3+} elements can realize the band-insulating state with low-spin state like $LaRhO_3$ [194,195].

Ru substitution in SSO and BSO is another idea making a p-type semiconductor using disordered correlation insulating states. Treating disordered system is difficult but

valuable due to the few cases of p-type perovskite oxide.

6.3 Half metallic state ($SrRu_{1-x}Sn_xO_3$, x~0.1) and dilute magnetic semiconductor ($SrSn_{1-x}Ru_xO_3$, x~0.3)

$SrRu_{1-x}Sn_xO_3$ (x~0.1) (SRSO) films (50 nm) grown on $SrTiO_3$ substrate in reciprocal space mapping in Figure 6.5 (a) indicates epitaxial growth with fully strained in-plane lattice constant.

On the other hand, tetravalent Ru ion has filled t_{2g} majority band and partially filled t_{2g} minority band so that suggest a good candidate for half metallic state [201]. LSDA+U (U_{eff} = 1.0 eV) result for $SrRu_{1-x}Sn_xO_3$ is described in Figure 6.5 (b) and especially $SrRu_{1-x}Sn_xO_3$ (x: 0.5, 0.625) are half metallic states with only spin-down. The half metallic state also can be analogized from resistivity vs. temperature plot in Figure 6.5 (c). Slight Sn substitution in $SrRuO_3$ shows lower resistivity, maybe driven by reduced spin up-spin down repulsion interaction. The exact half metallic range in SRSO films can be different from the calculation result due to parameter size and strain effect, etc. and more direct experiments like magnetic circular dichroism is needed.

The ordered magnetic moments in 3d cation doping at low concentration are unprecedented, and the mechanism of this dilute magnetic semiconductor (DMS) in GaN, TiO_2, SnO_2, ZnO system is like n-type carriers associated with lattice defects play a critical role to mediate the ferromagnetic exchange interaction among magnetic impurities [202]. Figure 6.5 (d) describes magnetic moment vs. temperature for $SrSn_{1-x}Ru_xO_3$ (x: 0.15, 0.3) grown on $LaAlO_3$ substrate by SQUID (superconducting quantum interference device) measurement. Especially, Ru 30 % substitution yield Curie temperature about 140 K, which is similar to $SrRuO_3$. It is deduced that 0.2 μ_B for Ru 30 %. Although the exact evidence for DMS should be figured out and Ru 30 % is near the cation percolation threshold, it is worthwhile to study the magnetic

property of SSRO system by Ru (4d cation) substitution.

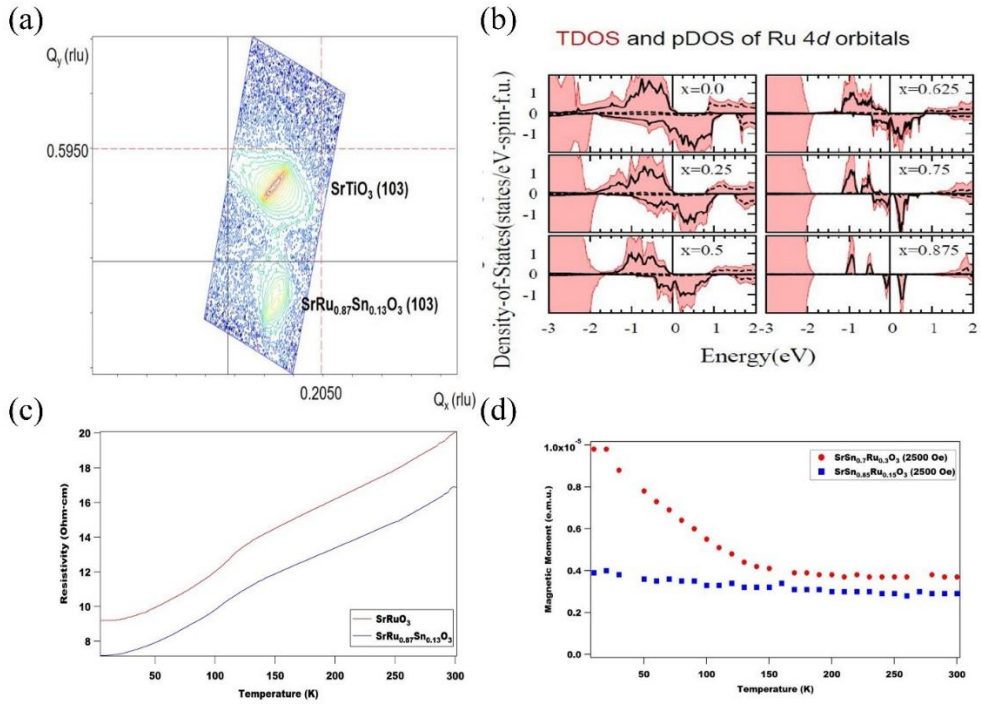

Figure 6.5: (a) RSM of $SrRu_{0.87}Sn_{0.13}O_3$ (50 nm) grown on $SrTiO_3$ substrate. (b) TDOS and pDOS of Ru 4d orbitals in $SrRu_{1-x}Sn_xO_3$. (c) Resistivity vs. temperature for $SrRuO_3$ and $SrRu_{0.87}Sn_{0.13}O_3$. (d) Magnetic moment vs. temperature for $SrSn_{0.85}Ru_{0.15}O_3$ and $SrSn_{0.7}Ru_{0.3}O_3$.

Bibliography

[1] H. J. Kim, U. Kim, H. M. Kim, T. H. Kim, H. S. Mun, B.-G. Jeon, K. T. Hong, W.-J. Lee, C. Ju, K. H. Kim, and K. Char, *Appl. Phys. Express* **5**, 061102 (2012)

[2] H. J. Kim, U. Kim, T. H. Kim, J. Kim, H. M. Kim, B.-G. Jeon, W.-J. Lee, H. S. Mun, K. T. Hong, J. Yu, K. Char, and K. H. Kim, *Phys. Rev. B* **86**, 165205 (2012)

[3] S. Lee, A. Nathan, S. Jeon, and J. Robertson, *Scientic Reports* **5**, 14902 (2015)

[4] Wei-Tsung Chen, Shih-Yi Lo, Shih-Chin Kao, Hsiao-Wen Zan, Chuang-Chuang Tsai, Jian-Hong Lin, Chun-Hsiang Fang, and Chung-Chun Lee, *IEEE. Elec. Dev. Lett*. **32**, 1552 (2011)

[5] D. S. Ginley and C. Bright, *MRS Bull.* **25** (8), 15 (2000)

[6] C. Park, U. Kim, C. J. Ju, J. S. Park, Y. M. Kim, and K. Char, *Appl. Phys. Lett.* **105**, 203503 (2014)

[7] U. Kim, C. Park, T. Ha, Y. M. Kim, N. Kim, C. Ju, J. Park, J. Yu, J. H. Kim, and K. Char, *APL Mater*. **3**, 036101 (2015)

[8] Y. M. Kim, C. Park, U. Kim, C. Ju, and K. Char, *Appl. Phys. Express* **9**, 011201 (2016)

[9] Y. M. Kim, C. Park, T. Ha, U. Kim, N. Kim, J. Shin, Y. Kim, J. Yu, J. H. Kim, and K. Char, *APL Mater*. **5**, 016104 (2017)

[10] P. G. Neudeck, R. S. Okojie, and L.-Y. Chen, *Proceedings of the IEEE*. **90**, 1065 (2002)

[11] R. J. Trew, *Proceedings of the IEEE*, **90**, 1032 (2002)

[12] C. Sintamarean, E. Eni, F. Blaabjerg, R. Teodorescu, and H. Wang, *Proceedings of Int. Power Electron. Conf.*, 1912 (2014)

[13] D. Toyota, I. Ohkubo, H. Kumigashira, M. Oshima, T. Ohnishi, M. Lippmaa, M. Kawasaki, and H. Koinuma, *J. Appl. Phys* **99**, 08N505 (2006)

[14] Kenji Uchino, *Sci. Technol. Adv. Mater*. **16**, 046001 (2015)

[15] R. E. Cohen, *Nature* **358**, 136–138 (1992)

[16] X. Wang, Y. Chai, L. Zhou, H. Cao, C. Cruz, J. Yang, J. Dai, Y. Yin, Z. Yuan, S. Zhang, R. Yu, M. Azuma, Y. Shimakawa, H. Zhang, S. Dong, Y. Sun, C. Jin, and Y. Long, *Phys. Rev. Lett.* **115**, 087601 (2015)

[17] N. Reyren, S. Thiel, A. D. Caviglia, L. Fitting Kourkoutis, G. Hammerl, C. Richter, C. W. Schneider, T. Kopp, A.-S. Ruetschi, D. Jaccard, M. Gabay, D. A. Muller, J. –M. Triscone, and J. Mannhart, *Science* **317**, 1196 (2007)

[18] U. Kim, C. Park, T. Ha, R. Kim, H. S. Mun, H. M. Kim, H. J. Kim, T. H. Kim, N. Kim, J. Yu, K. H. Kim, J. H. Kim, and K. Char, *APL Mater*. **2**, 056107 (2014)

[19] S. Upadhyay, O.Parkash, and D. Kumar. *Journal of Materials Science: Materials in Electronics* **12**,165–172 (2001)

[20] O. Parkash, D. Kumar, K. K. Srivastav, and R. K. Dwivedi, *Journal of Materials Science* **36**, 5805 (2001)

[21] A. Kumar, B. P. Singh, R. N. P Choudhary, and A. K. Thakur, *Materials Letters* **59**, 1880 (2005)

[22] A. Kumar and R. N. P. Choudhary, *Journal of Materials Science* **42**, 2476 (2007)

[23] Q. Liu, Y. He, H. Li, B. Li, G. Gao, Lele Fan, and Jianming Dai, *Appl. Phys.Express*, **7**,0 (2014)

[24] P. V. Wadekar, J. Alaria, M. O'Sullivan, N. L. O. Flack, T. D. Manning, L. J. Phillips, K. Durose, O. Lozano, S. Lucas, J. B. Claridge, and M. J. Rosseinsky, *Appl. Phys. Lett*. **105**, 052104 (2014)

[25] S. Raghavan,T. Schumann, H. Kim, J.Y. Zhang, T. A. Cain, and S. Stemmer, *APL Mater*. **4**, 016106 (2016)

[26] W.-J. Lee,1,H. J. Kim, E. Sohn,T. H. Kim, J.-Y. Park, W. Park, H. Jeong, T. Lee,

J. H. Kim, K.-Y. Choi, and K. H. Kim, *Appl. Phys. Lett.* **108**, 082105 (2016)

[27] Qinzhuang Liu, Jianjun Liu, Bing Li, Hong Li, Guangping Zhu, Kai Dai, Zhongliang Liu, Peng Zhang, and Jianming Dai, *Appl. Phys. Lett*. 101, 241901 (2012)

[28] M. Hussein, N. Assadi, and D. A. H. Hanaor, *J. Appl. Phys*. **113**, 233913 (2013).

[29] S. S. Shin, E. J. Yeom, W. S. Yang, S. Hur, M. G. Kim, J. Im, J. Seo, J. H. Noh, S. Seok, *Science* **356**, 167-171 (2017)

[30] A. Muthukumar, G. Rey, G. Giusti, V. Consonni, E. Appert, H. Roussel, A. Dakshnamoorthy, and D. Bellet, *AIP Conference Proceedings* **1512**, 710 (2013)

[31] S. H. Lee, S. H. Han, H. S. Jung, H. Shin, J. Lee, J. H. Noh, S. Lee, I. S. Cho, J. K. Lee, J. Kim, and H. Shin, *J. Phys. Chem. C* **114**, 7185–7189 (2010)

[32] K. K. Teshima, Y. Shirai, T. Miyasaka, *J. Am. Chem. Soc.* **131**, 6050–6051, (2009)

[33] M. M. Lee, J. Teuscher, T. Miyasaka, T. N. Murakami, H. J. Snaith, *Science* **338**, 643–647 (2012)

[34] B. Ostrick, M. Fleischer, and H. Meixner. *Journal of the American Ceramic Society* **80**, 2153–2156 (1997)

[35] P. Nunes, E. Fortunato, and R. Martins, *Thin Solid Films* **383,** 277 (2001)

[36] D. B. Schwarz, *J. Electrochem. Soc.* **122**, 707 (1975).

[37] K. N. Tu, N. C. Yeh, S. I. Park, and C. C. Tsuei, *Phys. Rev. B* **39,** 304 (1989)

[38] L. Malavasi and G. Flor, *J. Phys. Chem. B* **107**, 13880 (2003)

[39] R. A. Bucur, A. I. Bucur, S. Novaconi, and I. Nicoara, *Journal of Alloys and Compounds* **542**,142–146 (2012)

[40] K. Ploog, A. Fischer, and H. Kunzel, *J. Electrochem. Soc* **128**, 400 (1981)

[41] E. Kyle , S. Kaun , P. Burke , F. Wu , Y. Wu , and J. Speck , *J. Appl. Phys.* **115**, 193702 (2014).

[42] S. Smirnov, Ph. D. thesis, Vienna university of technology (2003)

[43] K. Ellmer, *Nature Photon.* **6**, 809 (2012).

[44] J. Son, P. Moetakef, B. Jalan, O. Bierwagen, N. J. Wright, R. E.-H., and S. Stemmer, *Nat. Mater.* **9**, 482 (2010).

[45] S. Ohta, T. Nomura, H. Ohta, and K. Koumoto, *J. Appl. Phys.* **97**, 034106 (2005).

[46] D. K. Gaskill, A. E. Wickenden, K. Doverspike, B. Tadayon, and L. B. Rowland, *J. Electron. Mater.* **24**, 1525 (1995)

[47] R. L. Weiher, *J. Appl. Phys.* **33**, 2834 (1962)

[48] H. Toyosaki, M. Kawasaki, and Y. Tokura, *Appl. Phys. Lett.* **93**, 132109 (2008)

[49] A. Ohtomo, K. Tamura, K. Saikusa, K. Takahashi, T. Makino, Y. Segawa, H. Koinuma, and M. Kawasaki, *Appl. Phys. Lett.* **75**, 2635 (1999)

[50] R. F. Pierret, Semiconductor Device Fundamentals (Addison-Wesley,Reading, MA, 1996).

[51] E. Moreira, J. M. Henriques, D. L. Azevedo, E. W. S. Caetano, V. N. Freire, and E. L. Albuquerque, *J. Solid State Chem.* **187**, 186 (2012)

[52] S. Adachi, *J. Appl.Phys.* **58**, 3 (1985)

[53] A. M. Witowski, K. Pakua, J. M. Baranowski, M. L. Sadowski, and P. Wyder. *Appl. Phys. Lett.* **75**, 4154 (1999)

[54] D. M. Riffe, *Journal of the Optical Society of America B* **19**, 1092 (2002)

[55] M. Oshikiri, Y. Imanaka, F. Aryasetiawan, and G. Kido, *Physica B: Condensed Matter* **298**, 472 (2001)

[56] N. Preissler, O. Bierwagen, A. T. Ramu, and J. S. Speck. *Phys. Rev. B - Condensed Matter and Materials Physics* **88**, 1 (2013)

[57] H. Wang, X. Jiao, Q. Liu, X. Xuan, F. Chen, and W. Wu, *J. Phys. D: Appl. Phys.*

43, 035403 (2010)

[58] B. Hadjarab, A. Bouguelia, and M. Trari, *J. Phys. Chem. Solids* **68**, 1491 (2007)

[59] E. H. Mountstevens, S. A. T. Redfern, and J. P. Attfield. *Phys. Rev. B - Condensed Matter and Materials Physics* **71**, 2 (2005)

[60] P. Singh, B. J. Brandenburg, C. P. Sebastian, P. Singh, S. Singh, D. Kumar, and O. Parkash, *Jpn. J. Appl. Phys.* **47**, 3540 (2008)

[61] K. Iniewski, CMOS Processors and Memories (Springer, New York, 2010)

[62] M. Trassin, *J. Phys.: Condens. Matter* **28,** 033001 (2016)

[63] J. W. Judy, *Smart Mater. Struct*. **10**, 1115 (2001)

[64] J. M. Tour and T. He, *Nature* **453**, 42 (2008)

[65] S. H. Baek, J. Park, D. M. Kim, V. A. Aksyuk, R. R. Das, S. D. Bu, D. A. Felker, J. Lettieri, V. Vaithyanathan, S. S. N. Bharadwaja, N. Bassiri-Gharb, Y. B. Chen, H. P. Sun, C. M. Folkman, H. W. Jang, D. J. Kreft, S. K. Streiffer, R. Ramesh, X. Q. Pan, S. Trolier-McKinstry, D. G. Schlom, M. S. Rzchowski, R. H. Blick, and C. B. Eom, *Science* **334**, 958 (2011).

[66] J. –S. Lee, and S. –K. Joo, *Appl. Phys. Lett.* **81**, 2602 (2002);

[67] H. M. Kim, U. Kim, C. Park, H. Kwon, and K. Char, *APL Mater.* **4**, 056105 (2016)

[68] H. Mun, U. Kim, H. M. Kim, C. Park, T. H. Kim, H. J. Kim, K. H. Kim, and K. Char, *Appl. Phys. Lett*. **102**, 252105 (2013)

[69] H. M. Ng, D. Doppalapudi, T. D. Moustakas, N. G. Weimann, and L. F. Eastman, *Appl. Phys. Lett*. **73**, 821 (1998)

[70]. Y. A. Osip'yan and S. A. Shevchenko, *Sov. Phys.-JETP* **38**, 345 (1974)

[71] N. G. Weimann, L. F. Eastman, D. Doppalapudi, H. M. Ng, and T. D. Moustakas,

J. Appl. Phys. **83**, 3656 (1998)

[72] T. Hino, S. Tomiya, T. Miyajima, K. Yanashima, S. Hashimoto, and M. Ikeda, *Appl. Phys. Lett.* **76**, 3421 (2000)

[73] K. Ueno, I. H. Inoue, T. Yamada, H. Akoh, Y. Tokura, and H. Takagi, *Appl. Phys. Lett.* **84**, 3726 (2004)

[74] K. Ueno, I. H. Inoue, H. Akoh, M. Kawasaki, Y. Tokura, and H. Takagi. *Appl. Phys. Lett.* **83**, 1755 (2003)

[75] K. Shibuya, T. Ohnishi, T. Uozumi, T. Sato, M. Lippmaa, M. Kawasaki, K. Nakajima, T. Chikyow, and H. Koinuma. *Appl. Phys. Lett.* **88**, 212116 (2006)

[76] K. Fujiwara, K. Nishihara, J. Shiogai, and A. Tsukazaki, *AIP Advances* **6**, 085014 (2016);

[77] S. Sallis, D. O. Scanlon, S. C. Chae, N. F. Quackenbush, D. A. Fischer, J. C. Woicik, J.-H. Guo, S. W. Cheong, and L. F. J. Piper, *Appl. Phys. Lett.* **103**, 042105 (2013);

[78] H. F. Wang, Q. Z. Liu, F. Chen, G. Y. Gao, Wenbin Wu, and X. H. Chen, *J. Appl. Phys.* **101**, 106105 (2007);

[79] P. R. Willmott and J. R. Huber, *Rev. Mod. Phys.* **72**, 315 (2000)

[80] D. M. Roessler and W. C. Walker, *Phys. Rev.* **159**, 733 (1967)

[81] J. Nowotny, Science of Ceramic interface II (Elsevier Science Publisher B. V., Amsterdam, The Netherlands, 1994) p. 349

[82] W. –C. Chen, C. –Y. Peng, and L. Chang, *Nanoscale Research Letters* **9**, 551 (2014)

[83] W. –J. Lee, H. J. Kim, E. Sohn, H. M. Kim, T. H. Kim, K. Char, J. H. Kim, and K. H. Kim, *Phys. Status Solidi A* **212**, 1487 (2015)

[84] J. Als-Nielsen and D. McMorrow, Elements of Modern X-ray Physics (John Wiley & Sons, Ltd., New York. 2001)

[85] D. Schick, A. Bojahr, M. Herzog, P. Gaal, I. Vrejoiu, and M. Bargheer, *Phys. Rev. Lett* **110**, 095502 (2013)

[86] . J. Park, U. Kim, and K. Char, *Appl. Phys. Lett.* **108**, 092106 (2016).

[87] T. Maekawa, K. Kurosaki, and S. Yamanaka, *J. Alloys Compd.* **407**, 44 (2006).

[88] . M. S. Tyagi, *Phys. Stat. Sol.* (a) **30**, 609 (1975)

[89] M. B. Das, *Solid State Electronics* **12**, 305 (1969)

[90] B. Li, Q. Liu, Y. Zhang, Z. Liu, L. Geng, *J. Alloy and Compounds* **680**, 343 (2016)

[91] Q. Liu, F. Jin, G. Gao, B. Li, Y. Zhang, Q. Liu, *J. Alloy and Compounds* **684**, 125-131 (2016)

[92] K. Ganguly, P. Ambwani, P. Xu, J. S. Jeong, K. A. Mkhoyan, C. Leighton, and B. Jalan, *APL Materials* **3**, 062509 (2015);

[93] R. L. Anderson, *IBM J. Res. and Develop* **4**, 283 (1960)

[94] L. Esaki and R. Tsu, *IBM Res., Internal Rep. RC 2418* (1969)

[95] R. Dingle, H. L. Stormer, A. C. Gossard, and W. Wiegmann, *Appl. Phys. Lett*., **33**, 665 (1978)

[96] D. G. Schlom, and L. N. Pfeier, *Nature materials* **9**, 881 (2010)

[97] Angus Rockett, The Materials Science of Semiconductors (Springer, 2008)

[98] O. Fursenko, J. Bauer, G. Lupina, P. Dudek, M. Lukosius, C. Wenger, and P. Zaumseil, *Thin Solid Films* **520**, 4532 (2012)

[99] G. Lupina, O. Seifarth, P. Dudek, G. Kozlowski, J. Dabrowski, H.-J. Thieme, G. Lippert, T. Schroeder, and H.-J. Müssig, *Physica Status Solidi (B) Basic Research* **248**, 323 (2011)

[100] H. Mizoguchi, H. W. Eng, and P. M. Woodward, *Inorganic Chemistry* **43**, 1667 (2004)

[101] . E. Baba, D. Kan, Y. Yamada, M. Haruta, H. Kurata, Y. Kanemitsu, and Y. Shimakawa, J. Phys. D: Appl. Phys. **48**, 455106 (2015)

[102]. Q. Liu, B. Li, J. Liu, H. Li, Z. Liu, K. Dai, G. Zhu, P. Zhang, F. Chen, and J. Dai, *EPL* **98**, 47010 (2012)

[103] G. Kresse and J. Furthmuller, *Phys. Rev. B* **54**, 11169 (1996)

[104] N. Charles and J. M. Rondinelli, *Phys. Rev. B* **94**, 174108 (2016)

[105] L. Abbes and H. Noura, *Results in Physics* **5**, 38 (2015)

[106] H.-R. Liu, J.-H. Yang, H. J. Xiang, X. G. Gong, and S.-H. Wei, *Appl. Phys. Lett.* **102**, 112109 (2013)

[107] L. Vegard, Z. *Phys.* **5**, 17 (1921)

[108] Y. Zhang, M. P. K. Sahooabc, and J. Wang, *Phys. Chem. Chem. Phys.* **19**, 7032 (2017)

[109] A. Bouhemadu, F. Djabi, and R. Khenata, *Phys. Lett. A* **372**, 4257 (2008)

[110] J. Tauc, R. Grigorovici, and A. Bancu, *Phys. Stat. Sol.* **15**, 627 (1966)

[111] C. Franchini, *J. Phys. : Condens. Matter* **26**, 253202 (2014)

[112]. J. Wu, W. Walukiewicz, K. M. Yu, J. W. Ager III, S. X. Li, E. E. Haller, H. Lu, and W. J. Schaff, *Solid State Communications* **127**, 411 (2003)

[113] Z. M. Wang, MoS_2: Materials, Physics, and Devices (Springer, Switzerland, 2014)

[114] T. Schumann, S. Raghavan, K. Ahadi, H. Kim, and S. Stemmer, *J. Vac. Sci. Technol. A* **34**, 050601 (2016)

[115] H.-L. Shi1, and Y. Duan, *Eur. Phys. J. B* **66**, 439–444 (2008)

[116] C. A. Francis, D. M. Detert, G. Chen, O. D. Dubon, K. M. Yu, and W. Walukiewicz, *Appl. Phys. Lett.* **106**, 022110 (2015)

[117] B. Wei, K. Zheng, Y. Ji, Y. Zhang, Z. Zhang, and X. Han, *Nano Lett.* **12**, 4595 (2012)

[118] K. Kim, G. L. W. Hart, and A. Zunger, *Appl. Phys. Lett.* **80**, 3105 (2002)

[119] D. C. Look, D. K. Lorance, J. R. Sizelove, C. E. Stutz, K. R. Evans, and D. W. Whitsonl, *J. Appl. Phys.* **71**, 260 (1992)

[120] J. Shin, Y. M. Kim, Y. Kim, C. Park, and K. Char, *Appl. Phys. Lett*. **109**, 262102 (2016)

[121] U. Kim, C. Park, Y. M. Kim, J. Shin, and K. Char, *APL Mater*. **4**, 071102 (2016)

[122] J. P. Ibbetson, P. T. Fini, K. D. Ness, S. P. DenBaars, J. S. Speck, and U. K. Mishra, *Appl. Phys. Lett*. **77**, 250 (2000)

[123] T. Ando, A. B. Fowler, and F. Stern, *Rev. Mod. Phys*. **54**, 437 (1982)

[124] Shin-ichi Takagi, ***Member,*** *IEEE*, Akira Toriumi, Masao Iwase, and Hiroyuki Tango, IEEE TRANSACTIONS ON ELECTRON DEVICES, VOL. **41,** NO. **12, 2357,** DECEMBER 1994

[125] Grove, A. S., Physics and Technology of Semiconductor Devices (Wiley, New York, 1967).

[126] Sze, S. M, Physics of Semiconductor Devices (Wiley, New York, 1969)

[127] N. E. H., and J. R. Brews, MOS Physics and Technology (Wiley, New York, 1982).

[128] S. Hiyamizu, T. Mimura, T. Fujii, K. Nanbu, and H. Hashimoto, *Jpn. J. Appl. Phys.* **20**, L245 (1981)

[129] E. H. Hwang and S. D. Sarma, *Phys. Rev. B* **77**, 235437 (2008)

[130] S. Das Sarma, E. H. Hwang, S. Kodiyalam, L. N. Pfeiffer, and K. W. West, *Phys. Rev. B* **91**, 205304 (2015)

[131] D. C. Tsui, H. L. Stormer, and A. C. Gossard, *Phys. Rev. Lett.* **48**, 1599 (1982)

[132] K Buth and U. Merkt, *Annalen der Physik* **11**(12), 843 (2002)

[133] S. Nakamura, T. Mukai, and M. Senoh, *Appl. Phys. Lett*. **64**, 1687 (1994)

[134] B. S. Eller, J. Yang, and R. J. Nemanich, *J. Vac. Sci. Technol. A* **31**, 050807 (2013)

[135] M. J. Manfra, K. W. Baldwin, A. M. Sergent, K. W. West, R. J. Molnar, and J. Caissie, *Appl. Phys. Lett*. **85**, 5394 (2004)

[136] S. Karmalkar D. M. Sathaiya, and M. S. Shur, *Appl. Phys. Lett*. **82**, 3976 (2003).

[137] Z. H. Liu, G. I. Ng, S. Arulkumaran, Y. K. T. Maung, and H. Zhou, *Appl. Phys. Lett.* **98**, 163501 (2011).

[138] E. Arslan, S. Altindal, S. Ozcelik, and E. Ozbay, *J. Appl. Phys.* **105**, 023705 (2009).

[139]S. Hoshi, T. Marui, M. Itoh, Y. Sano, and S. Seki, *IEICE Trans Electron.* ***E89C***, 1052 (2006).

[140] V. P. Pyara, R. Singh, A. K. Saxena, C. Patvardhan, D. P. Prasad, and D. B. Das, Proceedings of the National Seminar on Applied Systems Engineering and Soft Computing (Allied Publishers, India, 2000) p. 578

[141] Nouacry, Touhami, Benkassou, Bouziane, and Aouaj, *J. Elect. Electron Syst.* **5**, 1000169 (2016)

[142] R. Gaska, M. S. Shur, A. D. Bykhovski, A. O. Oriov, and G. L. Snider, *Appl. Phys. Lett.* **74**, 287 (1999)

[143] M. Marso, J. Bernat, P. Javorka, and P. Kordos, *Appl. Phys. Lett.* **84**, 2928 (2004)

[144] M. Marso, J. Bernát, P. Javorka, A. Fox, and P. Kordoš, *Phys. Stat. Sol. (c)* **2**, No. 7, 2611, (2005)

[145] M. J. Manfra, L. N. Pfeiffer, K. W. West, H. L. Stormer, K. W. Baldwin, J. W. P. Hsu, D. V. Lang, and R. J. Molnar Citation: *Appl. Phys. Lett.* **77**, 2888 (2000);

[146] F Carosella1 and J-L Farvacque, *J. Phys.: Condens. Matter* **20**,325210 (2008)

[147] D. Zanato, S. Gokden, N. Balkan, B. K. Ridley and W. Schaff, Semicond. *Sci. Technol.* **19**,427 (2004)

[148] J. H. Davies, The physics of low-dimensional semiconductors (Cambridge University Press, USA, 1998)

[149] W. Walukiewicz, H. E. Ruda, J. Lagowski, and H. C. Gatos, *Phys. Rev. B* **30**, 4571 (1984)

[150] D. Jena, Charge Transport in Semiconductors, University of Nortre Dame (2004)

[151] F. F.Fang, and W.E.Howard, *Phys.Rev.Lett.***16**, 797 (1996)

[152] D. Jena, A. C. Gossard, and U. K. Mishra, *Appl. Phys. Lett*. **76**, 1707 (2000)

[153] T. Ando, *J. Phys. Soc. Jpn.* **51**, 3900 (1982)

[154] D. Jena, Y. Smorchkova, C. Elsass, A. C. Gossard, and U. K. Mishra, arXiv:cond-mat/0103461v1 [cond-mat.mtrl-sci] (2001)

[155] J.-L. Farvacque1 and Z. Bougrioua, *Phys. Rev. B* **68**, 035335 (2003)

[156] D. K. Ferry and S. M. Goodnick, Transport in Nanostructures (Cambridge University Press, USA, 1997)

[157] O. Ambacher, J. Smart, J. R. Shealy, N. G. Weimann, K. Chu, M. Murphy, W. J. Schaff, and L. F. Eastman, *J. Appl. Phys*. **85**, 3222 (1999)

[158] M. J. Manfra, N. G. Weimann, J. W P Hsu, L. N. Pfei_er, K. W. West, S. Syed,

H. L. Stormer, W. Pan, D. V. Lang, S. N G Chu, G. Kowach, a. M. Sergent, J. Caissie, K. M. Molvar, L. J. Mahoney, and R. J. Molnar, *J. Appl. Phys*. **92**, 338 (2002)

[159] H. Tampo, H. Shibata, K. Matsubara, A. Yamada, P. Fons, and S. Niki, *Appl. Phys. Lett*. **89,** 132113 (2006)

[160] A. Tsukazaki, S. Akasaka, K. Nakahara, Y. Ohno, H. Ohno, D. Maryenko, A. Ohtomo, and M. Kawasaki, *Nature Mat*. **9**, 889 (2010)

[161] A. Ohtomo and H. Y. Hwang, *Nature* **427**, 423 (2004)

[162] N. Reyren, S. Thiel, D. Caviglia, L. F. Kourkoutis, G. Hammerl, C. Richter, C. W. Schneider, T. Kopp, S. Ruetschi, D. Jaccard, M. Gabay, D. Muller, J.-M. Triscone, ,and J. Mannhart, *Science* **317**, 1196 (2007)

[163] A. Brinkman, M. Huijben, M. van Zalk, J. Huijben, U. Zeitler, J. C. Maan, W. G. van der Wiel, G. Rijnders, D. H. Blank, and H. Hilgenkamp. *Nature materials* **6**, 493 (2007)

[164] Z. Q. Liu, C. J. Li, W. M. Lu, X. H. Huang, Z. Huang, S.W. Zeng, X. P. Qiu, L. S. Huang, A. Annadi, J. S. Chen, J. M. D. Coey, T. Venkatesan, and Ariando, *Phys. Rev. X* **3**, 021010 (2013)

[165] L. Yu and A. Zunger, *Nat. Comm*. **5**, 5518 (2014)

[166] G. Herranz, M. Basletic, M. Bibes, C. Carretero, E. Tafra, E. Jacquet, K. Bouzehouane, C. Deranlot, Hamzic, J.-M. Broto, A. Barthélémy, and A. Fert, *Phys. Rev. Lett.* **98**, 216803 (2007).

[167] A. Kalabukhov, Y. A. Boikov, I. T. Serenkov, V. I. Sakharov, J. Borjesson, N. Ljustina, E. Olsson, D. Winkler, and T. Claeson, *EPL* (Europhysics Lett.) **93**, 37001 (2011).

[168] A. Ohtomo and H. Y. Hwang, *J. Appl. Phys.* **102**, 083704 (2007).

[169] N. Nakagawa, H. Y. Hwang, and D. A. Muller*, Nature materials* **5**, 204 (2006).

[170] E. Slooten, Zhicheng Zhong, H. Molegraaf, P. Eerkes, S. de Jong, F. Massee, E. van Heumen, M. Kruize, S. Wenderich, J. Kleibeuker, M. Gorgoi, H. Hilgenkamp, A. Brinkman, M. Huijben, G. Rijnders, D. Blank, G. Koster, P. Kelly, and M. Golden. *Phys. Rev. B* **87**, 085128 (2013)

[171] W. Siemons, G. Koster, H. Yamamoto, W. Harrison, G. Lucovsky, T. Geballe, D. Blank, and M. Beasley, *Phys. Rev. Lett*. **98**, 196802 (2007)

[172] S. W. Lee, Y. Liu, J. Heo, and R. G. Gordon, *Nano letters*, **12**, 4775 (2012)

[173] Y. Chen, N. Pryds, J. E. Kleibeuker, G. Koster, J. Sun, E. Stamate, B. Shen, G. Rijnders, and S. Linderoth. *Nano letters* **11**, 3774 (2011)

[174] G. Herranz, M. Basletic, M. Bibes, R. Ranchal, A. Hamzic, E. Tafra, K. Bouzehouane, E. Jacquet, J. P. Contour, *Phys. Rev. B* **73**, 064403 (2006)

[175] J. J. Harris, C. T. Foxon, D. E. Lacklison, and K. W. J. Barnham, *Superlattices and Microstructures* **2**, 563 (1986)

[176] J. V. DiLorenzo, R. Dingle, M. Feuer, A. C. Gossard, R. Hendel, J. C. M. Hwang, A. Kastalsky, V. G. Keramidas, R. A. Kiehl, and P. O'Connor, *IEDM Tech. Dig.* **25**, 578 (1982)

[177] D. Delageveaudeuf and N. T. Linh, *IEEE Trans. Electron. Dev.*, **ED-29**, 955 (1982)

[178] T. Saju, Y. Hirayama, and Y. Horikoshi, *Jpn. J. Appl. Phys*. **30**, 902 (1991)

[179] K. Fujiwara, K. Nishihara, J. Shiogai, and A.Tsukazaki, *Appl. Phys. Lett.* **110**, 203503 (2017)

[180] K. Hirakawa and H. Sakaki, *Phys. Rev. B* **33**, 8291 (1986)

[181] I-H. Tan, G. L. Snider, L. D. Chang, and E. L. Hu, *J. Appl. Phys.* **68**, 4071 (1990)

[182] 1D Poisson-Schrodinger solver program developed by Dr. Gregory Snider, http://www3.nd.edu/～gsnider/.

[183] A. V. Sanchela, T. Onozato, B. Feng, Y. Ikuhara, and H. Ohta, *Phys. Rev. Materials* **1**, 034603 (2017)

[184] Y. Tsividis and C. McAndrew, Operation and modeling of the MOS Transistor (Oxford University Press., New York, 2011)

[185] H. Marien, M. Steyaert, and P. Heremans, Analog Organic Electronics (Springer Science, New York, 2013)

[186] S. Lee and A. Nathan, *Scientific Reports* **6**, 22567 (2016)

[187] E. F. Schubert, K. Ploog, H. Dambkes, and K. Heime, *Appl. Phys. A* **3**3, 63 (1984)

[188] X. Mi, T. M. Hazard, C. Payette, K. Wang, D. M. Zajac, J. V. Cady, and J. R. Petta, *Phys. Rev. B* **92**, 035304 (2015)

[189] M. Joseph, H. Tabata, and T. Kawai, *Jpn. J. Appl. Phys.* **38**, L1205 (1999)

[190] H. Raebiger, S. Lany, and A. Zunger, *Phys. Rev. B* **76**, 045209 (2007)

[191] H. Kawazoe, M. Yasukawa, H. Hyodo, M. Kurita, H. Yanagi, and H. Hosono, *Nature* **389**, 939 (1997)

[192] K. Ueda, T. Hase, H. Yanagi, H. Kwazoe, H. Hosono, H. Ohta, H. Orita, H. Hirano, *J. Appl. Phys.* **89**, 1790 (2001)

[193] B. Yang, Y. He, A. Polity, and B. K. Meyer, *MRS proceedings (Symposium F-Thin film compound semiconductor photovoltaics)* **865**, F14.7 (2005)

[194] T. Nakamura, T. Shimura, M. Itoh, and Y. Takeda, *J. Solid State Chem*. **103**, 523 (1993)

[195] M. Nakamura, Y. Krockenberger, J. Fujioka, M. Kawasaki, and Y. Tokura, *Appl.*

Phys. Lett. **106**, 072103 (2015)

[196] J. B. Goodneough, in *Prog. In Solid State Chemistry*, Vol. **5**, ed. H. Reiss (Pergamon, Oxford), p. 145 (1971)

[197] G. Koster, L. Klein, W. Siemons, G. Rijinders, J. S. Dodge, C.-B. Eom, D. H. A. Blank, and M. R. Beasley, *Review of Modern Physics* **84**, 253 (2012)

[198] O. Parkash, D. Kumar, K. K. Srivastav, and R. K. Dwivedi, *Journal of Materials Science* **36**, 5805 (2001)

[199] Y. Wang, A. Chesnaud, E. Bevillon, J. Yang, and G. Dezanneau, *International Journal of Hydrogen Energy* **36**, 7688 (2011)

[200] P. Singh, O. Parkash, and D. Kumar, *Journal of Materials Science: Materials in Electronics* **16**, 145 (2005)

[201] J. M. D. Coey and S. Sanvito, *J. Phys. D: Appl. Phys.* **37**, 988 (2004)

[202] J. M. D. Coey, M. Venkatesan, and C. B. Fitzgerald, *Nature materials* **4**, 173 (2005)

List of publications

1. Useong Kim, Chulkwon Park, Young Mo Kim, **Juyeon Shin**, and Kookrin Char, "Conducting interface states at $LaInO_3/BaSnO_3$ polar interface controlled by Fermi level", *APL Materials* **4**, 071102 (2016)

2. **Juyeon Shin**, Young Mo Kim, Youjung Kim, Chulkwon Park, and Kookrin Char, "High mobility $BaSnO_3$ films and field effect transistors on non-perovskite MgO substrate", *Appl. Phys. Lett.* **109**, 262102 (2016)

3. Young Mo Kim, Chulkwon Park, Taewoo Ha, Useong Kim, Namwook Kim, **Juyeon Shin**, Youjung Kim, Jaejun Yu, Jae Hoon Kim, and Kookrin Char, "High-k perovskite gate oxide $BaHfO_3$", *APL Materials* **5**, 016104 (2017)

4. **Juyeon Shin**, Jinyoung Lim, Taewoo Ha, Young Mo Kim, Chulkwon Park, Jaejun Yu, Jae Hoon Kim and Kookrin Char, "Bandgap and mobility of epitaxial perovskite $BaSn_{1-x}Hf_xO_3$ thin films", in preparation.

5. **Juyeon Shin**, Young Mo Kim, Chulkwon Park, and Kookrin Char, "Modulation doping in $LaInO_3/BaSnO_3$ polar interface", in preparation.

List of presentations

1. **Juyeon Shin**, Useong Kim, Chulkwon Park, Young Mo Kim, Taewoo Ha, Jae Hoon Kim, and Kookrin Char, "Bandgap tuning of $(Ba_{1-x}La_x)(Sn_{1-y}Hf_y)O_3$ thin films", Workshop on Oxide Electronics 22, Paris, France, October 2015. (Poster)

2. **Juyeon Shin**, Chulkwon Park, Young Mo Kim, Youjung Kim, and Kookrin Char, "Effect of the undoped $BaSnO_3$ space layer on the high mobility $LaInO_3/Ba_{1-x}La_xSnO_3$ polar interface", American Physical society Meeting, Baltimore, Maryland, March 2016. (Oral)

3. **Juyeon Shin**, Chulkwon Park, Young Mo Kim, and Kookrin Char, "High mobility $LaInO_3/BaSnO_3/Ba_{1-x}La_xSnO_3$ polar interface", Workshop on Oxide Electronics 23, Nanjing, China, October 2016. (Oral)

4. **Juyeon Shin**, Young Mo Kim, Chulkwon Park and Kookrin Char, "Enhanced mobility at the modulated polar interface: $LaInO_3/BaSnO_3/Ba_{1-x}La_xSnO_3$, Materials Research Society Meeting, Boston, Massachusetts, November 2017. (Oral)

국문 초록

넓은 밴드갭 반도체는 고온에서 동작하고 높은 전력을 이용하는 전자 분야 응용면에서 잠재력이 풍부하기 때문에 많은 관심이 주목되고 있다. 예를 들어 SiC와 GaN 같은 전형적인 넓은 밴드갭 반도체 가운데, 페로브스카이트계 산화물인 $BaSnO_3$는 지금까지 주로 투명전도체와 투명반도체로서 디스플레이 분야의 응용을 위한 연구가 진행되어 왔었다. 디스플레이 분야에서 보통의 능동소자는, 보통 사람의 시각 인지 속도가 디지털 처리 속도보다 느리기 때문에, 전기 수송 특성중의 하나인 이동도가 투과성 보다 덜 중요하다. 하지만, $BaSnO_3$는 넓은 밴드갭 반도체 가운데 축퇴된 도핑 영역에서 가장 높은 이동도 값을 가지고 있다. 따라서 이러한 $BaSnO_3$의 높은 이동도 값이 소자로 만들었을 때 더 향상된다면, 투명 전자제품 뿐만 아니라, 고온, 고주파수 영역의 응용으로도 확대될 수 있다.

$BaSnO_3$ 기반 전자 분야의 또 다른 강점은 강한 분극현상, 강유전성, 강자성 등의 물리적 성질을 가지는 다른 페로브스카이트계 산화물과 전체적으로 에피택시얼 헤테로 구조로 만들 수 있다는 점이다. 이러한 점은 비휘발성 스위칭 메모리와 스핀트로닉스로의 응용을 가능하게 하고, 전기 전자 분야에서 정보 전달의 양과 질을 높이는데 기여할 수 있다.

이 학위 논문은 총 3가지의 관점에서 $BaSnO_3$의 이동도 향상에 관한 연구에 초점을 두고 있다. 즉, MgO 기판 위에서의 뛰어난 전기적 수송 특성, 모듈레이션 도핑 가능성을 염두에 둔 Hf 도핑에 의한 밴드갭 공학, 그리고 모듈레이션 도핑된 polar interface ($LaInO_3/BaSnO_3/La-doped\ BaSnO_3$ 구조). 모든 에피택시얼 필름은 펄스 레이저 증착 방법에 의해 만들어졌다. 그리고 결정성은 X-ray 회절 분석 방법에 의해 단상 성장

과 잘 배열된 방향성을 확인하였다. 또한 투과전자분광학에 의해 불일치 전위와 관통 전위 같은 미세 구조를 확인하였다. 필름의 전하 수송 특성, 예를 들어, 비저항, 이동도, 캐리어 밀도는 Van der Pauw 방법에 의해 측정하였다. 모든 소자들은 금속-절연체-반도체 구조를 가지고 있는 세 개의 터미널을 갖는 전계 효과 트랜지스터 구조로 만들어졌다.

$BaSnO_3$의 연구가 $SrTiO_3$, $SmScO_3$, $PrScO_3$, $LaAlO_3$, 그리고 $BaSnO_3$ 같은 페로브스카이트계 산화물 기판 위에서만 이루어졌기에 작은 사이즈, 작은 밴드갭, 산소 불안정성 같은 기판 문제를 내포하고 있었다. 만약 $BaSnO_3$ 필름이 비페로브스카이트인 MgO 기판 위에서 전하 수송 특성이 좋다면, 웨이퍼 스케일로 공정이 가능하고 기판의 산소 안정성도 좋을 것이다. 따라서 이러한 연구는 상업적으로의 $BaSnO_3$ 전자분야의 응용을 앞당길 것이다. 비페로브스카트 기판임에도 불구하고, 실험 결과 La 도핑된 $BaSnO_3$ 필름의 최고 이동도 값은 97.2 cm^2/Vs 이고 이는 $BaSnO_3$ 단결정 기판 위에서 길렀을 때의 값과 비슷하다. 그리고 전계 효과 트랜지스터의 경우 La 도핑된 $BaSnO_3$ 채널의 이동도는 43.9 cm^2/Vs, 켜졌을 때와 꺼졌을 때 전류 비율이 $3x10^7$로 측정되었고 이 값들은 $SrTiO_3$ 기판 위에서 기른 소자 특성 값보다 살짝 좋은 편이다.

$BaSnO_3$ 채널을 기초로 하는 소자의 이동도 값을 높이는 또 다른 방법은 GaAs 시스템처럼 모듈레이션 도핑을 이용하는 것이다. 현재까지는 $BaSnO_3$의 전계 효과에 의한 캐리어 조정이 금속-절연체-반도체 구조로만 이루어졌었다. 따라서 의도적인 La 도핑 또는 비의도적인 산소 공핍 같은 전자 캐리어의 소스 요소들이 소자의 특성을 떨어지게 할 수 있다. 하지만, 도핑된 더 넓은 밴드갭 물질을 사용하여 헤테로 구조를 만들면, 이온화된 불순물과의 산란을 줄임으로서 채널의 이동도를 높일 가능성이 있다. 이러한 $BaSnO_3$ 기반의 모듈레이션 도핑을 시도하기 위해, 이제 밴드갭 공학이 필요한 시점이다. 따라서, $BaSnO_3$의 Sn 자리에 Hf 대

체에 대해 연구하였고, 이는 밴드구조와 결정구조, 밴드갭을 상당히 변화시키는 결과를 가져왔다. 또한 $BaSn_{1-x}Hf_xO_3$에 La을 도핑하는 것에 관해 연구하였고, 결과적으로 이는 $BaSnO_3/BaSn_{1-x}Hf_xO_3$ 구조에서 모듈레이션 도핑 가능성을 시사해 주었다.

마지막으로, polar interface에서 $BaSnO_3$의 이동도 향상을 연구하였다. 반도체 소자에서 가장 최적의 조건은 켜졌을 때 작은 저항을 가지고 스위칭 할 수 있는 특성이다. 높은 전류, 높은 면 캐리어 밀도, 높은 이동도를 다루기 위해서 전계로 유도된 모여있는 구조가 필요하다. Polarization 도핑은 높은 밀도로 모바일 캐리어를 축적시킬 수 있는 방편이며, 이는 기존의 고체 상태의 유전체로서는 불가능했다. 최근에, $LaInO_3$/La-doped $BaSnO_3$구조에서 $10^{13}\,cm^{-2}$의 캐리어 밀도를 갖는 전도성 interface가 보고되었다. 만약 이 polar interface에서 $BaSnO_3$ 채널의 이동도가 향상된다면 $BaSnO_3$ 기반의 2DEG 과학은 더 힘있어 질 것이다. 높은 캐리어 밀도를 얻기 위해 $BaSnO_3$ 채널 쪽에 La을 약간 도핑해야 하기 때문에, 모듈레이션 도핑 기술을 더 작은 밴드갭인 $BaSnO_3$에 적용하였다. 즉, 도핑 안된 $BaSnO_3$ 스페이서 층을 $LaInO_3$와 La-doped $BaSnO_3$ 사이에 증착하였다. 이 모듈레이션 도핑된 polar interface의 향상된 이동도는 $LaInO_3/BaSnO_3$ polar interface를 고 이동도와 고 전력 전기전자 분야 응용으로 더욱 진보시킬 것이다.

Keywords: 고 이동도, $BaSnO_3$, 페로브스카이트계 산화물, 펄스레이저 증착, 넓은 밴드갭 반도체, 모듈레이션 도핑, polar interface, 밴드갭 공학

Student number: 2012-20367